Thesis for the Degree of Doctor of Philosophy

On the robust stability analysis of VSC-HVDC systems

Yujiao Song

Group of Automatic Control
Department of Signals and Systems
Chalmers University of Technology
Göteborg, Sweden 2016

On the robust stability analysis of VSC-HVDC systems
YUJIAO SONG
ISBN 978-91-7597-511-5

Doktorsavhandlingar vid Chalmers tekniska högskola
Ny serie nr 4192
ISSN 0346-718X

Group of Automatic Control
Department of Signals and Systems
CHALMERS UNIVERSITY OF TECHNOLOGY
SE–412 96 Göteborg
Sweden

Telephone: +46 (0)31 – 772 1000

Email: yujiao@chalmers.se

Typeset by the author using LaTeX.

Chalmers Reproservice
Göteborg, Sweden 2016

to my parents

Abstract

This thesis focuses on small signal stability analysis of VSC-HVDC systems, emphasizing the system stability robustness with regard to the connected AC-grid and the distributed parameter DC-grid model respectively. In addition, for strong AC-grid connected systems, analytical eigenvalue expressions are provided to investigate the impact of physical or control parameters on the system stability for both two-terminal and multi-terminal VSC-HVDC systems.

The VSC-HVDC system with a distributed parameter DC-cable model can be described by two cascaded blocks. The first block is a transfer function that will be different, due to which input and output variables that are considered. The second block is a feedback loop, where the forward path is a rational function and the return path is a dissipative infinite dimensional function, that remains the same in all cases. The stability is then analyzed using the Nyquist criterion in a straight forward manner. Examples with different operating points P_{20} and different SCRs of the connected AC-grids have been studied, showing that the VSC-HVDC system with a single Π-section cable model is sufficient to evaluate system stability, independently of the DC-cable length and impedance density.

Based on the mixed small gain and passivity theorem, this thesis provides a theoretical method to evaluate a sufficient stability condition for a two terminal VSC-HVDC system with respect to the connected AC-grid. The result is that, for the frequency band where the converter admittance matrix is not passive, the negative closed loop system is stable if the loop gain is strictly less than one. On the basis of such a theorem, the sufficient stability conditions are provided, showing that at the DC-voltage controlled converter side, the system robustness can be increased by designing $i^{ref} = P^{ref}/E_0$ instead of $i^{ref} = P^{ref}/E$. In addition, the active power controlled converter can be designed to have passive converter admittance for all frequencies and thus the system is stable under all kinds of AC-grid.

Keywords: VSC-HVDC system, distributed parameter cable model, AC-grid interaction, Nyquist stability analysis, small gain theorem, passivity theorem, symbolic eigenvalue expressions.

Acknowledgments

I would like to take this opportunity to thank Prof. Claes Breitholtz and the financial support provided by the Chalmers Energy Initiative for giving me the opportunity to join the Automatic Control group as a PhD candidate. I have been very happy studying and working here.

My deepest gratitude goes to my examiner and supervisor Professor Claes Breitholtz who worked with me closely during my PhD studies. I remembered that I was excited to receive the invitation letter from him about this PhD project as a second year master student. It was a really smooth experience to get the position and become a PhD student after my master. I'm very grateful to be his last PhD student, which provides the enormous time he spend and effort he made to teach me how to give presentations, to write papers, and to do research.

I would also like to thank my co-supervisor Professor Lina Bertling-Tjernberg, now at KTH, and the reference group members she invited at Chalmers. Abdel-Aty Edris as an international co-advisor from Quanta Technology, USA, is appreciated for his support and discussion of my research work. I have been very fortunate to have the chance to collaborate with the researchers at Electric power Department, particularly Professor Massimo Bongiorno and Georgios Stamatiou. I thank all of them for the fruitful collaboration and stimulating discussions.

Working at the division of Automatic control, Automation and Mechatronics has been an exciting experience. I would like to thank all colleagues for making this such a nice environment to work in. I would also like to thank my friend Yinan Yu for providing me various kinds of help and I will always remember the time we spent together.

Finally, I want to thank my parents. Thank you for the constant support, consideration, patience and endless love.

Yujiao Song
Göteborg, December 2016

List of publications

This thesis is based on the following appended papers:

Paper 1

Y. Song and C. Breitholtz, “Nyquist stability analysis of a VSC-HVDC system using a distributed parameter DC-cable model”, *19th IFAC World Congress*, August 2014, Cape Town, South Africa.

Paper 2

Y. Song and C. Breitholtz, “Nyquist stability analysis of an AC-grid connected VSC-HVDC system using a distributed parameter DC-cable model”, *IEEE Trans. on Power Delivery*, vol. 31, no. 2, pp. 898 - 907, April 2016.

Paper 3

Y. Song and C. Breitholtz, “On passivity based measures of robustness for a VSC-HVDC system connected to weak AC-grids”, to be submitted for possible journal publication, 2016.

Paper 4

Y. Song, C. Breitholtz, G. Stamatiou, and M. Bongiorno, “Analytical investigation of poorly damped conditions in VSC-HVDC systems”, accepted for presentation at *the 55th IEEE Conference on Decision and Control*, Las Vegas, USA, Dec, 2016.

Other publications

In addition to the appended papers, the following paper by the thesis author is related to the topic of the thesis:

Y. Song, C. Breitholtz, "VSC-HVDC system robust stability analysis based on a modified mixed small gain and passivity theorem", *submitted for 20th IFAC World Congress*, July 2017, Toulouse, France.

List of Abbreviations

abc-frame	Three phase reference frame
AC	Alternating current
DC	Direct current
dq-frame	Direct-Quadrature reference frame
HVDC	High voltage direct current
LCC	Line commuted converter
LPF	Low pass filter
LTI	Linear time invariant
MIMO	Multi-input Multi-output
MTDC	Multi-terminal high voltage direct current
PCC	Point of common coupling
PI-controller	Proportional Integral controller
PLL	Phase locked loop
p.u.	Per unit
PWM	Pulse width modulation
RHP	Right half plane
SCR	Short circuit ratio
TF	Transfer function
VSC	Voltage source converter
VSC-HVDC	Voltage source converter based high voltage direct current transmission

List of Symbols

VSC-HVDC system electrical variables

x_d	d-axis value of the variable x in the dq-frame
x_q	q-axis value of the variable x in the dq-frame
v_s	The AC source voltage in the dq-frame
E	PCC voltage in the dq-frame
E^{abc}	PCC voltage in the abc-frame
E_c	Converter measured PCC voltage in the dq-frame
E_s	PCC voltage in the $\alpha\beta$-frame
v_c^{abc}	Converter voltage in the abc-frame
v_c	The converter voltage in the dq-frame
i	Converter input current in the dq-frame
i^{abc}	Converter input current in the abc-frame
i_c	Converter measured input current in the dq-frame
L	Series inductance of the VSC phase reactor
R	Series resistance of the VSC phase reactor
$Z_g,\ Z_i$	Series AC-grid impedance matrix in the dq-frame, $i = 1, 2$
L_g	Series AC-grid inductance
R_g	Series AC-grid resistance
C	DC-side shunt capacitor
τ_s	DC-shunt capacitor charging time constant
f_0	Fundamental AC-grid frequency
ω_0	Fundamental AC-grid angular velocity $\omega_0 = 2\pi f_0$
P	Active power absorbed by the VSC from the AC-grid
Q	Reactive power absorbed by the VSC from the AC-grid
P_{load}	Active power absorbed from the VSC to the DC-grid
i_{dc}	Direct current flow into the DC-grid
v_{dc}	Direct voltage of the VSC's DC shunt capacitor
r_c	Resistance density of the DC-cable
l_c	Inductance density of the DC-cable
c_c	Capacitance density of the DC-cable
g_c	Conductance density of the DC-cable

d	Length of the DC-cable
L_{dc}	Equivalent inductance of the single Π-section DC-cable model
R_{dc}	Equivalent resistance of the single Π-section DC-cable model
C_{dc}	Equivalent capacitance of the single Π-section DC-cable model at each terminal
C_{tot}	Total shunt capacitor of the converter, i.e. $C_{tot} = C + C_{dc}$

Controller related variables

p	The differential operator with respect to time
x^{ref}	Reference signals of variable x
x_0	Steady state value of variable x
Δx	Small variation of variable x
x_i	Variable x at the i-th VSC side, where $i = 1, 2$
$\tilde{x}$	Laplace transform of the time domain variable x
x^*	Complex conjugate value of x
f_{sw}	Switching frequency of the PWM
T_{sw}	Time delay due to the switching action of the PWM
k_p	Proportional gain of the inner current PI-controller
k_i	Integral gain of the inner current PI-controller
α_c	Bandwidth of the inner current control loop
k_{pd}	Proportional gain of the DC-voltage PI-controller
k_{id}	Integral gain of the DC-voltage PI-controller
α_d	Bandwidth of the DC-voltage control loop
α_f	Bandwidth of the LPF of the measured PCC voltge E_c
α_{df}	Bandwidth of the LPF of the DC load power P_{load}
$\hat{C}$	Approximate shunt capacitor at the DC-side of VSC
ζ	Damping ratio of the DC-voltage control loop
ω_{nd}	Natural frequency of the DC-voltage control loop
k_{pp}	Proportional gain of the active power PI-controller
k_{ip}	Integral gain of the active power PI-controller
α_p	Bandwidth of the active power control loop
k_{pa}	Proportional gain of $K_{ad}(s)$
θ	AC-grid phase angle estimated by the PLL
$k_{p,pll}$	Proportional gain of the PLL PI-controller
$k_{i,pll}$	Integral gain of the PLL PI-controller
α_{pll}	Bandwidth of the PLL

Transfer functions

s	Laplace operator

$g_c(s)$	Inner current loop TF from Δi^{ref} to Δi_c
$y_i(s)$	Inner current loop TF from ΔE_c^{ref} to Δi_c
$F_v(s)$	LPF of the PCC voltage
$F_d(s)$	PI-controller of the DC-voltage
$F_f(s)$	LPF of the feed forward DC load power
$K_{ad}(s)$	$q - axis$ outer controller for d-axis PCC voltage regulation
$K_{aq}(s)$	$q - axis$ outer controller for q-axis PCC voltage regulation
$F_{pll}(s)$	PI-controller at the PLL
$G_{pll}(s)$	TF from $\text{Im}\{\Delta E\}$ to $\Delta\theta$ at PLL
$\gamma(s)$	Characteristic wave complex damping factor of the DC-cable
$Y_0(s)$	Characteristic wave admittance of the DC-cable
$h_i(s)$	TF of the distributed parameter DC-cable model, $i = 1, 2$
$h_{\pi i}(s)$	Corresponding TF of the single Π-section DC-cable model, where, $i = 1, 2$
$g_0(s)$	Forward block TF of the VSC-HVDC system block diagram
$g_1(s)$	Forward TF of the feedback loop of the block diagram
$g_{ij}(s)$	TF from the i-th input to the j-th output of the VSC-HVDC system under weak AC-grid
$\hat{g}_{ij}(s)$	TF from the i-th input to the j-th output of the VSC-HVDC system under strong AC-grid
$Y(s)$	DC-voltage controlled converter admittance matrix
$Y_p(s)$	Active power controlled converter admittance matrix

Contents

I Introductory chapters

II Included papers

Part I

Introductory chapters

Chapter 1

Overview

1.1 Background and motivation

Voltage source converter based high voltage direct current (VSC-HVDC) transmission systems have now been in operation since 1997 as it is a reliable and flexible method of power transmission [1]. In principle, the operation of VSCs does not rely on the strength of the connected AC systems compared with the thyristor-based line commuted converter (LCC-HVDC) transmission technology. Furthermore, it provides independent control of the reactive power at the two ends and independently of the active power transfer over the DC transmission [2]. A typical application of a VSC-HVDC system would be the integration of renewable energy resources over large geographical areas, due to the benefits of high transmission power capacity and low losses [3].

Stability analysis of a VSC-HVDC system is typically achieved by calculating the values of system poles, where the DC-grid is modeled by a single Π-section no matter the transmission distance [4,5]. It is often sufficient, at least when considering dynamics of short cables and low frequencies. However, if more general results are required, for example in submarine (due to increased impedance density) or long distance cables, it would be more appropriate to use a distributed parameter cable model together with transfer functions (or finite order state-space) in the linearized VSC-models.

Aside from performing as a reliable and controllable power transmission between networks, in turn, the VSC-HVDC system also brings interaction between the system components such as the converter and the AC-grid. Current existing methods to analyze the stability of grid connected converters are impedance based analysis, where the system is characterized as a negative feedback system of grid impedance and converter admittance [6–8]. On the contrary to the root locus and characteristic equation based stability analysis, the impedance based stability analysis requires less detailed information of both converter controller and grid impedance. In addition, it provides a general stability condition based on the Nyquist criterion. However, in [6], only the passivity theorem is applied to analyze system stability which is hard to achieve in the lower frequency band, especially for the converter with positive input power.

The passivity theorem guarantees stability of a feedback interconnection of two linear time invariant (LTI) input to output stable subsystems if, for instance, both of the subsystems are passive, and one of them is strictly passive [9]. Another important result in stability assessment is the small gain theorem, where the feedback interconnection of two stable subsystems is stable when the product of the gains of those two stable subsystems is strictly less than one. Since there exist many situations where both the passivity and the small gain theorems are not compatible respectively, the idea of merging those two theorems would be potentially extremely useful.

The “mixed” small gain and passivity theorem is proposed in [10, 11]. However, the subsystems are required to be causal, input and output strictly passive over the frequency band that the small gain theorem does not hold. The requirement of a system to be input and output strictly passive, especially in the high frequency band, is severe and no strictly proper system satisfies this demand for all frequencies [12]. Therefore, it is important to give a less conservative condition regarding the passivity and thus further suited to analyze the stability of a two-terminal VSC-HVDC system embedded in weak AC-grids.

Poorly-damped resonances between converter stations and DC-cables can as well appear both in two-terminal and multi-terminal VSC-HVDC systems [13,14]. Such problems are typically approached by using numerical analysis to determine the actual values of the system’s poles [15]. However, acquiring analytical expressions for these poles has the benefit of better understanding which selected parameters of the system can affect the frequency and damping characteristics of its eigenvalues. Hence, it is valuable if such symbolic descriptions can be obtained for a poorly-damped VSC-HVDC link, highlighting the relationship between the system parameters and its poorly-damped poles.

1.2 Main contribution of the thesis

The purpose of this thesis is to study the robust stability of VSC-HVDC system with respect to different DC-cable models and the connected AC-grid dynamics. In addition, the poorly-damped conditions caused by the interaction of converter and DC-grid is studied by the approximated symbolic eigenvalues. To the best of the author’s knowledge, the main contributions of this thesis are the following:

1. A mathematical model for small-signal stability analysis of a two terminal VSC-HVDC system with a distributed parameter DC-cable model has been presented. Due to the symmetric properties of the cable model, the block diagram of each input output combination could be described by a transfer function $g_0(s)$ cascaded with a feedback loop $g_1(s)/(1+g_1(s)h_1(s))$, where $g_0(s)$ is stable with reasonable design of the DC voltage PI-controller and the forward path of the feedback loop, $g_1(s)$, is a rational function of 's' and the return path $h_1(s)$ is dissipative of infinite order. Using this approach, the small-signal stability has been analyzed by use of the Nyquist criterion.

2. The stability analysis of two terminal VSC-HVDC systems embedded in weak AC-grids can be separated into two parts: the active power controlled VSC and the VSC-HVDC system while the active power controlled VSC is under steady state. On the basis of the "mixed" small gain and passivity theorem, a theoretical method to evaluate a sufficient stability condition for such two terminal VSC-HVDC systems with respect to the AC-grid weakness has been provided.

3. Symbolic approximative eigenvalue expressions have been proposed, which help to characterize poorly-damped conditions that may appear on the DC-side of a two-terminal VSC-HVDC system, while the interaction with the AC-side is neglected considering the presence of strong AC-grids. In addition, by applying a symbolic-isolation method, the order of a multi-terminal VSC-HVDC system can be reduced to an equivalent two-terminal VSC-HVDC system, which enables the proposed method to be applied.

1.3 Thesis outline

The remaining chapters of this thesis are organized as follows:

Chapter 2 describes the VSC-HVDC system topology, the controllers of VSC, the AC- as well as the DC-grid dynamics, which all in all provides a theoretical base for the VSC-HVDC system stability analysis.

Chapter 3 shows the block diagram of the constructed VSC-HVDC system dynamics, which has the form of a forward combination of transfer functions cascaded by a feedback system. Numerical analysis of VSC-HVDC systems with a distributed parameter DC-cable model embedded in both strong and weak AC-environment are studied.

Chapter 4 presents a modification of the “mixed” small gain and passivity theorem. In addition, the modified theorem is applied to evaluate a sufficient stability condition for a two terminal VSC-HVDC system with respect to the connected AC-grid weakness.

Chapter 5 provides the simplified 4th order state space model of a strong AC-grid connected two-terminal VSC-HVDC system and its symbolically approximative eigenvalues, which can directly demonstrate the impact of physical or control parameters on the system stability. Furthermore, on account of a symbolic-isolation method, the result is applied to multi-terminal VSC-HVDC systems as well.

Chapter 6 gives brief summaries of the included papers.

Chapter 2

VSC-HVDC system

The intention of this chapter is to provide the reader with a VSC-HVDC transmission scheme and the main control technologies applied to the VSC. Following to that, the most important elements of a VSC is presented. Then, the principles of the inner current control loop, the active power and DC voltage control loops, the reactive power and AC-voltage control loops, and the phase locked loop (PLL) are described in some detail. Finally, the DC-cable model and the AC-grid dynamics are presented.

2.1 Introduction

The system under study is depicted in Fig. 1. The source voltage, the point of common coupling (PCC) voltage, the converter voltage and the converter input current are denoted by v_s, E, v_c and i respectively. Weak AC-grids are modeled by the impedance matrices $Z_1(s)$ and $Z_2(s)$ at the synchronous frame respectively. The so-called synchronous frame is oriented to be in alignment with the voltage direction, due to the PLL [16]. The PLL dynamics will be considered to build converter grid interconnection.

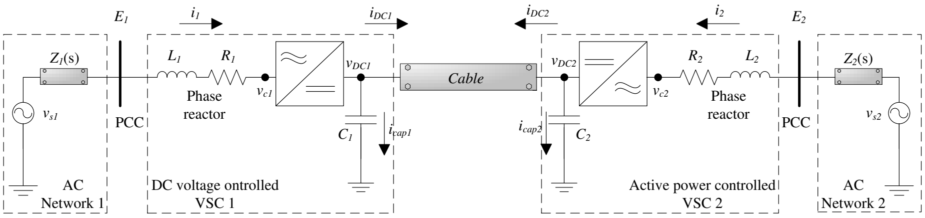

Figure 2.1: Standard HVDC-VSC system embedded in a weak AC-environment.

At the AC-side of the VSCs, the series inductances ($L_1,\ L_2$) and resistances ($R_1,\ R_2$) represent the AC phase reactors and (indirectly) the power losses in the converters as well. The phase reactors serve the function both of stabilizing the AC current and to enable the control of active and reactive output power from the VSC separately. The DC shunt capacitors at the terminals are denoted by C_1, C_2 respectively, which serve the purpose of stabilizing the DC voltage and to reduce the ripple introduced by the harmonics injected by the VSC [2].

In standard VSC-HVDC systems, one converter station (VSC1) is assigned the duty as the DC voltage controller to secure the stability of the DC-Bus voltage; the other station (VSC2) operates as the active power controller to guarantee and balance the power exchanges [17]. Moreover, in each VSC, it is possible to control the grid voltage at the AC-side, which in this thesis is further discussed.

If the DC-cable is modeled by a single Π-section, the stability of the system can be investigated by an eigenvalue calculation. However, the high frequency information is not necessarily well interpreted by the single Π-section cable model and thus potentially inconvenient to analyze the real dynamic influence of the DC-cable. Consequently, the VSC-HVDC system using a distributed parameter cable model is formulated as well.

The strength of the connected AC-grid relative to the power rating of the HVDC link is described by the value of short circuit ratio (SCR). SCR is calculated as the value of AC-grid admittance at fundamental frequency [18]. In this thesis, the connected AC-grid will be modeled as series R_gL_g-circuits.

2.2 VSC control system

In this subsection, the VSC model is derived in the so-called power invariant dq reference frame [19], where the frame is chosen to be in align with the PCC voltage direction and thus the steady state of the q-axis converter measured PCC voltage is zero i.e. $E_{cq10} = E_{cq20} = 0$. The two VSCs are assumed to be ideal and symmetrical, having a switching frequency around 1 [kHz]. In the following, the units for voltage, current and active power are [kV], [kA] and [MW] respectively and all reference signals x are expressed as x^{ref}, the differential operator with respect to time is denoted 'p' and the Laplace transform of a time domain variable $x(t)$ is denoted $\tilde{x}(s)$.

The AC-grid frequency is assumed to be constant i.e. $\omega_0 = 2\pi f_0$ and $f_0 = 50$ [Hz]. Since the VSCs are assumed symmetric, the variables and parameters in this subsection are not subscribed by the numbers 1 and 2, used to denote the different VSCs.

The local controller of the VSC is separated into two cascaded parts: inner current controller and outer controller. The inner current controller is to speed up the current dynamics and provides the voltage reference (v_{cd}^{ref} and v_{cq}^{ref}) to the pulse width modulator (PWM). The d-axis outer controller is used to track the reference of either the DC voltage or the active power and generates the d-axis current reference (i_d^{ref}) to the inner current loop; The q-axis outer controller is used to decrease the voltage drop of the PCC voltage [20] and it therefore generates a reference for the q-axis current (i_q^{ref}).

2.2.1 Vector current control method

The principle of the VSC controller is to control the magnitude and phase of the fundamental frequency component of the AC voltage at the valve side of the series inductive interface (v_c), in such a way that the converter input current (i) through the phase reactor has the desired phase and magnitude as well. With the vector control method, three phase currents are transformed to d- and q-axis quantities based on the Park transformation [19]. Similarly, the desired current d- and q-quantities can be calculated by the desired current magnitude and phase in the three phase system. Since the dq-frame is chosen to be in align with the PCC voltage, the active power P^{ref} and the reactive power Q^{ref} are thus determined by i_{cd} and i_{cq} separately [2].

Applying the voltage Kirchhoff law to the phase reactor at the AC-side of the VSC:

$$L \cdot \frac{\mathrm{d}i^{abc}}{\mathrm{d}t} = -R \cdot i^{abc} + E^{abc} - v_c^{abc} \tag{2.1}$$

where the relation between the abc (three phase) and dq reference frames is given by Park's transformation:

$$x^{abc} = P^{-1} x_{dq0} \tag{2.2}$$

$$P = \frac{2}{3} \begin{bmatrix} \cos(\omega t) & \cos(\omega t - \frac{2\pi}{3}) & \cos(\omega t + \frac{2\pi}{3}) \\ -\sin(\omega t) & -\sin(\omega t - \frac{2\pi}{3}) & -\sin(\omega t + \frac{2\pi}{3}) \\ \frac{1}{2} & \frac{1}{2} & \frac{1}{2} \end{bmatrix}$$

Applying the Park transformation to eq.(2.1), the dq-frame model of current dynamics is obtained:

$$L \cdot \frac{\mathrm{d}i_{cd}}{\mathrm{d}t} = -R \cdot i_{cd} + \omega_0 L \cdot i_{cq} + E_{cd} - v_{cd} \tag{2.3}$$

$$L \cdot \frac{\mathrm{d}i_{cq}}{\mathrm{d}t} = -R \cdot i_{cq} - \omega_0 L \cdot i_{cd} + E_{cq} - v_{cq} \tag{2.4}$$

The current control signal consists of a feedback signal from a PI-controller and two feed-forward signals, i.e. the filtered PCC voltage and the cross coupling current [21]. The reference voltages (v_{cd}^{ref}, v_{cq}^{ref}) are given by:

$$\tilde{v}_{cd}^{ref} = -(k_p + \frac{k_i}{s})(\tilde{i}_d^{ref} - \tilde{i}_{cd}) + \frac{a_f}{s + a_f}\tilde{E}_{cd} + \omega_0 L \cdot \tilde{i}_{cq} \tag{2.5}$$

$$\tilde{v}_{cq}^{ref} = -(k_p + \frac{k_i}{s})(\tilde{i}_q^{ref} - \tilde{i}_{cq}) + \frac{a_f}{s + a_f}\tilde{E}_{cq} - \omega_0 L \cdot \tilde{i}_{cd} \tag{2.6}$$

Due to the switching action of PWM inside the converter, a delay of half a switching period appears, where $T_{sw} = 1/(2f_{sw}) = 0.5$ [ms]. After having designed the inner current loop relatively slow, the delay is reasonable to ignore in the analysis of system dynamics i.e. $v_{cd}^{ref} \approx v_{cd}$ and $v_{cq}^{ref} \approx v_{cq}$ [6]. Consequently, the dynamics between the d- and q-axis is decoupled at the inner current loop.

The PI-parameters are designed as $k_p = a_c L$ and $k_i = a_c R$, where a_c is the design bandwidth of the inner current loop. Hence the phase reactor pole of $-R/L$ is thus canceled by the inner current PI-controller. Note that the unavoidable uncertainties, ΔL and ΔR in the AC-side model parameters, L and R, are assumed to be quite small ($|\Delta L|/L \ll 1$, etc). Hence, these uncertainties will have only a minor impact on the inner current loop performance. In addition, since the outer loop design bandwidth is usually designed to be at least ten times smaller than a_c, the effect caused by the inner loop parameter uncertainty does not influence the entire system dynamics significantly. Therefore, the design of the inner current loop PI-controller based on model parameters is well justified.

Consequently, the linearized inner current closed loop in the Laplace domain is given by:

$$\begin{aligned}
\Delta\tilde{i}_{cd}(s) &= \frac{a_c}{s + a_c}\Delta\tilde{i}_d^{ref}(s) + \frac{s^2}{(Ls + R)(s + a_c)(s + a_f)}\Delta\tilde{E}_{cd} \\
&= g_c(s)\Delta\tilde{i}_d^{ref}(s) + y_i(s)\Delta\tilde{E}_{cd} \qquad (2.7) \\
\Delta\tilde{i}_{cq}(s) &= g_c(s)\Delta\tilde{i}_q^{ref}(s) + y_i(s)\Delta\tilde{E}_{cq} \qquad (2.8)
\end{aligned}$$

Note that the low pass filter (LPF) of the feed-forward PCC voltage is used to filter out the high frequency resonance at the AC-side. Therefore, when strong AC-grid is considered, the bandwidth a_f can be designed to be large and thus $y_i(s) \approx 0$.

2.2.2 Direct voltage controller

The DC voltage is determined by the capacitor charging power that is the difference between the input active power to the VSC (assuming that the

VSC in itself is power lossless) and the DC load power:

$$\frac{\mathrm{d}}{\mathrm{d}t}(\frac{1}{2}C \cdot v_{dc}^2) = P - P_{load} \tag{2.9}$$

The corresponding linearized power balance close to the operating point is:

$$\Rightarrow \quad C \cdot v_{dc0} \cdot \frac{\mathrm{d}\Delta v_{dc}}{\mathrm{d}t} = \Delta P - \Delta P_{load} \tag{2.10}$$

Therefore, the linearized expression of the input active power and the DC load power are required, where the complex conjugate value of x is denoted by x^*:

$$\begin{aligned} P &= Re\{(E_0 + \Delta E_{cd} + j\Delta E_{cq})(i_{d0} + \Delta i_{cd} + j(i_{q0} + \Delta i_{cq}))^*\} \\ &\approx \underbrace{E_0 i_{d0}}_{P_0} + \underbrace{E_0 \Delta i_{cd} + i_{d0}\Delta E_{cd} + i_{q0}\Delta E_{cq}}_{\Delta P} \end{aligned} \tag{2.11}$$

$$\begin{aligned} P_{load} &= (v_{dc0} + \Delta v_{dc})(i_{dc0} + \Delta i_{dc}) \\ &\approx \underbrace{v_{dc0} i_{dc0}}_{P_{load0}} + \underbrace{v_{dc0}\Delta i_{dc} + i_{dc0}\Delta v_{dc}}_{\Delta P_{load}} \end{aligned} \tag{2.12}$$

Equation (2.11) shows that ΔP is proportional to Δi_{cd} and independent of Δi_{cq}. Therefore, the output of the DC voltage controller i.e. the d-axis reference current, can be provided through the reference input active power. The reference input active power is the sum of the output from a PI-controller operating on the error of the DC voltage square and the filtered feed forward DC load power (with bandwidth a_{df}):

$$P^{ref} = (k_{pd} + \frac{k_{id}}{p}) \cdot \nu + \frac{a_{df}}{p + a_{df}} P_{load} \tag{2.13}$$

$$\nu = \frac{(v_{dc}^{ref})^2 - v_{dc}^2}{2} \tag{2.14}$$

$$\Delta \tilde{P}^{ref} = v_{dc0} F_d(s)(\Delta \tilde{v}_{dc}^{ref} - \Delta \tilde{v}_{dc}) + F_f(s)\Delta \tilde{P}_{load} \tag{2.15}$$

$$F_d(s) = k_{pd} + \frac{k_{id}}{s} \text{ and } F_f(s) = \frac{a_{df}}{s + a_{df}}$$

Traditionally, the reference current is designed as [3]:

$$i_d^{ref} = P^{ref}/(F_v(s) \cdot E_c) \text{ and } F_v(s) = \frac{a_f}{s + a_f} \tag{2.16}$$

$$\Delta i_d^{ref} = \frac{1}{E_0}\Delta P^{ref} - F_v(s)\frac{P_0}{E_0^2}\Delta E_{cd} \tag{2.17}$$

As seen from eq.(2.17), a negative admittance $-P_0/E_0^2$ appears for the positive input power, relating changes in the measured PCC voltage to the changes in the d-axis reference current. This may deteriorate the stability of the interconnected converter and AC-grid system. Thus, we propose that the d-axis reference current is designed as below, hence removing the negative admittance:

$$i_d^{ref} = P^{ref}/E_0 \tag{2.18}$$

$$\Delta i_d^{ref} = \Delta P^{ref}/E_0 \tag{2.19}$$

After ignoring both the LPF in eq.(2.15) and the inner current loop dynamics i.e. $\Delta i_{cd} = \Delta i_d^{ref}$, designing the PI-controller parameters as $k_{pd} = 2\hat{C}\zeta\omega_{nd}$ and $k_{id} = \hat{C}\omega_{nd}^2$, the transfer function from $\Delta\tilde{v}_{dc}^{ref}$ to $\Delta\tilde{v}_{dc}$ is:

$$\frac{\Delta\tilde{v}_{dc}}{\Delta\tilde{v}_{dc}^{ref}} \approx \frac{2\zeta\omega_{nd}\frac{\hat{C}}{C}s + \omega_{nd}^2\frac{\hat{C}}{C}}{s^2 + 2\zeta\omega_{nd}\frac{\hat{C}}{C}s + \omega_{nd}^2\frac{\hat{C}}{C}} \tag{2.20}$$

$\hat{C}$ is the estimated DC shunt capacitance and C is the actual physical shunt capacitance. The damping ratio ζ and natural frequency ω_{nd} are amplified by $\sqrt{\hat{C}/C}$ compared to the designed parameters. Since the physical shunt capacitance C contains an impact from the DC-cable distributed shunt capacitance, and is assumed to be a bit larger than $\hat{C}$; then ζ and ω_{nd} should be a bit higher than the designed value in order to compensate for the error. In this thesis, the influence of such parameter uncertainty of C is not considered. ζ and ω_{nd} are chosen to be 1 and $0.4a_d$, which guarantees that the DC voltage loop bandwidth of eq.(2.20) is a_d.

2.2.3 Active power controller

For the outer controller of transmitted active power, again a PI-controller is used. The controller parameters are designed by inner current loop pole cancelation i.e. $k_{pp} = a_p/a_c$, $k_{ip} = a_p$. The bandwidth of the outer loop is chosen as $a_p = 0.2a_d$. Therefore, the DC voltage would not display large oscillations during the variations of transmitted active power. The linearized differential equations (where $E_{c0} = E_0$) of the active power control loop are derived as follows:

$$i_d^{ref} = (k_{pp} + \frac{k_{ip}}{p})(P^{ref} - P)/E_c \tag{2.21}$$

$$\Rightarrow \Delta\tilde{i}_d^{ref} = \frac{1}{E_0}(k_{pp} + \frac{k_{ip}}{s})(\Delta\tilde{P}^{ref} - \Delta\tilde{P}) \tag{2.22}$$

2.2.4 Reactive power and AC voltage controller

The idea of the AC voltage or reactive power controller is to compensate for the AC voltage drop i.e. to increase the reactive power at PCC when the AC voltage is lower than the reference PCC voltage [20]. In this thesis, both the d- and q-axis PCC voltages are regulated by the q-axis current and Δi_q^{ref} is expressed as:

$$\begin{aligned}\Delta\tilde{i}_q^{ref} &= K_{ad}(s)\cdot(\Delta\tilde{E}^{ref} - \Delta\tilde{E}_{cd}) + K_{aq}(s)\cdot(\Delta\tilde{E}_q^{\ ref} - \Delta\tilde{E}_{cq}) \\ &= K_{ad}(s)\cdot(\Delta\tilde{E}^{ref} - \Delta\tilde{E}_{cd}) - K_{aq}(s)\cdot\Delta\tilde{E}_{cq} \qquad (2.23)\end{aligned}$$

The design of the controllers $K_{ad}(s)$ and $K_{aq}(s)$ will be further discussed in Chapter 3 and 4.

2.2.5 Phase Locked Loop

Phase locked loop is applied to track the rotating phase angle θ^{ref}, which is used for transforming the converter *dq*-frame from the stationary $\alpha\beta$-frame. At steady state, the converter *dq*-frame coincides with the grid *dq*-frame. E_s, E and E_c are the PCC voltages in the $\alpha\beta$-frame, grid *dq*-frame and converter *dq*-frame respectively. θ^{ref} and θ are the grid phase angle and converter phase angle (tracked through PLL).

At steady state, $\theta = \theta^{ref}$. The frame transformation gives: $E_s = e^{j\theta^{ref}}E$ and $E_s = e^{j\theta}E_c$. Introducing $\Delta\theta = \theta - \theta^{ref}$, obviously E_c is expressed as $E_c = e^{-j\Delta\theta}E$.

Since the phase angle and the AC frequency cannot be measured directly, the measured sinusoidal PCC voltage is used to track the phase angle together with one PI-controller ($F_{pll}(s) = k_{p,pll} + \frac{k_{i,pll}}{s}$). The block diagram of the nonlinear PLL is shown at Fig. 2.2. At steady state, $\Delta\theta = 0$ and the imaginary part (*q*-axis) of the PCC voltage in the converter *dq*-frame is zero as well, i.e. at steady state, $E_c = E_0$. The linearized equations are given as follows, where $e^{-j\Delta\theta} \approx 1 - j\cdot\Delta\theta$ if $|\Delta\theta| \leq \varepsilon$, where ε is small.

$$\begin{aligned}E_c &= E\cdot e^{-j\Delta\theta} \approx (E_0 + \Delta E)\cdot(1 - j\cdot\Delta\theta) \\ &\approx E_0 + \Delta E - jE_0\cdot\Delta\theta \qquad (2.24) \\ \Delta\omega &= \left(k_{p,pll} + \frac{k_{i,pll}}{p}\right)\cdot \mathrm{Im}\{E_c\} = F_{pll}(p)\cdot(\mathrm{Im}\{\Delta E\} - E_0\cdot\Delta\theta) \qquad (2.25) \\ \frac{\mathrm{d}\Delta\theta}{\mathrm{d}t} &= \frac{\mathrm{d}(\theta - \theta^{ref})}{\mathrm{d}t} = \omega - \omega^{ref} \\ &= \omega_0 + F_{pll}(p)\cdot(\mathrm{Im}\{\Delta E\} - E_0\cdot\Delta\theta) - \omega^{ref} \qquad (2.26)\end{aligned}$$

If $\omega^{ref} = \omega_0$, a P-controller is enough to reach zero steady state error, which implies that the integral action of the PI-controller is used to compensate for the grid frequency approximation. In this thesis, we assume that $\omega^{ref} = \omega_0$ and design $k_{i,pll} = 0$, $k_{p,pll} = a_{pll}/E_0$. The transfer function from $\mathrm{Im}\{\Delta E\}$ to $\Delta\theta$ is given as follows, where the bandwidth of the PLL,

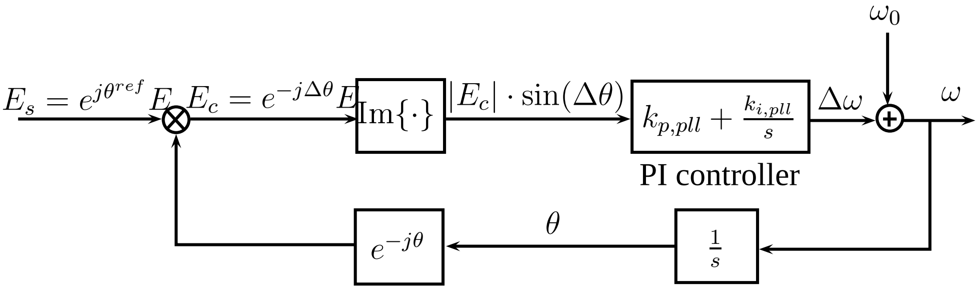

Figure 2.2: Model of Phase Locked Loop.

a_{pll}, should satisfy: $a_{pll} \leq 0.1a_c$, where a_c is the bandwidth of the inner current loop [22].

$$\frac{\Delta\tilde{\theta}}{\mathrm{Im}\{\Delta\tilde{E}\}} = G_{pll}(s) = \frac{a_{pll}/E_0}{s + a_{pll}} \tag{2.27}$$

As discussed above, at steady state, the converter dq-frame coincides with the grid dq-frame, i.e. $E_{c0} = E_0$ and $i_{c0} = i_0$. Besides, $E_c = e^{-j\Delta\theta}E$ and $i = e^{j\Delta\theta}i_c$. After considering the transfer function $G_{pll}(s)$ and the approximation $e^{-j\Delta\theta} \approx 1 - j \cdot \Delta\theta$, the linearized relations are given as follows:

$$\Delta E_c = \Delta E - jE_0 \cdot \Delta\theta = \Delta E - jE_0 \cdot G_{pll}(p) \cdot \mathrm{Im}\{\Delta E\} \tag{2.28}$$

$$\Delta i = \Delta i_c + ji_0 \cdot \Delta\theta = \Delta i_c + ji_0 \cdot G_{pll}(p) \cdot \mathrm{Im}\{\Delta E\} \tag{2.29}$$

In the Laplace form, the relations are given as follows. Note that the variable x in dq-frame is a complex number and can be expressed as $x = x_d + j \cdot x_q$, where the subscriptions d, q represent the real and imaginary part respectively:

$$\Delta\tilde{E}_{cd} = \Delta\tilde{E}_d \tag{2.30}$$

$$\Delta\tilde{E}_{cq} = (1 - E_0 G_{pll}(s)) \cdot \Delta\tilde{E}_q \tag{2.31}$$

$$\Delta\tilde{i}_d = \Delta\tilde{i}_{cd} - i_0^q G_{pll}(s) \cdot \Delta\tilde{E}_q = \Delta\tilde{i}_{cd} + \frac{Q_0}{E_0} G_{pll}(s) \cdot \Delta\tilde{E}_q \tag{2.32}$$

$$\Delta\tilde{i}_q = \Delta\tilde{i}_{cq} + i_0^d G_{pll}(s) \cdot \Delta\tilde{E}_q = \Delta\tilde{i}_{cd} + \frac{P_0}{E_0} G_{pll}(s) \cdot \Delta\tilde{E}_q \tag{2.33}$$

The equilibriums of the PLL are $\Delta\omega = 0$ and $\Delta\theta = k\pi$ (k is odd implies unstable equilibrium and k is even implies stable equilibrium), thus the initial value of $\Delta\theta$ should be bounded within $[-\pi,\ \pi]$ in order to reach equilibrium $\Delta\omega = 0$ and $\Delta\theta = 0$. For the strong AC-grid case, the PLL dynamics is ignored, which implies $G_{pll}(s) \approx 1/E_0$.

2.3 AC-grid model

The AC-grid model is not unique. In this thesis, the AC-grid is modeled by the series R_gL_g-circuit. The strength of the AC-grid is represented by the short circuit ratio (SCR), which is the ratio between short circuit power and rated power. If the base power unit is set as the rated power, SCR $= 1/Z_g$, where Z_g is the AC-grid impedance in per unit [23].

For the series connected AC-grid, since the transmission line typically has a Q-value ($\omega L_g/R_g$) that exceeds 10, the grid resistance R_g can be ignored when calculating SCR, i.e. SCR $\approx 1/(\omega L_g)$ where ωL_g is the grid reactance in per unit. For a strong grid, L_g is ignored, implying that SCR approaches infinity. The least SCR value which has been practically experienced by the end of year 2004 is 1.3 [2]. There is no particular limit on SCR, however, as the transmittable maximum active power is limited by a smaller SCR [24].

The dynamics of the series R_gL_g-circuit modeled in the synchronous dq-frame is:

$$\Delta\tilde{v}_{sd} - \Delta\tilde{E}_d = (L_g s + R_g)\Delta\tilde{i}_d - \omega_0 L_g \Delta\tilde{i}_q \tag{2.34}$$

$$\Delta\tilde{v}_{sq} - \Delta\tilde{E}_q = \omega_0 L_g \Delta\tilde{i}_d + (L_g s + R_g)\Delta\tilde{i}_q \tag{2.35}$$

2.4 DC-grid model

2.4.1 Distributed parameter DC-cable model

The conventional method of approximating a transmission line is to replace the line by cascaded lumped RLCG-sections, which is shown in Fig. 2.3. The terminal voltage and current are represented by v_{dc1}, v_{dc2}, i_{dc1} and i_{dc2}. The cable parameters are given by r_c, l_c, c_c, g_c and d, which are the cable densities of resistance, inductance, capacitance, conductance, and cable length.

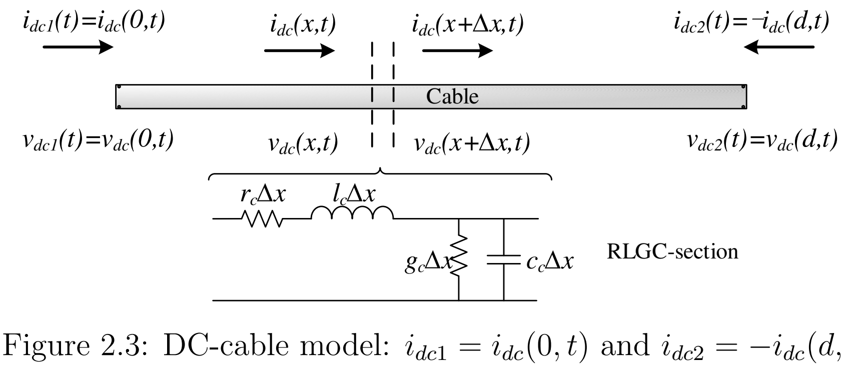

Figure 2.3: DC-cable model: $i_{dc1} = i_{dc}(0,t)$ and $i_{dc2} = -i_{dc}(d,t)$.

Define the current from the AC- to the DC-side as a positive current. At arbitrary distance 'x' from terminal 1, the voltage v_{dc} and current i_{dc} obey the following two equations:

$$v_{dc}(x+\Delta x,t) = v_{dc}(x,t) - r_c\Delta x \cdot i_{dc}(x,t) - l_c\Delta x \cdot \frac{\partial i_{dc}(x,t)}{\partial t}$$
$$i_{dc}(x+\Delta x,t) = i_{dc}(x,t) - g_c\Delta x \cdot v_{dc}(x+\Delta x,t) - c_c\Delta x \cdot \frac{\partial v_{dc}(x+\Delta x,t)}{\partial t}$$

$$\frac{v_{dc}(x+\Delta x,t) - v_{dc}(x,t)}{\Delta x} = -r_c \cdot i_{dc}(x,t) - l_c \cdot \frac{\partial i_{dc}(x,t)}{\partial t} \tag{2.36}$$
$$\frac{i_{dc}(x+\Delta x,t) - i_{dc}(x,t)}{\Delta x} = -g_c \cdot v_{dc}(x+\Delta x,t) - c_c \cdot \frac{\partial v_{dc}(x+\Delta x,t)}{\partial t} \tag{2.37}$$

As $\Delta x \to 0$, there are:

$$\lim_{\Delta x\to 0} \frac{v_{dc}(x+\Delta x,t) - v_{dc}(x,t)}{\Delta x} = \frac{\partial v_{dc}(x,t)}{\partial x} \tag{2.38}$$
$$\lim_{\Delta x\to 0} \frac{i_{dc}(x+\Delta x,t) - i_{dc}(x,t)}{\Delta x} = \frac{\partial i_{dc}(x,t)}{\partial x} \tag{2.39}$$
$$\lim_{\Delta x\to 0} \frac{\partial v_{dc}(x+\Delta x,t)}{\partial t} = \frac{\partial v_{dc}(x,t)}{\partial t} \tag{2.40}$$
$$\lim_{\Delta x\to 0} v_{dc}(x+\Delta x,t) = v_{dc}(x,t) \tag{2.41}$$

With infinitely small distance Δx, by eq.(2.38 - 2.41), eq.(2.36, 2.37) can be rewritten as follows:

$$\frac{\partial v_{dc}(x,t)}{\partial x} + r_c \cdot i_{dc}(x,t) + l_c \cdot \frac{\partial i_{dc}(x,t)}{\partial t} = 0$$
$$\frac{\partial i_{dc}(x,t)}{\partial x} + g_c \cdot v_{dc}(x,t) + c_c \cdot \frac{\partial v_{dc}(x,t)}{\partial t} = 0$$

Taking Laplace transforms of each term in the above equations, gives:

$$\frac{\mathrm{d}\tilde{v}_{dc}(x,s)}{\mathrm{d}x} + (r_c + l_c \cdot s) \cdot \tilde{i}_{dc}(x,s) = 0 \tag{2.42}$$
$$\frac{\mathrm{d}\tilde{i}_{dc}(x,s)}{\mathrm{d}x} + (g_c + c_c \cdot s) \cdot \tilde{v}_{dc}(x,s) = 0 \tag{2.43}$$

Differentiate each term in eq.(2.42) with respect to x and replace $\mathrm{d}\tilde{i}_{dc}/\mathrm{d}x$ by use of eq.(2.43). The Laplace transformed version of the damped wave equation is then obtained:

$$\frac{\mathrm{d}^2\tilde{v}_{dc}(x,s)}{\mathrm{d}x^2} - (r_c + l_c \cdot s)(g_c + c_c \cdot s) \cdot \tilde{v}_{dc}(x,s) = 0 \tag{2.44}$$

Introducing $\gamma(s)$ and $Y_0(s)$, the characteristic wave complex damping factor and the characteristic wave admittance for the transmission line, respectively. They are defined by:

$$Y_0(s) = \sqrt{\frac{c_c \cdot s + g_c}{l_c \cdot s + r_c}} \tag{2.45}$$

$$\gamma(s) = d \cdot \sqrt{(c_c \cdot s + g_c)(l_c \cdot s + r_c)} \tag{2.46}$$

Letting A(s), B(s) be constants of integration, the solutions of eq.(2.42) and eq.(2.43) are given as:

$$\tilde{v}_{dc}(x,s) = A(s)\cosh(\gamma(s) \cdot x) + B(s)\sinh(\gamma(s) \cdot x) \tag{2.47}$$

$$\begin{aligned} \tilde{i}_{dc}(x,s) &= -\frac{1}{(r_c + l_c \cdot s)} \frac{\mathrm{d}\tilde{v}_{dc}(x,s)}{\mathrm{d}x} \\ &= -\frac{1}{(r_c + l_c \cdot s)}(A(s)\gamma(s)\sinh(\gamma(s) \cdot x) + B(s)\gamma(s)\cosh(\gamma(s) \cdot x)) \end{aligned} \tag{2.48}$$

A(s) and B(s) are then determined by the boundary conditions:

$$\begin{aligned} &\tilde{v}_{dc}(0,s) = \tilde{v}_{dc1}(s) = A(s) \\ &\Rightarrow A(s) = \tilde{v}_{dc1}(s) && (2.49) \\ &\tilde{v}_{dc}(d,s) = \tilde{v}_{dc2}(s) = A(s)\cosh(\gamma(s) \cdot d) + B(s)\sinh(\gamma(s) \cdot d) \\ &\Rightarrow B(s) = -\coth(\gamma(s) \cdot d) \cdot \tilde{v}_{dc1}(s) + \frac{1}{\sinh(\gamma(s) \cdot d)}\tilde{v}_{dc2}(s) && (2.50) \end{aligned}$$

With the relations of $\tilde{i}_{dc1}(s) = \tilde{i}_{dc}(0,s)$ and $\tilde{i}_{dc2}(s) = -\tilde{i}_{dc}(d,s)$, the terminal voltage and current satisfying the following relations, where $\Gamma(s) = d \cdot \gamma(s)$:

$$\tilde{i}_{dc1}(s) = \underbrace{Y_0(s)\coth(\Gamma(s))}_{h_1(s)} \cdot \tilde{v}_{dc1}(s) - \underbrace{Y_0(s)\frac{1}{\sinh(\Gamma(s))}}_{h_2(s)} \cdot \tilde{v}_{dc2}(s) \tag{2.51}$$

$$\tilde{i}_{dc2}(s) = -Y_0(s)\frac{1}{\sinh(\Gamma(s))} \cdot \tilde{v}_{dc1}(s) + Y_0(s)\coth(\Gamma(s)) \cdot \tilde{v}_{dc2}(s) \tag{2.52}$$

Equivalently, the relation between the terminal terms can be written in the matrix form as:

$$\begin{pmatrix} \tilde{i}_{dc1}(s) \\ \tilde{i}_{dc2}(s) \end{pmatrix} = \begin{pmatrix} h_1(s) & -h_2(s) \\ -h_2(s) & h_1(s) \end{pmatrix} \cdot \begin{pmatrix} \tilde{v}_{dc1}(s) \\ \tilde{v}_{dc2}(s) \end{pmatrix} \tag{2.53}$$

It is worth to be mentioned that $h_1^2(s) - h_2^2(s) = Y_0^2(s) = \frac{c_c \cdot s + g_c}{l_c \cdot s + r_c}$, where $h_1(s)$ and $h_2(s)$ are the short cut admittances at each side.

2.4.2 Single Π-section DC-cable model

The single Π-section DC-cable model is depicted in Fig. 2.4.

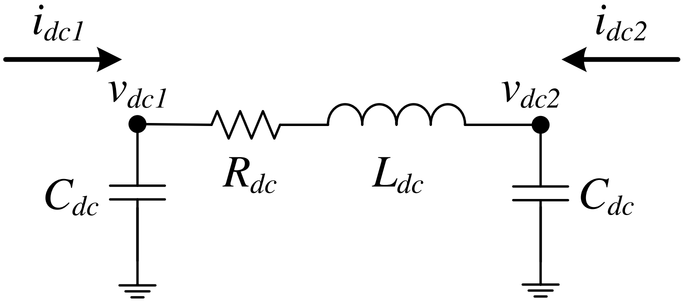

Figure 2.4: Single Π-section DC-cable model: $C_{dc} = d \cdot c_c/2$, $L_{dc} = d \cdot l_c$ and $R_{dc} = d \cdot r_c$.

Similarly, the relation between the terminal voltages and currents can be written in the matrix form as:

$$\begin{pmatrix} \tilde{i}_{dc1}(s) \\ \tilde{i}_{dc2}(s) \end{pmatrix} = \begin{pmatrix} h_{\pi1}(s) & -h_{\pi2}(s) \\ -h_{\pi2}(s) & h_{\pi1}(s) \end{pmatrix} \cdot \begin{pmatrix} \tilde{v}_{dc1}(s) \\ \tilde{v}_{dc2}(s) \end{pmatrix} \tag{2.54}$$

$$\begin{aligned} \text{where, } h_{\pi1}(s) &= c_c s \cdot d/2 + 1/(l_c s + r_c)/d \\ h_{\pi2}(s) &= 1/(l_c s + r_c)/d \end{aligned}$$

Chapter 3

Nyquist stability analysis of system with a distributed parameter DC-cable model

In this chapter, the two terminal VSC-HVDC system embedded in strong or weak AC-environments is considered and transformed into the block diagram in Fig. 3.

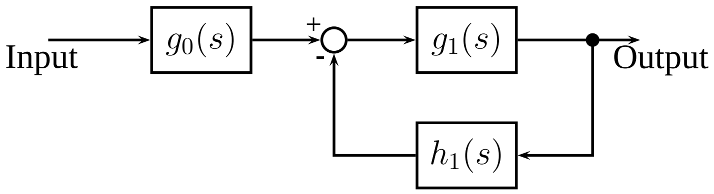

Figure 3.1: Block diagram of a VSC-HVDC system with a distributed parameter DC-cable model: g_0 is the forward transfer function, g_1h_1 is the open loop function of the feedback loop $g_1/(1+g_1h_1)$.

The first block, $g_0(s)$, is a transfer function that will differ depending on what input and output variables are considered, but which is in all realistic cases stable. The second block, $g_1(s)/(1+g_1(s)h_1(s))$, is a feedback loop where the forward path, $g_1(s)$, is a rational function and the return path, $h_1(s)$, is a dissipative infinite dimensional function, remaining the same in all cases. The stability is then analyzed, using the Nyquist criterion, in a straightforward manner. Numerical examples are as well given in this section. The physical and control parameters used for simulation are listed in Tab. 1 and Tab. 1.

Table 3.1: Bandwidth design of VSC-HVDC system

Inner current loop	a_c	4p.u.	400π [rad/s]
Active power outer loop	a_p	0.1p.u.	10π [rad/s]
DC voltage outer loop	a_d	0.4p.u.	40π [rad/s]
PLL loop	a_{pll}	0.4p.u.	40π [rad/s]
LPF of AC voltage	a_f	0.4p.u.	40π [rad/s]
LPF of DC load power	a_{df}	0.4p.u.	40π [rad/s]

Table 3.2: Parameter of VSC-HVDC system

Cable distance	d	50	km
Cable inductance density	l_c	0.189	mH/km
Cable capacitance density	c_c	0.207	μF/km
Cable resistance density	r_c	0.0376	Ω/km
Cable conductance density	g_c	0	S/km
Phase reactor inductance	L	53	mH
Phase reactor resistance	R	0.167	Ω
DC shunt capacitor ($\tau_s = 2.5$ ms)	C	33	μF
Rated AC voltage (dq-frame)	v_{sd0}	200	kV
Rated DC voltage	v_{dc0}	300	kV
Rated transmission power	P_0	600	MW
System frequency	f_0	50	Hz
Weak AC-grid inductance	L_g	53.1	mH
Weak AC-grid resistance	R_g	1.11	Ω

3.1 Block diagram

In this thesis, the converter (VSC) comprising the switching valves is surrounded by the phase reactor at the AC-side and the shunt capacitor at the DC-side. Therefore, there are five input signals at each converter for small signal stability analysis, i.e. the AC source voltage (in the *dq*-frame) Δv_{sd} and Δv_{sq}, the *d*-axis reference signal ΔP^{ref} or Δv_{dc}^{ref}, the *q*-axis reference signal ΔE^{ref} and one internal input signal Δi_{dc} (perform as a state variable for the entire VSC-HVDC system).

When the converter is embedded in strong AC-grid, it is not necessary to control the AC voltage and thus reasonable to assume that both Δv_{sq}

and ΔE^{ref} are zero. There are three input signals for each converter i.e. the d-axis AC source voltage Δv_{sd}, the d-axis reference signal ΔP^{ref} or Δv_{dc}^{ref} and one internal input signal Δi_{dc}.

3.1.1 Weak AC-grid environment

As discussed in subsection 2.1, in two-terminal VSC-HVDC systems, one converter station (VSC1) is assigned the duty as DC voltage controller with input signal Δv_{dc1}^{ref} and the other station (VSC2) operates as the active power controller with input signal ΔP_2^{ref}. Choose the DC voltage as the converter system output. The preliminary transfer functions from those five inputs to the DC voltages are given by:

$$\begin{aligned}\Delta\tilde{v}_{dc1} =& g_{11}(s)\Delta\tilde{v}_{dc1}^{ref} + g_{12}(s)\Delta\tilde{E}_1^{ref} + g_{13}(s)\Delta\tilde{v}_{sd1} + g_{14}(s)\Delta\tilde{v}_{sq1} + \\ &+ g_{15}(s)\Delta\tilde{i}_{dc1} \qquad (3.1)\\ \Delta\tilde{v}_{dc2} =& g_{21}(s)\Delta\tilde{P}_2^{ref} + g_{22}(s)\Delta\tilde{E}_2^{ref} + g_{23}(s)\Delta\tilde{v}_{sd2} + g_{24}(s)\Delta\tilde{v}_{sq2} + \\ &+ g_{25}(s)\Delta\tilde{i}_{dc2} \qquad (3.2)\end{aligned}$$

where, the transfer functions $g_{ij}(s)$ can be calculated through the state space model given by eq.(3.18) in section 3.2.2.

Combining the relationship between the DC terminal currents and voltages given by eq.(2.53), the two-terminal VSC-HVDC system transfer function matrix is readily obtained from:

$$\Lambda(s)\begin{bmatrix}\Delta\tilde{v}_{dc1}\\ \Delta\tilde{v}_{dc2}\end{bmatrix} = \Phi(s) * u \qquad (3.3)$$

$$\Lambda(s) = \begin{bmatrix}1 - g_{15}h_1 & g_{15}h_2\\ g_{25}h_2 & 1 - g_{25}h_1\end{bmatrix}$$

$$\Phi(s) = \begin{bmatrix}g_{11} & g_{12} & 0 & 0 & g_{13} & g_{14} & 0 & 0\\ 0 & 0 & g_{21} & g_{22} & 0 & 0 & g_{23} & g_{24}\end{bmatrix}$$

where, $u^T = [\Delta\tilde{v}_{dc1}^{ref}\ \Delta\tilde{E}_1^{ref}\ \Delta\tilde{P}_2^{ref}\ \Delta\tilde{E}_2^{ref}\ \Delta\tilde{v}_{sd1}\ \Delta\tilde{v}_{sq1}\ \Delta\tilde{v}_{sd2}\ \Delta\tilde{v}_{sq2}]$. The MIMO transfer function from inputs to outputs is given as follows, where $\mathrm{adj}(\Lambda)$ denotes the adjoint matrix of Λ:

$$\begin{aligned}\begin{bmatrix}\Delta\tilde{v}_{dc1}\\ \Delta\tilde{v}_{dc2}\end{bmatrix} &= \Lambda^{-1}\Phi\cdot u = \frac{1}{\det\Lambda}\mathrm{adj}(\Lambda)\Phi\cdot u\\ &= \underbrace{\frac{-\frac{g_{15}+g_{25}}{1+Y_0^2 g_{15}g_{25}}}{1-\frac{g_{15}+g_{25}}{1+Y_0^2 g_{15}g_{25}}\cdot h_1}}_{\text{Feedback loop } \frac{g_1}{1+g_1h_1}}\ \underbrace{\frac{-1}{g_{15}+g_{25}}G(s)}_{\text{Forward function } g_0} *u \qquad (3.4)\end{aligned}$$

$$\begin{aligned} G(s) &= \operatorname{adj}(\Lambda)\Phi \qquad\qquad\qquad\qquad\qquad\qquad\qquad\qquad\qquad\qquad\qquad\qquad (3.5)\\ &= \left[\begin{matrix} g_{11}(1-g_{25}h_1) & g_{12}(1-g_{25}h_1) & -g_{21}g_{15}h_2 & -g_{22}g_{15}h_2 \\ -g_{11}g_{25}h_2 & -g_{12}g_{25}h_2 & g_{21}(1-g_{15}h_1) & g_{22}(1-g_{25}h_1) \end{matrix}\right. \\ &\qquad \left.\begin{matrix} g_{13}(1-g_{25}h_1) & g_{14}(1-g_{25}h_1) & -g_{23}g_{15}h_2 & -g_{24}g_{15}h_2 \\ -g_{13}g_{25}h_2 & -g_{14}g_{25}h_2 & g_{23}(1-g_{25}h_1) & g_{24}(1-g_{25}h_1) \end{matrix}\right] \end{aligned}$$

The feedback loop $g_1/(1+g_1h_1)$ remains the same for all combinations of input and output signals. Since the DC-cable system is dissipative, all poles of h_1 have negative real part and are thus stable. The number of unstable poles of the open loop function of the feedback system, g_1h_1, is then determined by the rational function g_1. Consequently, the Nyquist stability criterion can be applied to analyze the feedback system stability.

The forward path function g_0 is one element of $-G/(g_{15}+g_{25})$, which varies with different input and output signals. Since g_0 will always be a linear non-feedback combination of rational functions and of h_1 or h_2 (h_1 and h_2 have stable poles), the stability of g_0 is determined by a limited number of poles.

Consequently, by transformation into the block diagram in Fig. 3, the VSC-HVDC system stability can be analyzed by the above criteria.

3.1.2 Strong AC-grid environment

While the connected AC-grids are well balanced and strong i.e. the nominal AC-grid voltage is as most subject to small variations, and hence the dynamics of the PLL is ignored. In addition, since the q-axis current has no impact on the dynamics at the DC-side (due to d- and q-dynamics decoupling at the inner current loop), the q-axis reference current signal, Δi_q^{ref}, is thus assumed to be zero.

As before, choose the DC voltage as the converter output, the preliminary transfer functions from the remaining three inputs to its DC terminal voltage are given by:

$$\Delta\tilde{v}_{dc1} = \hat{g}_{11}(s)\Delta\tilde{v}_{dc1}^{ref} + \hat{g}_{13}(s)\Delta\tilde{v}_{sd1} + \hat{g}_{15}(s)\Delta\tilde{i}_{dc1} \tag{3.6}$$

$$\Delta\tilde{v}_{dc2} = \hat{g}_{21}(s)\Delta\tilde{P}_2^{ref} + \hat{g}_{23}(s)\Delta\tilde{v}_{sd2} + \hat{g}_{25}(s)\Delta\tilde{i}_{dc2} \tag{3.7}$$

where, the corresponding transfer functions of the strong AC-grid case are denoted by $\hat{g}_{ij}$, $i = 1,2,\ j = 1,3,5$. Combining the DC-grid dynamics eq.(2.53), the transfer functions from inputs $\hat{u}^T = [\Delta\tilde{v}_{dc1}^{ref}\ \Delta\tilde{P}_2^{ref}\ \Delta\tilde{v}_{sd1}\ \Delta\tilde{v}_{sd2}]$

to $[\Delta\tilde{v}_{dc1}\ \Delta\tilde{v}_{dc2}]^T$ are:

$$\begin{bmatrix}\Delta\tilde{v}_{dc1}\\ \Delta\tilde{v}_{dc2}\end{bmatrix} = \underbrace{\frac{-\frac{\hat{g}_{15}+\hat{g}_{25}}{1+Y_0^2\hat{g}_{15}\hat{g}_{25}}}{1-\frac{\hat{g}_{15}+\hat{g}_{25}}{1+Y_0^2\hat{g}_{15}\hat{g}_{25}}\cdot h_1}}_{\text{Feedback loop } \frac{\hat{g}_1}{1+\hat{g}_1 h_1}} \underbrace{\frac{-1}{\hat{g}_{15}+\hat{g}_{25}}\hat{G}(s)}_{\text{Forward function } \hat{g}_0} *\hat{u} \tag{3.8}$$

$$\hat{G}(s) = \begin{bmatrix} \hat{g}_{11}(1-\hat{g}_{25}h_1) & -\hat{g}_{21}\hat{g}_{15}h_2 & \hat{g}_{13}(1-\hat{g}_{25}h_1) & -\hat{g}_{23}\hat{g}_{15}h_2 \\ -\hat{g}_{11}\hat{g}_{25}h_2 & \hat{g}_{21}(1-\hat{g}_{15}h_1) & -\hat{g}_{13}\hat{g}_{25}h_2 & \hat{g}_{23}(1-\hat{g}_{15}h_1) \end{bmatrix}$$

For both weak and strong AC-environment, the transfer functions of a two-terminal VSC-HVDC system, using a distributed parameter DC-cable model, can always be written into the form $g_0 \cdot g_1/(1+g_1h_1)$. The forward function g_0 is determined by the choice of input and output signal, while the feedback loop is invariant of this choice. Using this approach, the small-signal stability of the infinite dimensional system can in principle always be analyzed by the Nyquist criterion.

3.2 Stability analysis

In order to guarantee the stability of the entire system, both the feedback loop and the outer forward path should be stable. Even though the forward path transfer function $g_0(s)$ is determined by an input-output combination, it will always be a linear non-feedback combination of rational functions and of h_1 or h_2. Thus, the stability of g_0 is determined by the sign of the real parts of a limited number of poles. The stability of the feedback loop is analyzed by use of the Nyquist stability criterion.

Assuming that the closed path $\mathcal{C}$ enclosing all of the right half complex s-plane has the clockwise positive direction, we can apply the Nyquist criterion: The number of anti-clockwise encirclements around the point -1 in the $g_1(s)h_1(s)$-plane should, for a stable closed loop system, equal the number of open loop unstable poles of $g_1(s)$, as $h_1(s)$ is already an input to output stable function [25].

For the active power controlled converter (VSC2), the transfer function $g_{25}(s)$ from Δi_{dc2} to Δv_{dc2} is the same as the converter connected to a strong AC-grid (i.e. $g_{25}(s) = \hat{g}_{25}(s)$). Therefore, the feedback loop stability is not influenced by the weak AC-grid dynamics at the active power controlled converter. Similarly, the stability of the active power controlled converter could be analyzed without considering the DC-side influence. Consequently, the stability analysis of two terminal VSC-HVDC systems embedded in a weak AC-grid can be separated into two parts: the active power controlled converter and the VSC-HVDC system while the active power controlled converter is under steady state. The stability of the first part is further discussed in chapter 4 and the second part is analyzed in this subsection .

3.2.1 VSC-HVDC system connected with a strong AC-grid

For a VSC-HVDC system embedded in strong AC-grid, the preliminary transfer functions from the input signals $\hat{u}^T = [\Delta\tilde{v}_{dc1}^{ref}\ \Delta\tilde{P}_2^{ref}\ \Delta\tilde{v}_{sd1}\ \Delta\tilde{v}_{sd2}]$ to the DC voltages Δv_{dc1} and Δv_{dc2} are given by eq.(3.8) and the preliminary transfer functions are given as follows, where both a_f and a_{df} are assumed to be infinity (i.e. there is no LPF for both the DC load power and the AC voltage) and the d-axis reference current is designed as eq.(2.17):

$$\hat{g}_{11} = \frac{a_c\omega_{nd}C_1(2\zeta s + \omega_{nd})}{C_1 s^2(s+a_c) + a_c\omega_{nd}C_1(2\zeta s + \omega_{nd}) + \frac{i_{dc10}}{v_{dc10}}s^2} \tag{3.9}$$

$$\hat{g}_{13} = \frac{\frac{P_{10}}{E_{10}v_{dc10}}s^2}{C_1 s^2(s+a_c) + a_c\omega_{nd}C_1(2\zeta s + \omega_{nd}) + \frac{i_{dc10}}{v_{dc10}}s^2} \tag{3.10}$$

$$\hat{g}_{15} = -\frac{s^2}{C_1 s^2(s+a_c) + a_c\omega_{nd}C_1(2\zeta s + \omega_{nd}) + \frac{i_{dc10}}{v_{dc10}}s^2} \tag{3.11}$$

$$\hat{g}_{21} = \frac{a_p}{(C_2 v_{dc20}s + i_{dc20})(s+a_p)} \tag{3.12}$$

$$\hat{g}_{23} = \frac{\frac{P_{20}}{E_{20}}s}{(C_2 v_{dc20}s + i_{dc20})(s+a_p)} \tag{3.13}$$

$$\hat{g}_{25} = -\frac{v_{DC20}}{C_2 v_{dc20}s + i_{dc20}} \tag{3.14}$$

For each single input single output system, the forward path function $\hat{g}_0$ is one element of $-\hat{G}/(\hat{g}_{15}+\hat{g}_{25})$. From eq.(3.9) to eq.(3.14), it shows that $\hat{g}_{11}$, $\hat{g}_{13}$, $\hat{g}_{15}$ have similar pole polynomial and similarly for $\hat{g}_{21}$, $\hat{g}_{23}$ and $\hat{g}_{25}$ except one stable pole $-a_p$. In addition, h_1 and h_2 are stable. The stability of the forward path depends on the zero polynomial $Q_3(s)$ of $\hat{g}_{15}+\hat{g}_{25}$:

$$Q_3(s) = (C_1+C_2)s^3 + (C_1 a_c + \frac{i_{dc10}}{v_{dc10}} + \frac{i_{dc20}}{v_{dc20}})s^2 + a_c k_{pd}s + a_c k_{id} \tag{3.15}$$

To guarantee that the zeros of $Q_3(s)$ are located in the left half plane, the following inequality, resulting from the Routh stability criterion [25], must hold:

$$\frac{C_1 a_c + \frac{i_{dc10}}{v_{dc10}} + \frac{i_{dc20}}{v_{dc20}}}{C_1+C_2} > \frac{k_{id}}{k_{pd}} = \frac{\omega_{nd}}{2\zeta} = 0.2a_d \tag{3.16}$$

At steady state $i_{dc10} = -i_{dc20}$, and to minimize transmission losses, the DC voltage drop between two terminals should be kept small. Moreover, the bandwidth of the inner current loop a_c is designed to be ten times larger than the DC voltage loop i.e. $a_c = 10a_d$. Therefore the inequality eq.(3.16) holds for all reasonable designs of PI-controllers and the forward path $\hat{g}_0$ for all input-output combinations are thus stable in case of strong AC-grid environment. The stability of the strong AC grid connected VSC-HVDC system is thus determined by the feedback system $\hat{g}_1/(1+\hat{g}_1h_1)$.

In the feedback loop, $\hat{g}_1(s)$ is a rational function with respect to 's' and $h_1(s)$ is input to output stable. Therefore, the number of unstable poles of the open loop transfer function $\hat{g}_1h_1$ is determined by $\hat{g}_1$, where $\hat{g}_1$ is:

$$\begin{aligned}
\hat{g}_1(s) &= \frac{Q_3(s)(l_cs+r_c)}{P_5(s)} \\
P_5(s) &= (l_cs+r_c)(C_2s+\frac{i_{dc20}}{v_{dc20}})[C_1s^3+(C_1a_c+\frac{i_{dc10}}{v_{dc10}})s^2+a_ck_{pd}s+a_ck_{id}]+ \\
&\quad + s^2(c_cs+g_c)
\end{aligned}$$

In the case study setup, the physical and the control parameters of the VSC-HVDC system are listed in Tab. 1 and Tab. 1. There are two cases that will be discussed in this subsection: one example is using the rectifier (AC→DC) as DC voltage controller (standard situation) and the other is using the inverter (DC→AC) as DC voltage controller.

- Rectifier performs as the DC voltage controller

If the rectifier controls the DC voltage and the inverter controls the transmitted active power, the steady states are $v_{dc10} = 300$ [kV] and $P_{20} = -600$ [MW]. The poles of $\hat{g}_1(s)$ with different cable distances $d = 50$, 150, 450 [km] are given in Table 3.3. For all three cable distances, there is one unstable pole of the open loop transfer function $\hat{g}_1(s)h_1(s)$.

Table 3.3: Poles of $\hat{g}_1(s)$ with P_{20}=-600MW

d	Poles of $g_1(s)$				
50	23.9	-3.3+3.4j	-3.3-3.4j	-206.8+954j	-206.8-954j
150	25.3	-3.3+3.5j	-3.3-3.5j	-204.5+951j	-204.5-951j
450	31.3	-3.3+3.5j	-3.3-3.5j	-194.7+938j	-194.7-938j

The Nyquist plots of the transfer functions $\hat{g}_1(j\omega)h_1(j\omega)$ with different cable distances are given in Fig. 3.2. It shows that for all three cases, $\hat{g}_1(j\omega)h_1(j\omega)$ anti-clockwise encircles the critical point (-1,0) once, which is equal to the number of unstable poles of $\hat{g}_1(s)h_1(s)$. Consequently, for the different cable distances, $d = 50,\ 150,\ 450$ [km], the VSC-HVDC system remains stable at the operational point $v_{dc10} = 300$ [kV] and $P_{20} = -600$ [MW]. (For other operating points of both DC-voltage and active power, the VSC-HVDC system still appears to be stable.)

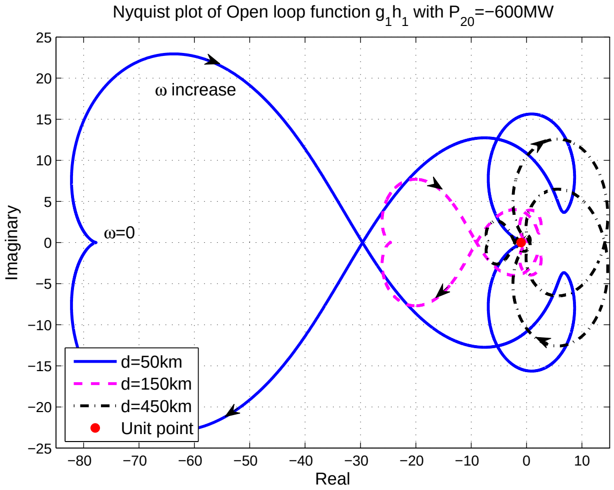

(a)Full curve

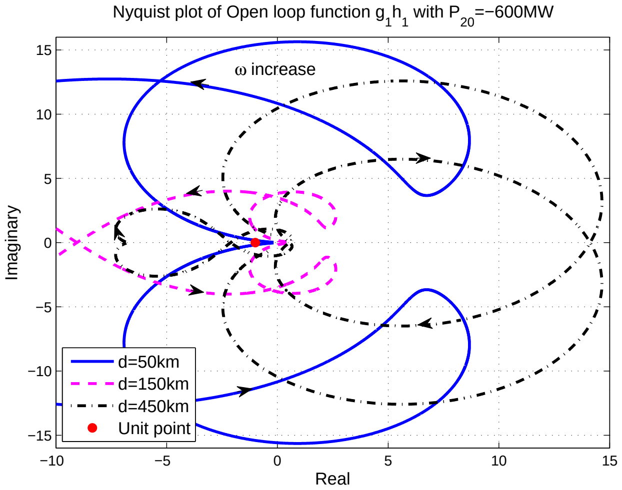

(b)Amplified around critical point (-1,0)

Figure 3.2: Nyquist plot of $\hat{g}_1(j\omega)h_1(j\omega)$ with $P_{20} = -600MW$: blue solid curve is d=50 km; red dashed curve is d=150 km; black dashed dotted curve is d=450 km; the critical point (-1,0) is marked by a red dot.

- Inverter performs as the DC voltage controller

If instead the inverter controls the DC voltage and the rectifier controls the transmitted active power, the steady states are $v_{dc10} = 300$ [kV] and

$P_{20} = 600$ [MW]. The poles of $\hat{g}_1(s)$ with different cable distances are given in Table 3.4. For all three cases, there are two unstable poles of the open loop transfer function $\hat{g}_1(s)h_1(s)$.

Table 3.4: Poles of $\hat{g}_1(s)$ with $P_{20} = 600$ [MW]

d	Poles of $\hat{g}_1(s)$				
50	1.2+11.5j	1.2-11.5j	-3.6	-198+994j	-198-994j
150	1.1+11.3j	1.1-11.3j	-3.6	-195+995j	-195-995j
450	0.95+10.6j	0.95-10.6j	-3.6	-190+996j	-190-996j

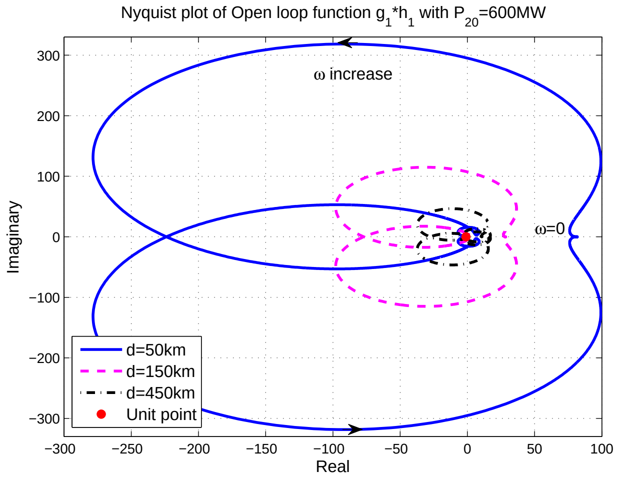

(a)Full curve

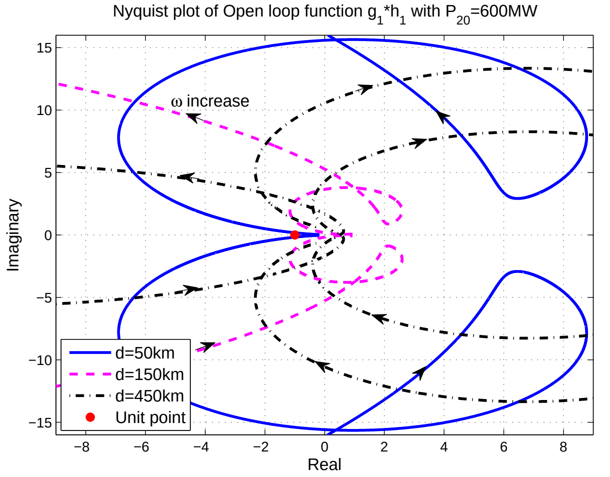

(b)Amplified around critical point (-1,0)

Figure 3.3: Nyquist plot of $\hat{g}_1(j\omega)h_1(j\omega)$ with $P_{20} = 600MW$

The Nyquist plots of the transfer functions $\hat{g}_1(j\omega)h_1(j\omega)$ with different cable distances are given in Fig. 3.3. It shows that for all three cases, $\hat{g}_1(j\omega)h_1(j\omega)$ anti-clockwise encircles the critical point (-1,0) twice, which is equal to the number of unstable poles of $\hat{g}_1(s)h_1(s)$. Consequently, for the different cable distances, $d = 50$, 150, 450 [km], the VSC-HVDC system remains stable when $v_{dc10} = 300$ [kV] and $P_{20} = 600$ [MW].

According to above analysis, the VSC-HVDC system embedded in a strong AC grid will be stable for three different cable distances $d = 50$, 150, 450 [km]. The corresponding conclusion can be made when using the single Π-section cable model. The distributed parameter cable model, hence justifies the use of the single Π-model in most situations.

3.2.2 VSC-HVDC system connected with a weak AC-grid

As concluded above, the stability of the active power controlled VSC would not influence the stability of the feedback loop $g_1/(1+g_1h_1)$ since $g_{25} = \hat{g}_{25}$. In this subsection, it is assumed that the active power controlled VSC is under steady state. On the other terminal, the DC-voltage controlled VSC is connected to a weak AC-grid, which is modeled by a series L_gR_g-circuit. In the synchronous coordinates, the AC grid dynamics are given by eq.(2.34-2.35).

The comparison stability result between a VSC-HVDC system with one single Π-section DC-cable model and with distributed DC-cable model is presented in this subsection, where the LPF of the AC-voltage is not considered (i.e. $a_f \to \infty$ and $y_i(s) \approx 0$) and the d-axis reference current is designed as eq.(2.17), the q-axis outer control loop is designed by $K_{ad}(s) = k_{pa}$ and $K_{aq}(s) = 0$.

- Single Π-section DC-cable model:

While the DC-cable is modeled by one single Π-section, the VSC-HVDC system embedded in weak AC-grid at the DC-voltage controlled converter side, could be modeled by an eighth-order state space model. The state variables are $x_{dv}^T = [\Delta i_{cd}\ \Delta i_{cq}\ \Delta v_{dc1}\ x_{dv4}\ x_{dv5}\ x_{pll}\ \Delta i_{dc}\ \Delta v_{dc2}]$, where x_{dv4} is the integral action of the DC-voltage controller, x_{dv5} is the dynamics of the LPF of the forward DC load power and Δv_{dc2} is the DC-voltage at the active power controlled converter side. The input variables are $u_{dv}^T = [\Delta v_{dc1}^{ref}\ \Delta E^{ref}\ \Delta v_{sd}\ \Delta v_{sq}]$ and the disturbance input variables are $w^T = [\Delta E_d\ \Delta E_q]$. u_{dv}^{ref} are the first two reference signals of the input vector u_{dv}.

Combine the inner current loop dynamics eq.(2.7-2.8), the DC-voltage dynamics eq.(2.10), the DC-voltage controlled outer loop dynamics eq.(2.15, 2.17), the PLL dynamics eq.(2.30-2.33), the DC-current dynamics due to series $R_{dc}L_{dc}$-circuit and the active power controlled VSC dynamics given by $g_{25}(s)$, the state-space model of the VSC-HVDC system with a single Π-section DC-cable model is given by eq.(3.17), where $C_{tot} = C + C_{dc}$ and $C_{dc} = d \cdot c_c/2$.

$$\begin{aligned}
\dot{x}_{dv} &= A_1 \cdot x_{dv} + B_{u1} \cdot u_{dv}^{ref} + B_{w1} \cdot w \\
w &= C_{w1} \cdot x_{dv} + D_{w1} \cdot u_{dv}
\end{aligned} \tag{3.17}$$

$$A_1 = \begin{bmatrix}
-a_c & 0 & -k_{pd}\frac{v_{dc10}}{E_{10}}a_c & k_{id}\frac{v_{dc10}}{E_{10}}a_c & \frac{a_c}{E_{10}} & 0 & 0 & 0 \\
0 & -a_c & 0 & 0 & 0 & 0 & 0 & 0 \\
\frac{E_{10}}{C_{tot}v_{dc10}} & 0 & -\frac{i_{dc0}}{C_{tot}v_{dc10}} & 0 & 0 & \frac{Q_{10}/E_{10}}{C_{tot}v_{dc10}} & -\frac{1}{C_{tot}} & 0 \\
0 & 0 & -1 & 0 & 0 & 0 & 0 & 0 \\
a_{df}E_{10}\frac{C_{dc}}{C_{tot}} & 0 & a_{df}i_{dc0}\frac{C}{C_{tot}} & 0 & -a_{df} & a_{df}E_{10}\frac{C_{dc}}{C_{tot}}\frac{Q_{10}}{E_{10}^2} & a_{df}v_{dc10}\frac{C}{C_{tot}} & 0 \\
0 & 0 & 0 & 0 & 0 & -a_{pll} & 0 & 0 \\
0 & 0 & \frac{1}{L_{dc}} & 0 & 0 & 0 & -\frac{R_{dc}}{L_{dc}} & -\frac{1}{L_{dc}} \\
0 & 0 & 0 & 0 & 0 & 0 & \frac{1}{C_{tot}} & \frac{i_{dc0}}{C_{tot}v_{dc20}}
\end{bmatrix}$$

$$B_{u1}^T = \begin{bmatrix}
k_{pd}\frac{v_{dc10}}{E_{10}}a_c & 0 & 0 & 1 & 0 & 0 & 0 & 0 \\
0 & a_c k_{pa} & 0 & 0 & 0 & 0 & 0 & 0
\end{bmatrix}$$

$$B_{w1}^T = \begin{bmatrix}
-a_c\frac{P_{10}}{E_{10}^2} & -a_c k_{pa} & \frac{P_{10}/E_{10}}{C_{tot}v_{dc10}} & 0 & a_{df}\frac{C_{dc}}{C_{tot}}\frac{P_{10}}{E_{10}^2} & 0 & 0 & 0 \\
0 & 0 & -\frac{Q_{10}/E_{10}}{C_{tot}v_{dc10}} & 0 & -a_{df}\frac{C_{dc}}{C_{tot}}\frac{Q_{10}}{E_{10}^2} & a_{pll} & 0 & 0
\end{bmatrix}$$

$$C_{w1} = \frac{L_g}{k_1}\begin{bmatrix}
1 + a_{pll}L_g\frac{P_{10}}{E_{10}^2} & -a_{pll}L_g\frac{Q_{10}}{E_{10}^2} \\
a_c L_g k_{pa} & 1 - a_c L_g\frac{P_{10}}{E_{10}^2}
\end{bmatrix} \cdot \begin{bmatrix}
a_c - \frac{R_g}{L_g} & \omega_0 & k_{pd}\frac{v_{dc10}}{E_{10}}a_c & -k_{id}\frac{v_{dc10}}{E_{10}}a_c & -\frac{a_c}{E_{10}} & \omega_0\frac{P_{10}}{E_{10}^2} + \frac{Q_{10}}{E_{10}^2}(a_{pll} - \frac{R_g}{L_g}) & 0 & 0 \\
-\omega_0 & a_c - \frac{R_g}{L_g} & 0 & 0 & 0 & (a_{pll} - \frac{R_g}{L_g})\frac{P_{10}}{E_{10}^2} - \frac{Q_{10}}{E_{10}^2}\omega_0 & 0 & 0
\end{bmatrix}$$

$$D_{w1} = \frac{1}{k_1}\begin{bmatrix}
1 + a_{pll}L_g\frac{P_{10}}{E_{10}^2} & -a_{pll}L_g\frac{Q_{10}}{E_{10}^2} \\
a_c L_g k_{pa} & 1 - a_c L_g\frac{P_{10}}{E_{10}^2}
\end{bmatrix}\begin{bmatrix}
-k_{pd}\frac{v_{dc10}}{E_{10}}a_c L_g & 0 & 1 & 0 \\
0 & -a_c k_{pa} L_g & 0 & 1
\end{bmatrix}$$

$$k_1 = 1 + L_g(a_{pll} - a_c)\frac{P_{10}}{E_{10}^2} + L_g^2 a_{pll} a_c (k_{pa}\frac{Q_{10}}{E_{10}^2} - \frac{P_{10}^2}{E_{10}^4})$$

A_1, B_{u1} and B_{d1} do not depend on the AC-grid SCR, however that C_{d1} and D_{d1} depend on it. The parameters of the DC-cable are listed in Tab. 1 and Tab. 1, where $L_{dc} = l_c * d$ and $R_{dc} = r_c * d$. The stability of the VSC-HVDC system with a single Π-section DC cable model can be analyzed by the eigenvalues of $A_1 + \Delta A_1$ and $\Delta A_1 = B_{w1} C_{w1}$.

It's straight forward to be calculated that for SCR < 4, provided the parameter values in Tab. 1 and Tab. 1, the VSC-HVDC system will become unstable due to the weak AC-grid impedance but not for the case with higher SCR. The reason for the system instability is that $k_1 \to \infty$ and thus $||\Delta A_1||_\infty \to \infty$ when SCR $= 1/L_g$ [p.u.] is around a_c i.e. 4 [p.u.].

- Distributed parameter DC-cable model:

While the DC-cable is modeled by eq.(2.53), it is hard to use eigenvalue analysis to study the system stability since there are an infinite number of poles. Therefore, the Nyquist criterion is applied to analyze the stability of the system in the block diagram in Fig. 3.

As claimed in subsection 3.1, the VSC-HVDC system can be described by two cascaded systems: one is a forward combination of transfer functions, which depends on the considered input and output. The second is a feedback loop which is unique for all input-output combinations. When the active power controlled converter is operated under steady state, the transfer function at VSC2 is simplified as $\Delta v_{dc2} = g_{25}(s)\Delta i_{dc2}$, which would not induce an unstable forward function $g_0(s)$. For the DC-voltage controlled VSC, the forward function stability will be analyzed by a case study.

In the case study setup, the VSC-HVDC system parameters and nominal steady states are listed in Tab. 1 and Tab. 1. However, change the cable inductance density to be 10.2 [mH/km] (other parameters as in Tab. 1 and Tab. 1), which renders the single Π-section cable model based VSC-HVDC system unstable and the SCR of the AC-grid is still chosen to be 4. For the case with distributed parameter DC-cable model, the forward function stability and the function g_{15} are determined by the new state-space model, where x_{dvn} is the first six components of x_{dv}, the input signal is Δi_{dc} and the output signal is Δv_{dc},

$$
\begin{aligned}
\dot{x}_{dvn} &= A_2 \cdot x_{dvn} + B_2 \cdot \Delta i_{dc} \\
\Delta v_{dc1} &= C_2 \cdot x_{dvn} && (3.18) \\
g_{15} &= C_2 (sI - A_2)^{-1} B_2 && (3.19)
\end{aligned}
$$

where A_2 is the sub-square matrix of $A_1 + \Delta A_1$ with the first 6 columns and first 6 rows and $C_{dc} = 0$ [μF] (since the cable capacitance should not be included in the VSC dynamics itself), and B_2, C_2 are:

$$\begin{aligned} B_2^T &= \begin{bmatrix} 0 & 0 & -\frac{1}{C} & 0 & a_{df} v_{dc10} & 0 \end{bmatrix} \\ C_2 &= \begin{bmatrix} 0 & 0 & 1 & 0 & 0 & 0 \end{bmatrix} \end{aligned}$$

It is straight forward to prove that the above system eq.(3.18) is minimum order, i.e. the system is both controllable and observable. Therefore, the stability of the forward function $g_0 = \frac{-1}{g_{15}+g_{25}} G(s)$ is determined by the zeros of $g_{15}+g_{25}$. The expression of g_{25} is given by eq.(3.14), as $g_{25} = \hat{g}_{25}$ and the expression of g_{15} is given by eq.(3.19). In this case study, the zeros of $g_{15}+g_{25}$ are -30, $-41 \pm 66j$, -119, -1265, -466180 and thus the forward function $g_0(s)$ is always stable regardless of the input and output signals. Note that the system zero with large magnitude ($z = -466180$) is due to the fact that k_1 is small when SCR is around 4.

The feedback loop stability is studied by the Nyquist criterion. The number of unstable poles of $g_1 h_1$ is determined by $g_1 = -\frac{g_{15}+g_{25}}{1+Y_0^2 g_{15} g_{25}}$ due to that $h_1(s)$ is dissipative, containing an infinite number of stable poles. The poles of g_1 are: 173, -0.98, $-25 \pm 22j$, -119, -434, -1125 and -449937. Obviously, there is one unstable pole of the open loop function of $g_1/(1+g_1 h_1)$. In order to guarantee the stability of the closed loop function, the Nyquist plot should anti-clockwise encircle the critical point (-1,0) once. For the single Π-section cable model, the equivalent cable function of $h_1(s)$ is depicted by $h_{\pi 1}(s) = c_c s \cdot d/2 + 1/(l_c s + r_c)/d$. The Nyquist curve of the open loop function $g_1 h_1(j\omega)$ and $g_1 h_{\pi 1}(j\omega)$ is given by Fig. 7.

Fig. 7 (a) shows that in the low frequency band, both cable models provide similar Nyquist curves. However, in this study case, the Fig. 7 (b) shows that for the distributed parameter cable model, the Nyquist curve will anti-clockwise encircle the critical point (-1,0) but for the single Π-section cable model, the Nyquist curve will clockwise encircle the critical point once. Therefore, the VSC-HVDC system with distributed parameter DC cable is stable but the VSC-HVDC system with one single Π-section DC cable model has two unstable poles i.e. $0.7 \pm 1.78j$, which are calculated by the eigenvalue of the weak AC-grid connected VSC-HVDC system state matrix $A_1 + \Delta A_1$.

This is because, for $\omega < 1/(d\sqrt{l_c c_c/2}) = \omega_{rf}$ (resonance frequency of the single Π-section model), $|h_1(j\omega)| > |h_{\pi 1}(j\omega)|$ implying that the VSC-HVDC system with the distributed parameter cable model has a larger gain margin.

Fig. 8. shows that if the VSC-HVDC system with the single Π-section model is stable, then the phase crossover frequency must be lower than ω_{rf} where $h_1(j\omega)$ is similar to $h_{\pi 1}(j\omega)$ and since $g_1 h_1$ has a larger gain margin, the VSC-HVDC system with the distributed parameter cable model is also

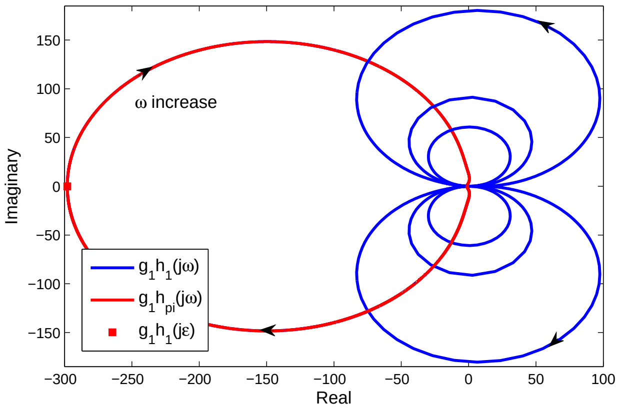

(a)Full curve

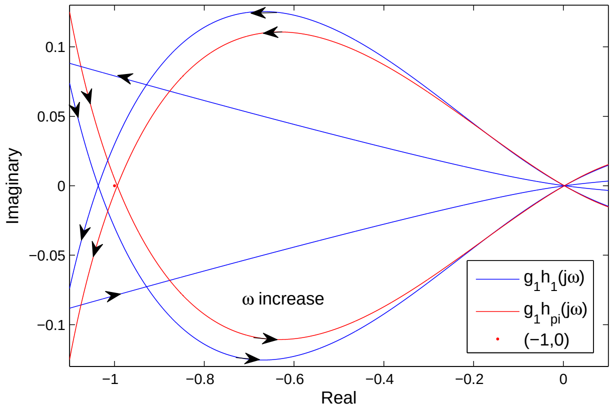

(b)Amplified around critical point (-1,0)

Figure 3.4: Nyquist plot of $g_1(j\omega)h_1(j\omega)$: one Π-section DC-cable model (red curve); distributed parameter DC-cable model (blue curve).

stable. Consequently, if the VSC-HVDC system with a single Π-section model is stable, it is sufficient for the VSC-HVDC system with distributed parameter cable model to be stable but not vice versa.

For different operating points P_{20} and for different SCRs, the open loop function g_1h_1 always has one unstable pole, which implies that the Nyquist curve should anti-clockwise encircle the critical point (-1,0) once, so that the closed loop VSC-HVDC system is stable. As shown in Fig. 7, the Nyquist curve should cross the negative real axis at the left of (-1,0) in order to anti-clockwise encircle the critical point. Therefore, the larger magnitude of $|g_1h_1(j\omega_{pc})|$ is, the better stability robustness the system will have. ω_{pc} is the phase crossover frequency, i.e. the angle of $g_1h_1(j\omega_{pc})$ is -180 [deg].

Fig. 9 illustrates the difference in loop transfer function gain, for the

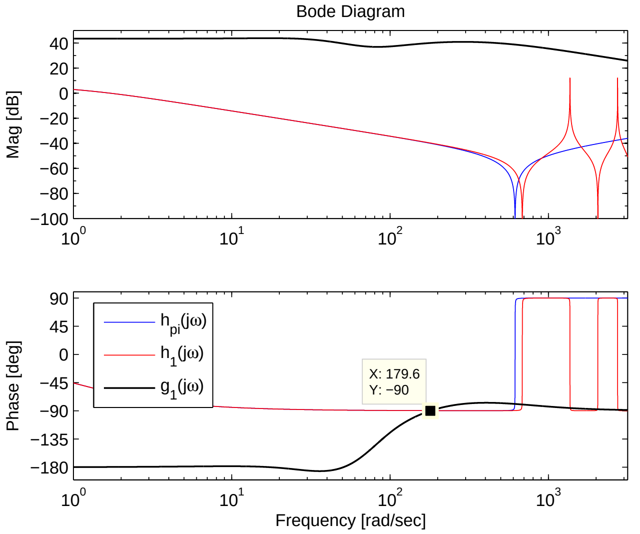

Figure 3.5: Frequency characteristic curve of $g_1(j\omega)$, $h_1(j\omega)$ and $h_{\pi 1}(j\omega)$.

two cases (distributed model and Π-section model) at ω_{pc}, ω_{pc}^{π}, respectively. Positive difference values imply that $|g_1 h_1(j\omega_{pc})| > |g_1 h_{\pi 1}(j\omega_{pc}^{\pi})|$. It shows that the VSC-HVDC system with one Π-section DC cable model always has worse stability robustness for different operating points P_{20} and for different SCRs. Consequently, the VSC-HVDC system with a single Π-section DC cable is a safe choice in the evaluation of system stability under different P_{20} and SCR.

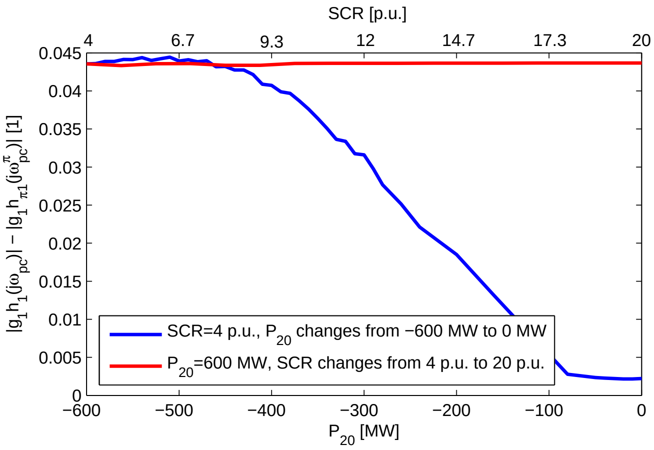

Figure 3.6: Magnitude differences between $|g_1 h_1(j\omega_c)|$ and $|g_1 h_{\pi 1}(j\omega_{c\pi})|$, where the angle of both $g_1 h_1(j\omega_c)$ and $g_1 h_{\pi 1}(j\omega_{c\pi})$ are −180°.

Chapter 4

Robust stability analysis

As shown in subsection 3.2.2, the interconnected AC-grid may adversely decrease the VSC-HVDC system robustness and cause instability. Therefore, in this section, the stability of grid connected converters are analyzed based on the small gain theorem and the passivity theorem, where the system is characterized as a negative feedback system of grid impedance and converter admittance as shown in Fig. 4.1.

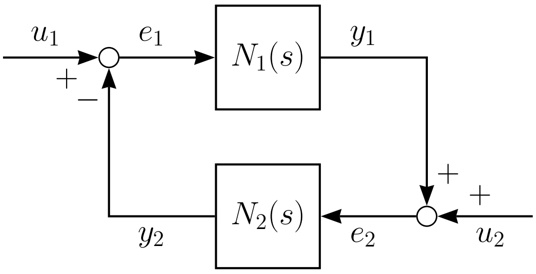

Figure 4.1: Block diagram of the grid connected converter system: converter admittance system $N_1(s)$ and AC-grid impedance system $N_2(s)$.

4.1 Mixed small gain and passivity theorem

The small gain theorem and the passivity theorem are two of the most important results in the input-output stability theory of interconnected systems. However, there exist many situations where both the passivity and the small gain theorems are not compatible respectively, the idea of merging those two theorems is potentially extremely useful. In this section, a modified “mixed” small gain and passivity theorem is proposed and will be further applied to give sufficient conditions for the stability of a two-terminal VSC-HVDC system embedded in weak AC-grids.

The small gain theorem and the passivity theorem are given as follows [9, 26–30]:

Theorem 1 (Small gain theorem)
Consider a system with a stable loop transfer function $L(s)$. *Then the closed-loop system is stable if*

$$||L(j\omega)|| < 1, \ \forall\omega \in \mathbb{R}$$

where $||L||$ *denotes any matrix norm satisfying* $||N_1 N_2|| < ||N_1|| \cdot ||N_2||$.

Theorem 2 (Passivity theorem)
Consider two linear time invariant (LTI) stable subsystems N_1 *and* N_2 *in negative feedback configuration, as shown in Fig. 4.1. The closed-loop system is asymptotically stable if both subsystems are passive and at least one of them is strictly passive.* $N_1(s)$ *is passive if and only if* $N_1(j\omega)+N_1^H(j\omega) \geq 0$, *for* $\forall\omega$ *and is strictly passive if and only if* $N_1(j\omega) + N_1^H(j\omega) \geq \delta > 0$, *for* $\forall\omega$. $N_i^H(j\omega)$ *is the Hermitian transpose of* $N_i(j\omega)$.

For LTI systems, both the small gain theorem and the passivity theorem follow from the classical Nyquist criterion, which claims that for stable subsystems as depicted in Fig. 4.1, the Nyquist curve of the loop function $L(s) = N_1(s)N_2(s)$ should not encircle the critical point in order to guarantee the input-output stability of the negative feedback system. Therefore, assume that there are no internal right half plane (RHP) pole-zero cancelation in the loop function $L(s)$, i.e. $L(s)$ contains no unstable hidden modes, then the generalized (MIMO) Nyquist theorem is formulated [31]:

Theorem 3 (Generalized MIMO Nyquist theorem)
Assume that there are no open-loop RHP poles in the loop gain L(s). Then the closed-loop system $(I+L(s))^{-1}$ *is stable if and only if the Nyquist plot of* $\det(I + L(s))$ *(i) makes no anti-clockwise encirclements of the origin, and (ii) does not pass through the origin.*

It is obvious that in the generalized MIMO Nyquist theorem, both $N_1(s)$ and $N_2(s)$ can be non-proper but stable, so that there are no hidden unstable poles in $N_1(s)$ and $N_2(s)$ due to cancelation. Since the "mixed" small gain and passivity theorem follows from the classical Nyquist arguments, there is no need to require both subsystems to be proper as shown in [10, 11]. In addition, the high frequency dynamics of the system studied in [10] destroy the passivity property and thus the system stability is established if gains are small in the high frequency band and passivity holds in the low frequency band which is contrary to our study case (i.e. passivity holds in the high frequency band and gains are small in the low frequency band). Consequently, the new proposed "mixed" small gain and passivity theorem does not require both subsystems to be causal.

Another strong condition of the "mixed" small gain and passivity theorem presented in [10, 11] is that both subsystems has to be input and output strictly passive in the frequency interval Ω_p, where $N(j\omega)$ is input and output strictly passive in the frequency band Ω_p if $\exists k,\ l > 0$ such that $-kN^H(j\omega)N(j\omega) + N^H(j\omega) + N(j\omega) - lI \geq 0$ for $\forall \omega \in \Omega_p$. It is obvious that, for strictly proper system, it is not input and output strictly proper for $\omega \to \infty$. However, if Ω_p only contains bounded frequency bands (i.e. $\pm\infty \notin \Omega_p$), then input and output strict passivity is equivalent to strict passivity, i.e. $N^H(j\omega) + N(j\omega) > 0$ if and only if $-kN^H(j\omega)N(j\omega) + N^H(j\omega) + N(j\omega) - lI \geq 0$ for $\forall \omega \in \Omega_p$. Therefore, in this thesis, the condition of input and output strictly passivity for both subsystems $N_1(s)$ and $N_2(s)$ is released as both of them are passive and at least one of them is strictly passive (which is the same as the condition of the passivity theorem).

The resulting "mixed" small gain and passivity theorem, modified according to the reasons given above is:

Theorem 4 ("Mixed" small gain and passivity theorem)
Suppose that in the open-loop gain $L(s) = N_1(s)N_2(s)$, $N_1(s)$ *and* $N_2(s)$ *are stable rational square transfer function matrices. In addition, there exist two distinct sets of frequency bands: (a) one set denoted by* Ω_p *that consists of frequency intervals over which* $N_i(j\omega)+N_i^H(j\omega) \geq 0,\ i = 1, 2$ *and at least one of them is strictly positive. (b) one set denoted by* Ω_s *that consists of frequency intervals over which* $\bar{\sigma}(N_1(j\omega))\bar{\sigma}(N_2(j\omega)) < 1$. *Then the negative feedback loop (Fig. 4.1) is stable if* $\Omega_p \cup \Omega_s = \mathbb{R} \cup \pm\infty$.

In order to prove Theorem 4, the required observation is given as below:

Lemma 1 (Observation 5 in [11])
Suppose that the Nyquist plot of $\det(I + L(s))$ *encircles the origin at least once. Then there must exist at least one* $\kappa_0 > 1$ *and one* ω_0 *for which* $\det(I + \frac{1}{\kappa_0}L(j\omega_0)) = 0$.

Proof: For an asymptotically stable system $(I+L(s)^{-1})$, *it must satisfied that* $\det(I+L(0)^{-1}) \neq 0$. *Assume that* $\det(I+L(0)^{-1}) > 0$ *and that the Nyquist plot of* $\det(I + L(s))$ *encircles the origin at least once, then the Nyquist plot of* $\det(I + L(s))$ *must cross the negative real axis at leat once. (If* $\det(I + L(0)^{-1}) < 0$, *then neither small gain nor passivity conditions will hold.)*

It implies that there exists at least one positive real number $\varepsilon > 0$ *and one frequency* ω_0, *such that* $\det(I+L(j\omega_0)) = -\varepsilon < 0$. *The invertible matrix*

$Q(s)$ consists of the eigenvectors of $L(s)$ and $\lambda_i(s)$ are the eigenvalues of $L(s)$. Then:

$$\begin{aligned}\det(I + L(s)) &= \det(Q(s)^{-1} \cdot (I + L(s)) \cdot Q(s))\\ &= \det(I + Q(s)^{-1}L(s))Q(s))\\ &= \Pi_{i=1}^{n}(1 + \lambda_i(s))\\ \Rightarrow \det(I + L(j\omega_0)) &= \Pi_{i=1}^{n}(1 + \lambda_i(j\omega_0)) < 0\end{aligned}$$

Therefore, it exists at leat one λ_j such that $1 + \lambda_j(j\omega_0) = -k < 0$, where k is a positive real number. Note that for all conjugate eigenvalue pair $\lambda_m(j\omega_0)$, $\lambda_n(j\omega_0)$, it has $(1+\lambda_n(j\omega_0))(1+\lambda_m(j\omega_0))$ is a positive real number and thus the negative term in $\det(I + L(j\omega_0))$ must comes from the real eigenvalue $\lambda_j(j\omega_0)$ but not the complex one.

In addition, since $1 + \lambda_j(j\omega_0) = -k < 0$, choose $\kappa_0 = 1 + k > 1$, it follows that $1 + \frac{1}{\kappa_0}\lambda_j(j\omega_0) = 0$ and thus $\det(I + \frac{1}{\kappa_0}L(j\omega_0)) = 0$. □

Thus, a sufficient condition for a stable closed-loop system $(I + L(s))^{-1}$ is that, for all $\kappa \geq 1$ and all $\omega \in \mathbb{R} \cup \pm\infty$, $\det(I + \frac{1}{\kappa}L(j\omega)) \neq 0$ provided that the open-loop gain $L(s)$ is stable (according to Theorem 3). Our aim is to show the conditions of $N_1(s)$ and $N_2(s)$ given in Theorem 4, such that $L(s) = N_1(s)N_2(s)$ satisfies the sufficient condition. It is obvious that $N_1(s)$ or $N_2(s)$ can be non-causal but stable, provided there is no hidden unstable pole in $N_1(s)$ or $N_2(s)$ due to cancelation. Note that the similar proof can be found in [11,32].

Proof of Theorem 4:

Part (a): $\forall\omega \in \Omega_p$, assume that $N_1(j\omega) + N_1^H(j\omega) > 0$ and $N_2(j\omega) + N_2^H(j\omega) \geq 0$. Then we want to prove that for all $\kappa \geq 1$ and all $\omega \in \Omega_p$, $\det(I + \frac{1}{\kappa}L(j\omega)) \neq 0$.

Since $N_1(j\omega) + N_1^H(j\omega) > 0$, $N_1(j\omega)$ is nonsingular for $\forall\omega \in \Omega_p$ [33]. Then for $\forall\omega \in \Omega_p$, it follows:

$$\begin{aligned}&N_1^{-1}(j\omega) + N_1^{-H}(j\omega) > 0 \text{ and } \det(N_1^{-1}(j\omega)) \neq 0 \quad \Rightarrow\\ &N_1^{-1}(j\omega) + \frac{1}{\kappa}N_2(j\omega) + N_1^{-H}(j\omega) + \frac{1}{\kappa}N_2^H(j\omega) > 0,\ \forall\kappa \in [1,\infty) \quad \Rightarrow\\ &\det(N_1^{-1}(j\omega) + \frac{1}{\kappa}N_2(j\omega)) = \det(N_1^{-1}(j\omega))\det(I + \frac{1}{\kappa}N_1(j\omega)N_2(j\omega)) \neq 0\end{aligned}$$

$$\therefore \quad \det(I + \frac{1}{\kappa}N_1(j\omega)N_2(j\omega)) \neq 0,\ \forall\kappa \in [1,\infty)$$

Part (b): $\forall\omega \in \Omega_s$, we want to prove that if $\bar{\sigma}(N_1(j\omega))\bar{\sigma}(N_2(j\omega)) < 1$, then for all $\kappa \geq 1$ and all $\omega \in \Omega_s$, $\det(I + \frac{1}{\kappa}L(j\omega)) \neq 0$.

For any $\kappa \geq 1$, it follows:

$$\begin{aligned}
\underline{\sigma}(I + \frac{1}{\kappa}L(j\omega)) &= \min_{||x||_2=1} ||(I + \frac{1}{\kappa}L(j\omega)) \cdot x||_2 \\
&\geq \min_{||x||_2=1} (||x||_2 - ||\frac{1}{\kappa}L(j\omega) \cdot x||_2) \\
&\geq 1 - \max(||\frac{1}{\kappa}L(j\omega) \cdot x||_2) \\
&\geq 1 - \bar{\sigma}(\frac{1}{\kappa}L(j\omega))
\end{aligned}$$

As $\kappa \geq 1$, we have that:

$$\bar{\sigma}(\frac{1}{\kappa}L(j\omega)) \leq \bar{\sigma}(L(j\omega)) \leq \bar{\sigma}(N_1(j\omega))\bar{\sigma}(N_2(j\omega)) < 1$$

Therefore, $\underline{\sigma}(I + \frac{1}{\kappa}L(j\omega)) > 0$ and $\det(I + \frac{1}{\kappa}L(j\omega)) \neq 0$ for $\forall \omega \in \Omega_p$ and $\forall \kappa \geq 1$.

Consequently, if $\Omega_p \cup \Omega_s = \mathbb{R} \cup \pm\infty$, then for all $\kappa \geq 1$ and all $\omega \in \mathbb{R} \cup \pm\infty$, $\det(I + \frac{1}{\kappa}L(j\omega)) \neq 0$. According to Theorem 3 and Lemma 1, the closed loop $(1 + L(s))^{-1}$ is stable. □

Note that the passivity theorem holds when $\Omega_p = \mathbb{R} \cup \pm\infty$ and the small gain theorem holds when $\Omega_s = \mathbb{R} \cup \pm\infty$ [9,26–30]. In this subsection, based on classical Nyquist theorem, the proof of a stability result for a negative feedback interconnection of stable LTI systems (Fig. 4.1) with mixed small gain and passivity properties is provided. When compared with [11], the causality (rational LTI systems are causal if and only if they are proper) of the subsystems is not required and there is no need to demand input and output strict passivity to hold for both subsystems but only passivity and at least one to be strictly passive. The reason why we provide a soft condition for system passivity and causality, is that in the high frequency band ($\omega \to \infty$), we want a strictly proper subsystem to be passive and for a series R_gL_g-circuit, which is not causal (proper) in the transfer function from Δi to ΔE.

4.2 Active power controlled converter

The block diagram of the active power controlled converter embedded in a weak AC-grid is shown in Fig. 4.2. It shows that the stability of the AC-side dynamics of the active power controlled converter is independent of the DC-side dynamics and thus the stability of $G(s)$ is not considered in this subsection. The system of active power controlled converter interacting with weak AC-grid is stable if the negative feedback loop Y_pZ_2 is stable and G_{p1}, G_p2 are stable.

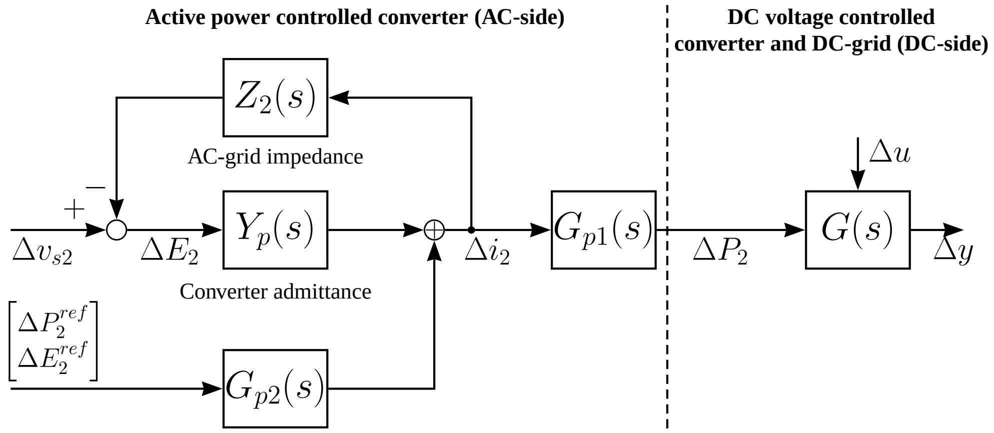

Figure 4.2: Block diagram of the two-terminal VSC-HVDC system connected with weak AC-grids, where $G_{p1}(s)$, $G_{p2}(s)$, $G(s)$ are the transfer function matrices with respect to different input/output signals.

Combining the eq.(2.7, 2.8), (2.11), (2.22, 2.23), (2.30-2.35), results in the transfer functions shown in Fig. 4.2:

$$Z_2(s) = \begin{bmatrix} L_g s + R_g & -\omega_0 L_g \\ \omega_0 L_g & L_g s + R_g \end{bmatrix} \tag{4.1}$$

$$Y_p(s) = \begin{bmatrix} \frac{s}{s+a_p} y_i(s) - \frac{P_{20}}{E_{20}^2}\frac{a_p}{s+a_p} & \frac{Q_{20}}{E_{20}^2}\frac{a_p}{s+a_p}\frac{s}{s+a_{pll}} + \frac{Q_{20}}{E_{20}^2}\frac{a_{pll}}{s+a_{pll}} \\ -\frac{a_c}{s+a_c} K_{ad}(s) & \frac{s}{s+a_{pll}} y_i(s) + \frac{P_{20}}{E_{20}^2}\frac{a_{pll}}{s+a_{pll}} - K_{aq}(s)\frac{a_c}{s+a_c}\frac{s}{s+a_{pll}} \end{bmatrix} \tag{4.2}$$

$$G_{p2} = \begin{bmatrix} \frac{1}{E_{20}}\frac{a_p}{s+a_p} & 0 \\ 0 & g_c K_{ad}(s) \end{bmatrix} \tag{4.3}$$

It is obvious that for positive design bandwidths a_c, a_p, a_{pll}, there are no unstable poles in $G_{p2}(s)$, $Z_2(s)$, $Y_p(s)$. The output active power ΔP_2 is proportional to Δi_2 and ΔE_2 respectively (eq.(2.11)) and thus if the feedback loop system is stable, the output active power is bounded as well. Consequently, the stability of the active power controlled converter (VSC2) is determined by the feedback loop $(1 + L(s))^{-1}$, $L(s) = Y_p(s)Z_2(s)$.

Since the AC-grid model is always strictly positive real if it contains a non-zero resistance R_g, according to Theorem 4 (“mixed” small gain and passivity theorem), the closed loop system $(1 + Y_p(s)Z_2(s))^{-1}$ is stable if $Y_p(s)$ is passive or, for the non-passive frequency band, the product of the gains of $Y_p(s)Z_2(s)$ is strictly less than one.

$Y_p(s)$ is passive if and only if $Y_p(j\omega) + Y_p^H(j\omega) \geq 0$ [9], which implies that:

$$Y_p(j\omega) = \begin{bmatrix} Y_{p11}(j\omega) & Y_{p12}(j\omega) \\ Y_{p21}(j\omega) & Y_{p22}(j\omega) \end{bmatrix}$$

$$Y_p(j\omega) + Y_p^H(j\omega) = \begin{bmatrix} \mathrm{Re}\{Y_{p11}(j\omega)\} & Y_{p12}(j\omega) + Y_{p21}^*(j\omega) \\ Y_{p12}^*(j\omega) + Y_{p21}(j\omega) & \mathrm{Re}\{Y_{p22}(j\omega)\} \end{bmatrix} \geq 0$$

A Hermitian matrix $Y_p(j\omega) + Y_p^H(j\omega)$ is semi-positive definite if and only if the determinants of all leading principal sub-matrices of $Y_p(j\omega) + Y_p^H(j\omega)$ are non-negative, i.e. $\mathrm{Re}\{Y_{p11}(j\omega)\} \geq 0$, $\mathrm{Re}\{Y_{p22}(j\omega)\} \geq 0$ and $\det(Y_p(j\omega) + Y_p^H(j\omega)) \geq 0$ [34].

Assume that $Q_{20} = 0$ (which is a realistic assumption, since the VSCs are most often operated with a unity power factor [6]) and the input active power at VSC2 is negative i.e. $P_{20} < 0$ (which is reasonable since the converter having the lower steady state DC-voltage is set as the active power controller and has negative input power). In addition, by designing $y_i = 0$ (i.e. $a_f \to \infty$, the LPF for the converter voltage of the inner current loop is ignored), the converter admittance matrix $Y_p(s)$ is:

$$Y_p(s) = \begin{bmatrix} -\frac{P_{20}}{E_{20}^2}\frac{a_p}{s+a_p} & 0 \\ -\frac{a_c}{s+a_c}K_{ad}(s) & \frac{P_{20}}{E_{20}^2}\frac{a_{pll}}{s+a_{pll}} - K_{aq}(s)\frac{a_c}{s+a_c}\frac{s}{s+a_{pll}} \end{bmatrix}$$

It shows that when $K_{aq}(s) = 0$, the real part of $Y_{p11}(j\omega)$ and $Y_{p22}(j\omega)$ always have different signs, which implies that the converter dynamics is not passive for all frequencies. Therefore, introducing $K_{aq}(s) = 2\frac{P_{20}}{E_{20}^2}\frac{a_{pll}}{a_c}(1+\frac{a_c}{s})$, which compensates for the dynamics caused by the PLL and will guarantee that the real parts of $Y_{p11}(j\omega)$ and $Y_{p22}(j\omega)$ are positive when the inverter controls the transmitted active power.

In addition, in order to ensure that $\det(Y_p(j\omega) + Y_p^H(j\omega)) \geq 0$, $K_{ad}(s)$ can be designed as $K_{ad}(s) = -k\frac{P_{20}}{E_{20}^2}\frac{a_{vd}}{s+a_{vd}}$ with any positive $k \leq 1$ and $a_{vd} = \frac{a_p a_{pll}}{a_c}$. Consequently, the converter admittance is passive for all frequencies. According to Theorem 2 (passivity theorem), the negative feedback system is stable if $Y_p(s)$ is passive and $Z_2(s)$ is strictly passive, i.e. $\Omega_p = \mathbb{R} \cup \pm\infty$. Thus the active power controlled converter (VSC2) is stable under all connected AC-grids.

Such result is contributed by the new q-axis outer controller, which contains two parts: the low-pass filtered d-axis PCC voltage differences, used to compensate for the AC-voltage drop and a PI-controller on the q-axis PCC voltage, counteracting the PLL dynamics. The comparison between different controllers are shown by the step response from ΔP_2^{ref} to ΔP_2 in Fig. 4.3. It shows that when the connected AC-grid is strong i.e. SCR $= 3$, the step responses are similar between different q-axis outer controller (solid red and solid blue curve). However, when the connected AC-grid becomes weaker i.e. SCR $= 0.95$, the new q-axis outer controller enables the stability of the grid interconnected converter.

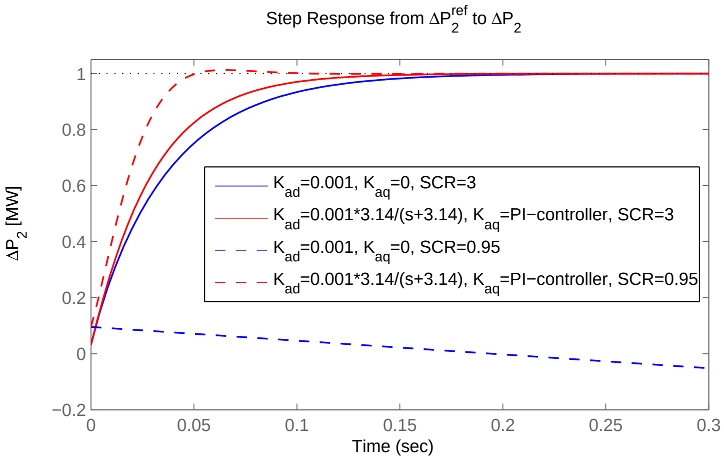

Figure 4.3: Step response from ΔP_2^{ref} to ΔP_2: red curves represent q-axis outer controller designed as $K_{ad}(s) = 0.001\frac{a_{vd}}{s+a_{vd}}$ and $K_{aq}(s) = 2\frac{P_{20}}{E_{20}^2}\frac{a_{pll}}{a_c}(1+\frac{a_c}{s})$, blue curves represent q-axis outer controller designed as $K_{ad}(s) = 0.001$ and $K_{aq}(s) = 0$; solid curves represent the case with SCR $= 3$ and the dashed curves represent the case with SCR $= 0.95$.

4.3 DC voltage controlled converter

As we discussed in section 3.2.2, the active power transmission ΔP_2 is assumed to be zero while the stability of the DC-voltage controlled converter interacting with both AC- and DC-grid is analyzed. In addition, since the external reference signals Δv_{dc1}^{ref} and ΔE_1^{ref} are independent of the system states, the system stability will not be affected by those signals and they can thus be assumed zero.

In this subsection, the DC-cable is modeled as a Π-section, which is shown to be sufficient to analyze the system stability [35]. The active power controlled converter under steady state is modeled as a negative resistance $R_{20} = v_{dc20}^2/P_{20}$ (as $P_{20} < 0$). The transfer function from Δv_{dc1} to Δi_{dc} is:

$$\frac{\Delta\tilde{i}_{dc}}{\Delta\tilde{v}_{dc1}} = G_{dc}(s) = \frac{1}{L_{dc}s + R_{dc} + \frac{R_{20}}{1+R_{20}C_{tot}\cdot s}} \tag{4.4}$$

In order to study the converter-grid interaction, the system is thus depicted as a negative feedback loop of the AC-grid impedance matrix $Z_1(s)$

and the converter admittance matrix $Y(s)$ (including the DC-grid dynamics), which is shown in Fig. 4. Note that the stability of $Y(s)$ is equivalent to the stability of a VSC-HVDC system connected with strong AC-grid, which has been shown to be stable with reasonable designs of local controllers in section 3.2.1. Provided that $Y(s)$ is stable, the stability of the converter-grid interacting system can be further analyzed by Theorem 4.

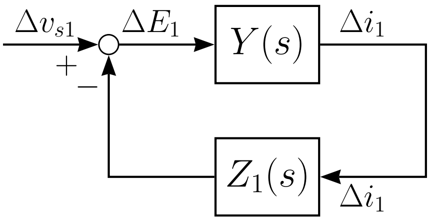

Figure 4.4: Block diagram of the DC voltage controlled converter interacting with both AC- and DC-grid

Combining the eq.(2.7,2.8), (2.10-2.15), (2.19), (2.23), (2.30-2.35), the converter admittance matrix $Y(s)$ and the AC-grid impedance matrix $Z_1(s)$ are:

$$Z_1(s) = \begin{bmatrix} L_g s + R_g & -\omega_0 L_g \\ \omega_0 L_g & L_g s + R_g \end{bmatrix} \tag{4.5}$$

$$Y(s) = \begin{bmatrix} Y_{11}(s) & Y_{12}(s) \\ Y_{21}(s) & Y_{22}(s) \end{bmatrix} \tag{4.6}$$

$$Q_5(s) = C_{tot} v_{dc10} s + (i_{dc0} + v_{dc10} G_{dc})(1 - g_c F_f) + v_{dc10} g_c F_d$$

$$\begin{aligned} Y_{11}(s) = \frac{1}{Q_5(s)} \Bigg\{ & \frac{P_{10}}{E_{10}^2} g_c [F_f (i_{dc0} + v_{dc10} G_{dc}) - v_{dc10} F_d] + \\ & + (y_i - \frac{P_{10}}{E_{10}^2} g_c F_e)(C_{tot} v_{dc10} s + i_{dc0} + v_{dc10} G_{dc}) \Bigg\} \end{aligned}$$

$$Y_{12}(s) = \frac{Q_{10}}{E_{10}^2} \frac{a_{pll}}{s + a_{pll}} + \frac{Q_{10}}{E_{10}^2} \frac{s}{s + a_{pll}} \frac{1}{Q_5(s)} g_c \left\{ v_{dc10} F_d - F_f (i_{dc0} + v_{dc10} G_{dc}) \right\}$$

$$Y_{21}(s) = -g_c(s) K_{ad}(s)$$

$$Y_{22}(s) = (y_i(s) - g_c K_{aq}(s)) \frac{s}{s + a_{pll}} + \frac{P_{10}}{E_{10}^2} \frac{a_{pll}}{s + a_{pll}}$$

When $Q_{10} = 0$, it is obvious that $Y_{12}(s) = 0$. By setting $K_{ad}(s)$ to be a small enough constant, i.e. $K_{ad}(s) \approx 0$ and thus $Y_{21}(s) \approx 0$, the converter admittance matrix $Y(s)$ is then simplified to a diagonal matrix. Therefore, $Y(s)$ is passive if and only if the real parts of both $Y_{11}(j\omega)$ and $Y_{22}(j\omega)$ are non-negative and the gain of $Y(s)$ is the maximum value of $|Y_{11}(j\omega)|$ and $|Y_{22}(j\omega)|$ [34].

Contrary to the active power controller converter, the PLL dynamics provide a term with positive real part in $Y_{22}(j\omega)$ i.e. $\frac{P_{10}}{E_{10}^2}\frac{a_{pll}}{s+a_{pll}}$. Therefore, there is no need to compensate for the effect of the PLL dynamics and thus the design $K_{aq}(s) = 0$ is chosen.

Equation (2.10) and (2.11) show that at steady state with $\Delta P_{load} = 0$, then $\Delta P = 0$ and thus $\Delta i_d = -\frac{P_0}{E_0^2}\Delta E_d$. This implies that with $P_0 > 0$, the impedance $Y_{11}(j\omega)$ has negative real part in the low frequency band and $Y_{11}(0) = -P_0/E_0^2$. Consequently, for the DC-voltage controlled converter, it is impossible to obtain passivity for all frequencies.

According to Theorem 4, since the grid impedance $Z_1(s)$ is strictly passive for all frequencies, the closed loop system is stable if the loop gain is smaller than one when $Y(s)$ is not passive i.e. either $Y_{11}(j\omega)$ or $Y_{22}(j\omega)$ has negative real part. The parameters for the case study made are listed in Tab. 1 and Tab. 1.

Impact of DC-grid length:

In this subsection, the sufficient stability condition with respect to the AC-grid short circuit ratio (SCR $\approx 1/L_g$ [p.u.]) is given under different DC-cable lengths, i.e. $\Delta P_{load1} = 0$, and d= 50 [km], 200 [km]. Assuming $\Delta P_{load1} = 0$ and combining with eq.(4.4), we will obtain:

$$\begin{aligned} & \Delta\tilde{P}_{load1} = v_{dc10}\Delta\tilde{i}_{dc} + i_{dc0}\Delta\tilde{v}_{dc1} = (v_{dc10}G_{dc}(s) + i_{dc0})\Delta\tilde{v}_{dc1} = 0 \\ \Leftrightarrow \quad & v_{dc10}G_{dc} + i_{dc0} = 0 \end{aligned}$$

$$\text{Thus, } Y(s) = \begin{bmatrix} \frac{y_i(s)C_{tot}s - \frac{P_{10}}{E_{10}^2}g_c(s)F_d(s)}{C_{tot}s + g_c(s)F_d(s)} & 0 \\ 0 & y_i(s)\frac{s}{s+a_{pll}} + \frac{P_{10}}{E_{10}^2}\frac{a_{pll}}{s+a_{pll}} \end{bmatrix}$$

The loop gain of $L(s) = Y(s)Z_1(s)$ satisfies:

$$\bar{\sigma}(Z_1(j\omega)) = \begin{cases} \sqrt{R_g^2 + L_g^2(\omega+\omega_0)^2} \approx \frac{1}{SCR}\frac{\omega+\omega_0}{\omega_0}, \text{ for } \omega \geq 0 \\ \sqrt{R_g^2 + L_g^2(\omega-\omega_0)^2}, \text{ for } \omega < 0 \end{cases}$$

$$\bar{\sigma}(Y(j\omega)) = \max(|Y_{11}(j\omega)|, |Y_{22}(j\omega)|)$$

$$\bar{\sigma}(L(j\omega)) \leq \kappa = \sqrt{R_g^2 + L_g^2(\omega+\omega_0)^2} \cdot \max(|Y_{11}(j\omega)|, |Y_{22}(j\omega)|), \text{ for } \omega \geq 0$$

It shows that the upper bound of the loop gain (κ) is linearly proportional to 1/SCR. Therefore, we can first assume that SCR = 1 and the resulting maximum κ in the frequency band where passivity does not hold is the stability sufficient condition of the AC-grid SCR.

The frequency characteristics of $Y_{11}(j\omega)$ and $Y_{22}(j\omega)$ are shown in Fig. 5, where values of all system parameters and steady state entries are set to be constantly equal to the values provided in Tab. 1 and Tab. 1, with the exception of DC cable length.

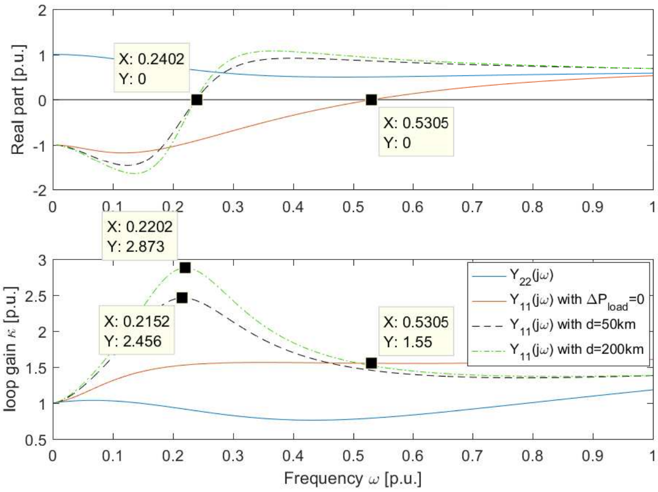

Figure 4.5: Frequency characteristic of $Y_{11}(j\omega)$ and $Y_{22}(j\omega)$ with different DC dynamics

It shows that $Y_{22}(j\omega)$ has positive real part for all frequencies and $Y_{11}(j\omega)$ has positive real part in the high frequency band i.e. $\omega \in [\omega_p, \infty)$ and $\text{Re}\{Y_{11}(j\omega_p)\} = 0$. Therefore, the closed loop system is stable if the gain κ is lower than 1 for $\omega \in [0, \omega_p]$. When $\Delta P_{load1} = 0$, $\omega_p = 0.531$ [p.u.] and the system is stable for SCR > 1.56. For the case with 50, 200 [km] cable length, $\omega_p = 0.24$ [p.u.] and the system is stable for SCR $> 2.46,\ 2.87$ respectively. It implies that the influence of the DC grid dynamics is not ignorable and the longer the DC cable length, the stronger AC-environment is required to guarantee system stability.

Impact of converter controller design:

In this subsection, the sufficient stability condition is compared between cases with different DC-voltage controller i.e. $i^{ref} = P^{ref}/E$ or $i^{ref} = P^{ref}/E_0$ and different bandwidth of the LPF for the AC voltage (a_f).

The comparison result is shown in Fig. 6, where all the non-specified system parameters and steady state entries are set to be constantly equal to the values given in Tab. 1 and Tab. 1.

It shows that by designing $i^{ref} = P^{ref}/E_0$ instead of $i^{ref} = P^{ref}/E$, ω_p decreases from 0.38 [p.u.] to 0.24 [p.u.], in addition, the sufficient condition of a stable closed loop system is improved from SCR $= 2.7$ to SCR $= 2.46$.

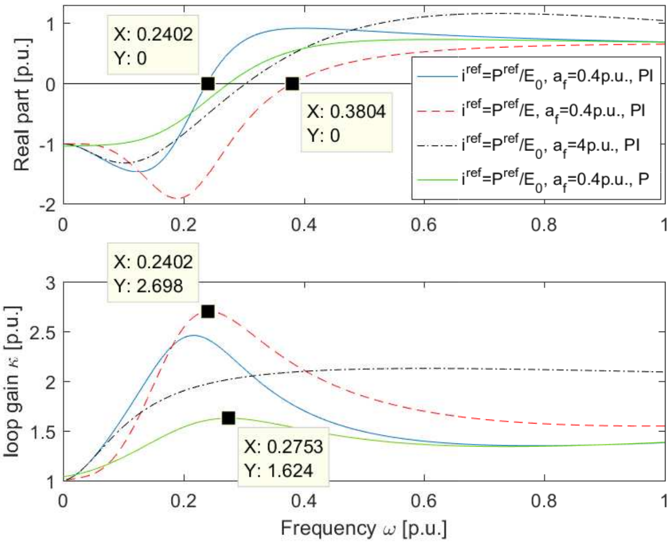

Figure 4.6: Frequency characteristic of $Y_{11}(j\omega)$ and $Y_{22}(j\omega)$ with different converter controllers

Therefore, by designing $i^{ref} = P^{ref}/E_0$, the system robustness with respect to a weak AC-grid is improved.

In addition, by setting $a_f = 4$ [p.u.] (ten times higher), the upper boundary of the loop gain can be decreased but the frequency region of a non-passive converter admittance is also increased. This indicates that if there is a significant resonance at the AC-grid in the low frequency band, it is recommended to introduce an LPF at the measured converter PCC voltage. Otherwise this is not required. The resonance aspect is further discussed in [6].

After designing the outer DC voltage controller as a P-controller with $K_{pd} = C_{tot}a_d$, the upper bound of the loop gain can be decreased from SCR = 2.46 to SCR = 1.63, even though the frequency region of non-passive converter admittance is increased from $\omega_p = 0.24$ [p.u.] to $\omega_p = 0.275$ [p.u.]. Therefore, a P-controller is better than a PI-controller with respect to the system stability robustness.

Note that the “mixed” small gain and passivity theorem might not be the best choice to analyze the stability of series R_gL_g-circuit interconnected DC-voltage controlled converter due to that the uncertainty of the AC-gird is linearly proportional to 1/SCR. However, the “mixed” small gain and passivity theorem can be applied to analyze the stability of grid interconnected converter with other AC-grid topologies, such as AC-grid with parallel resonance (inductor shunt with capacitor) or with series resonance (inductor series with capacitor).

Chapter 5

Analytical investigation of poorly damped conditions

In this section, a method are proposed to obtain approximative analytical expression for eigenvalues of a two-terminal VSC-HVDC system, while the interaction with the AC-side is neglected assuming the presence of strong AC-grids. The symbolic eigenvalues efficiently characterize poorly-damped conditions that may appear on the DC-side of a VSC-HVDC system. Consequently, the interaction between the controller parameters of the terminals and the physical properties of the DC-cable can be better understood and evaluated.

In addition, by applying the symbolic-isolation method [36], the state space model order of a multi-terminal VSC-HVDC system (MTDC) can be reduced to four and thus enables the proposed method to derive the approximate eigenvalues of the MTDC system in symbolic expressions as well.

The VSC-HVDC system model under study is simplified as a fourth order state space model, which is shown to be a sufficient description of a two-terminal connection [37]. The state space model is calculated based on the following assumptions:

- The connected AC-grids are well balanced and strong, which implies that the nominal AC-grid voltage is as most subject to small variations, in this section they are ignored (i.e. $\Delta E_d \approx 0$, $\Delta E_q \approx 0$) and the dynamics of the PLL and the LPF for feed forward PCC voltage are ignored.
- Since the q-axis current (i_q) has no impact on the dynamics at the DC-side (after d- and q-dynamics decoupling), i_q^{ref} is thus assumed to be zero.
- The inner current loop dynamics is ignored, i.e. $\Delta i_{cd} = \Delta i_d^{ref}$.

- The DC-voltage controller is simplified as a P-controller, i.e. $k_{id} = 0$ and $k_{pd} = C \cdot a_d$, where C is the DC-shunt capacitor of the converter.
- The active power controlled VSC is assumed to be operated under steady state. If not, the dynamics caused by the AC-side of the active power controlled VSC is considered as an disturbance input to the DC-side dynamics.

Combining the dynamics of the DC-voltage controlled VSC eq.(2.10) - (2.17), the active power controlled VSC together with DC cable eq.(4.4), the two-terminal VSC-HVDC system can be interpreted as a fourth order state space model, where $C_{tot} = C + c_c \cdot d/2 = C + C_{dc}$ and Δi^f_{load} is the filtered load power normalized by v_{dc10}, i.e. $\Delta \tilde{i}^f_{load} = F_f(s)\Delta \tilde{P}_{load}/v_{dc10}$:

$$\frac{\mathrm{d}}{\mathrm{d}t} x_s = A_s \cdot x_s + B_s \cdot \Delta v^{ref}_{dc1} \tag{5.1}$$

$$y_s = C_s \cdot x_s = \begin{bmatrix} 0 & 1 & 0 & 0 \end{bmatrix} \cdot x_s = \Delta v_{dc1} \tag{5.2}$$

$$x_s^T = \begin{bmatrix} \Delta i^f_{load} & \Delta v_{dc1} & \Delta i_{dc} & \Delta v_{dc2} \end{bmatrix}$$

$$A_s = \begin{bmatrix} -a_{df}\frac{C}{C_{tot}} & a_{df}\frac{C i_{dc10} - a_d C_{dc} C v_{dc10}}{C_{tot} v_{dc10}} & a_{df}\frac{C}{C_{tot}} & 0 \\ \frac{1}{C_{tot}} & -\frac{a_d C v_{dc10} + i_{dc10}}{C_{tot} v_{dc10}} & -\frac{1}{C_{tot}} & 0 \\ 0 & \frac{1}{L_{dc}} & -\frac{R_{dc}}{L_{dc}} & -\frac{1}{L_{dc}} \\ 0 & 0 & \frac{1}{C_{tot}} & -\frac{P_{20}}{C_{tot} v^2_{dc20}} \end{bmatrix}$$

$$B_s^T = \begin{bmatrix} a_{df} a_d \frac{C_{dc} C}{C_{tot}} & a_d \frac{C}{C_{tot}} & 0 & 0 \end{bmatrix}$$

It is easy to show that the state space model is of minimum order, implying that the system poles are the eigenvalues of the state matrix A_s. The suggested method to analytically describe the poles of the system will thus operate on the symbolic state matrix A_s, in an effort to extract the desired approximate analytical expressions.

5.1 Symbolic eigenvalue expressions

The characteristic polynomial of the 4×4 matrix A_s can be regarded as a product of two second order polynomials $p_1(\lambda)$ and $p_2(\lambda)$. We are in fact most interested in $p_1(\lambda)$, which is poorly damped and its roots are strongly dependent of the DC-cable length. $p_2(\lambda)$, whose roots are well damped and may even be real, is to a low extent dependent of the DC-cable length. Consequently, $p_2(\lambda)$ can be approximately calculated by assuming that the DC-cable length is zero.

Letting the DC-cable length to approach zero, the fourth order system will exactly reduce to a second order system. The characteristic polynomial of the new 2×2 state matrix A_{s2} can be assumed to approximate the well damped polynomial $p_2(\lambda)$, i.e. $p_2(\lambda) \approx \hat{p}_2(\lambda)$. Therefore, we can use $\hat{p}_2(\lambda)$ to calculate an approximated poorly damped polynomial $\hat{p}_1(\lambda) \approx p_1(\lambda)$.

To reduce the visual complexity, A_s is re-written as:

$$A_s = \begin{bmatrix} -a & b & a & 0 \\ \frac{1}{C_{tot}} & -e & -\frac{1}{C_{tot}} & 0 \\ 0 & \frac{1}{L_{dc}} & -\frac{R_{dc}}{L_{dc}} & -\frac{1}{L_{dc}} \\ 0 & 0 & \frac{1}{C_{tot}} & f \end{bmatrix}$$

$$\text{where } a = a_{df}\frac{C}{C_{tot}},\ b = a_{df}\frac{Ci_{dc10} - a_d C_{dc} C v_{dc10}}{C_{tot} v_{dc10}},$$

$$e = \frac{a_d C v_{dc10} + i_{dc10}}{C_{tot} v_{dc10}},\ f = -\frac{P_{20}}{C_{tot} v_{dc20}^2} \tag{5.3}$$

5.1.1 Well damped polynomial $p_2(\lambda)$

If the DC-cable length is zero, then $\Delta v_{dc1} = \Delta v_{dc2}$, $\Delta \dot{v}_{dc1} = \Delta \dot{v}_{dc2}$ and the dynamics of the current passing through the DC-cable, Δi_{dc}, is removed. The new second order autonomous state space model is:

$$\begin{bmatrix} \dot{x}_1 \\ \dot{x}_2 \end{bmatrix} = \begin{bmatrix} -\frac{a}{2} & b - \frac{aC_{tot}}{2}(e+f) \\ \frac{1}{2C_{tot}} & -\frac{e-f}{2} \end{bmatrix} \begin{bmatrix} x_1 \\ x_2 \end{bmatrix} = A_{s2} \begin{bmatrix} x_1 \\ x_2 \end{bmatrix} \tag{5.4}$$

The characteristic function of A_{s2} is:

$$\hat{p}_2(\lambda) = \det(\lambda I - A_{s2}) = \lambda^2 + 0.5(a + e - f)\lambda + 0.5(ae - b/C_{tot}) \tag{5.5}$$

5.1.2 Poorly damped polynomial $p_1(\lambda)$

The characteristic polynomial of the fourth order state matrix A_s is given below, where k_1 and k_2 are the first and second order coefficient respectively:

$$\det(\lambda I - A_s) = \lambda^4 + (a + e - f + \frac{R_{dc}}{L_{dc}})\lambda^3 + k_2\lambda^2 + k_1\lambda +$$

$$+ (ae - \frac{b}{C_{tot}})(\frac{1}{L_{dc}C_{tot}} - f\frac{R_{dc}}{L_{dc}}) \tag{5.6}$$

Let $\lambda_{1,2}$ be the roots of polynomial $p_1(\lambda)$ and $\lambda_{3,4}$ be the roots of polynomial $p_2(\lambda)$. They satisfy:

$$\lambda_1 + \lambda_2 + \lambda_3 + \lambda_4 = -(a + e - f + \frac{R_{dc}}{L_{dc}}) \tag{5.7}$$

$$\lambda_1 \cdot \lambda_2 \cdot \lambda_3 \cdot \lambda_4 = (ae - \frac{b}{C_{tot}})(\frac{1}{L_{dc}C_{tot}} - f\frac{R_{dc}}{L_{dc}}) \tag{5.8}$$

Combining eq.(5.7)-(5.8) with the approximated polynomial $\hat{p}_2(\lambda)$ eq.(5.5), results in:

$$\lambda_3 + \lambda_4 \approx -\frac{1}{2}(a + e - f); \quad \lambda_3 \cdot \lambda_4 \approx \frac{1}{2}(ae - \frac{b}{C_{tot}})$$

$$\Rightarrow \lambda_1 + \lambda_2 = -\frac{1}{2}(a + e - f + 2\frac{R_{dc}}{L_{dc}}) \tag{5.9}$$

$$\lambda_1 \cdot \lambda_2 = 2(\frac{1}{L_{dc}C_{tot}} - f\frac{R_{dc}}{L_{dc}}) \tag{5.10}$$

The approximate poorly damped polynomial is:

$$\begin{aligned}\hat{p}_1(\lambda) &\approx (\lambda - \lambda_1)(\lambda - \lambda_2) \\ &\approx \lambda^2 + \frac{1}{2}(a + e - f + 2\frac{R_{dc}}{L_{dc}})\lambda + 2(\frac{1}{L_{dc}C_{tot}} - f\frac{R_{dc}}{L_{dc}})\end{aligned} \tag{5.11}$$

5.1.3 Accuracy of the approximations

In this section, the eigenvalues λ_{num} of the VSC-HVDC system, found be numerical extracting them from A_s, are compared to the symbolic eigenvalues λ_{sym} expressed by eq.(5.5) and eq.(5.11). Different scenarios are investigated where the values of all the system's parameters and steady-state entries are set to be constantly equal to the values of Tab. 5.1, with the exception of certain parameters that are allowed to vary. The motive for doing so is to observe the accuracy of the analytical expressions compared to the numerical eigenvalues, for different values of the selected parameters. Seven scenarios are considered:

1. Variation of a_{df} between $10 - 600$ rad/s.
2. Variation of a_d between $10 - 600$ rad/s.
3. Variation of $a_d = a_{df}$ between $10 - 600$ rad/s.
4. Variation of the cable length between $10 - 600$ km.
5. Variation of the active power transmitted at station 2 from -1000 to 0 MW.
6. Variation of the converter DC-shunt capacitor $C_1 = C_2 = C$ between $4.9 - 146.5$ μF (equivalent capacitor charging time constant τ_s changes between $1 - 30$ ms).
7. Variation of the DC-cable impedance density l_c increases from 0.316 to 1.415 mH/km while the capacitance density c_c decreases from 0.138 to 0.0139 μF/km.

Note that the seventh scenario corresponds to that the DC transmission lines change from DC-cables to overhead lines. It is due to that the DC-cable poles are normally laid very close to each other and therefore have a relatively high capacitance and low inductance per km. On the contrary, overhead transmission line poles are located in a relative distance from each other and as a result they have a relatively high inductance and low capacitance per km [37].

Table 5.1: Parameters of VSC-HVDC system

Cable distance	d	100 km
Cable inductance density	l_c	0.316 mH/km
Cable capacitance density	c_c	0.138 μF/km
Cable resistance density	r_c	0.03 Ω/km
DC shunt capacitor ($\tau_s = 4.1$ ms)	C	20 μF
Rated DC voltage	v_{dc0}	640 kV
Rated transmission power	P_b	1000 MW
Bandwidth of DC-voltage controller	a_d	300 rad/s (0.95 p.u.)
Bandwidth of DC-load power filter	a_{df}	300 rad/s (0.95 p.u.)

The nominal algebraic error is shown in Tab. 2. The first four columns show the nominal algebraic error of the real and imaginary part respectively:

$$\varepsilon_{real} = |(\mathrm{Re}[\lambda_{num}] - \mathrm{Re}[\lambda_{sym}])/\mathrm{Re}[\lambda_{num}]| \cdot 100\% \tag{5.12}$$

$$\varepsilon_{imag} = |(\mathrm{Im}[\lambda_{num}] - \mathrm{Im}[\lambda_{sym}])/\mathrm{Im}[\lambda_{num}]| \cdot 100\% \tag{5.13}$$

The last two columns show the nominal algebraic error of the pole magnitude, which is the same as the difference of the system natural frequency for complex poles:

$$\varepsilon_{mag} = ||\lambda_{num}| - |\lambda_{sym}|/|\lambda_{num}|| \cdot 100\% = |(\omega_{n,num} - \omega_{n,sym})/\omega_{n,num}| \cdot 100\% \tag{5.14}$$

The movement of the eigenvalues of A_s with varied a_{df} (bandwidth of the LPF of the DC load power) is shown in Fig. 5.1. The nominal algebraic error of the well damped pole pair is plotted with $a_{df} \in [40,\ 600]$ rad/s. This is because the eigenvalues of the well damped pole pair become complex when a_{df} is larger than 35 rad/s. The error plots will only illustrate the approximation difference of complex pole pairs.

Similarly, the error plots of the well damped pole pair with varied a_d (bandwidth of the DC-voltage control loop) in Fig. 5.2 are also shown with $a_d \in [40,\ 600]$ rad/s and the well damped pole pair becomes complex when a_d is larger than 35 rad/s. Note that for a poorly damped pole pair, since the imaginary part is much larger than the real part, the magnitude error curves are close to the imaginary part error curves (shown in the fourth figure in Fig. 5.1 - Fig. 5.7.

The comparison results show that the maximum relative error appears in the real part of scn. 4, which can be decreased from 20.63% to 7.42% if the studied maximum cable length decreases from 600 km to 300 km. In addition, the maximum relative errors for both a well and a poorly damped pole pair slightly exceeds 10% in scn. 7. It is due to the fact that the relative errors of approximated eigenvalues dramatically depend on the magnitude of the exact eigenvalues. Therefore, when the magnitude of exact eigenvalues decreases, the relative error will increase.

Except of scn. 4, the maximum errors of the approximated result are bounded by 12% and in average are lower than 6.39%. In general, the method provide compact expressions that closely fit the numerically calculated eigenvalues of the system, with relatively small error. The eigenvalue movements under different scenarios are shown in Fig. 5.1 - Fig. 5.7.

Table 5.2: Numerical difference between eigenvalues of As and the roots of of $\hat{p}_1(\lambda)$, $\hat{p}_2(\lambda)$ [%]

Scenarios	Real		Imaginary		Magnitude	
	Max	Average	Max	Average	Max	Average
Scn. 1	0.86	0.59	1.55	0.76	1.51	0.72
Scn. 2	0.86	0.59	1.55	0.74	1.51	0.72
Scn. 3	2.64	1.00	2.43	0.84	2.26	0.80
Scn. 4	8.05	4.02	4.04	1.25	4.27	1.34
Scn. 5	0.75	0.74	0.63	0.25	0.61	0.24
Scn. 6	3.62	1.88	3.16	1.65	2.51	1.44
Scn. 7	6.95	1.89	10.63	4.76	10.49	4.68

a) The pole pair $\lambda_{1,2}$ that has larger ratio of Im$\{\lambda\}$/Re$\{\lambda\}$

Scenarios	Real		Imaginary		Magnitude	
	Max	Average	Max	Average	Max	Average
Scn. 1	1.16	0.85	3.15	1.80	1.48	0.73
Scn. 2	1.16	0.85	3.15	1.80	1.48	0.73
Scn. 3	5.33	1.58	5.12	2.03	2.21	0.79
Scn. 4	20.63	8.49	2.06	1.21	4.46	1.37
Scn. 5	1.09	1.07	1.53	0.96	0.61	0.24
Scn. 6	5.23	2.67	8.17	4.41	2.45	1.41
Scn. 7	6.51	1.95	12.03	6.39	9.49	4.40

b) The pole pair $\lambda_{3,4}$ that has smaller ratio of Im$\{\lambda\}$/Re$\{\lambda\}$

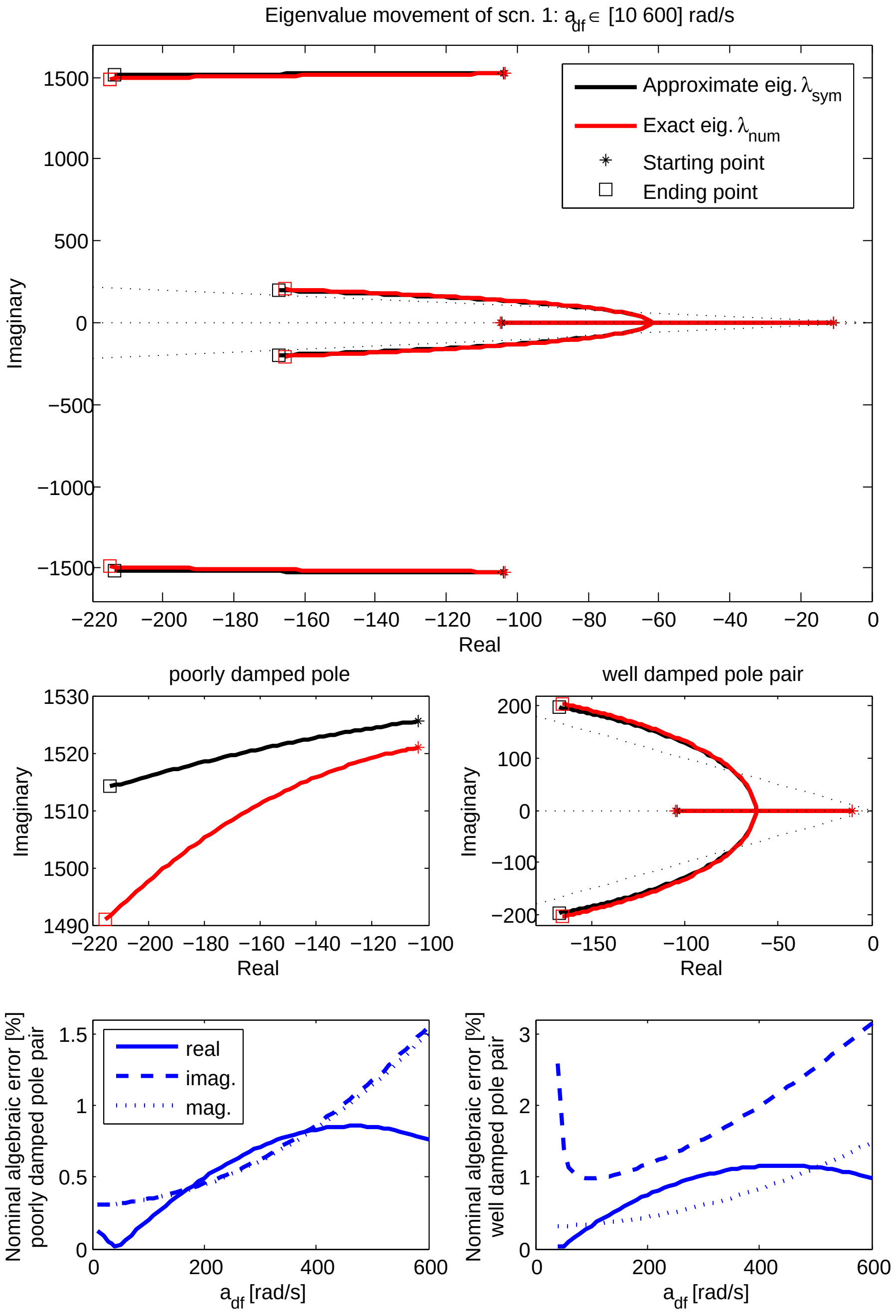

Figure 5.1: Eigenvalue movement and approximation error studies on scn. 1, where a_{df} is varied within [10 600] rad/s.

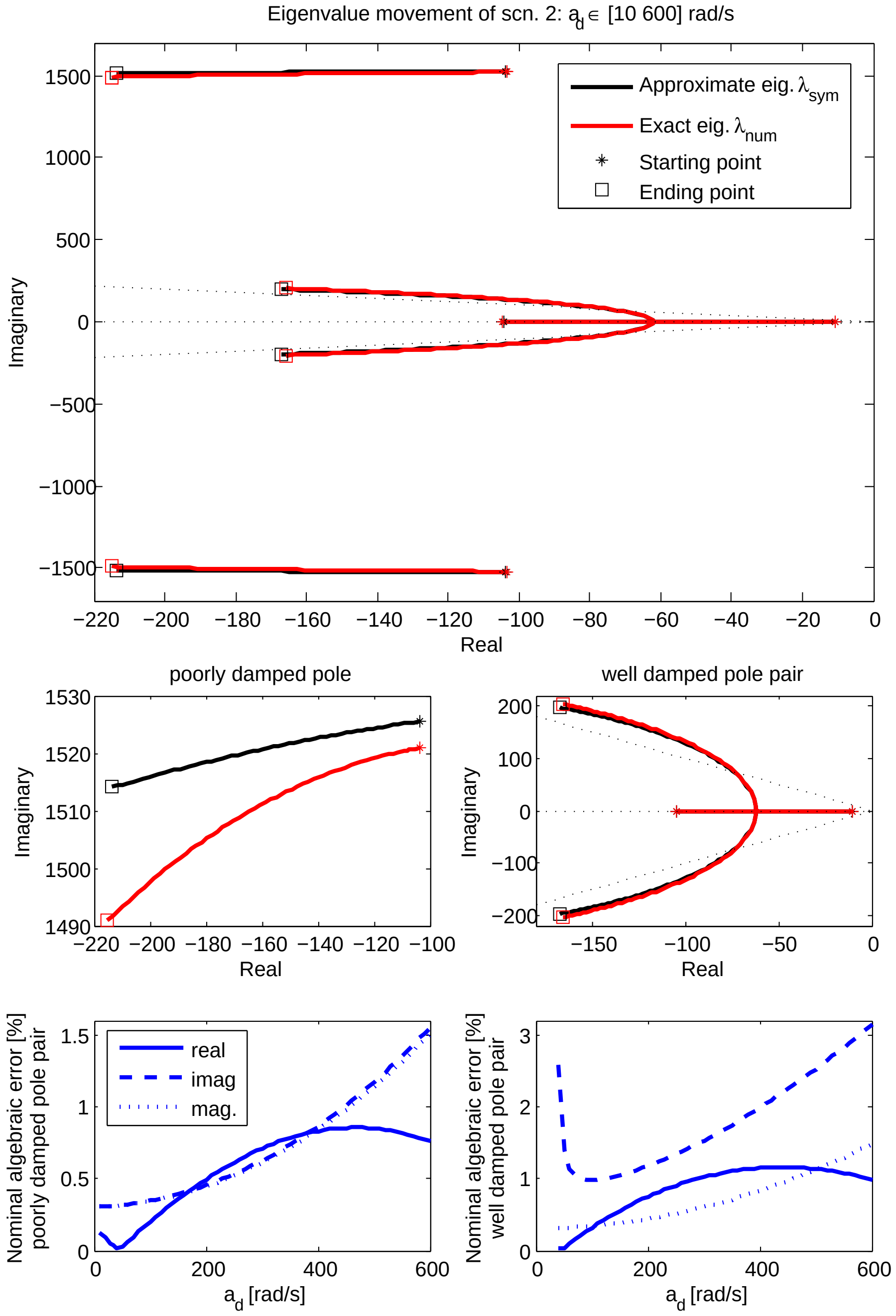

Figure 5.2: Eigenvalue movement and approximation error studies on scn. 2, where a_d is varied within [10 600] rad/s.

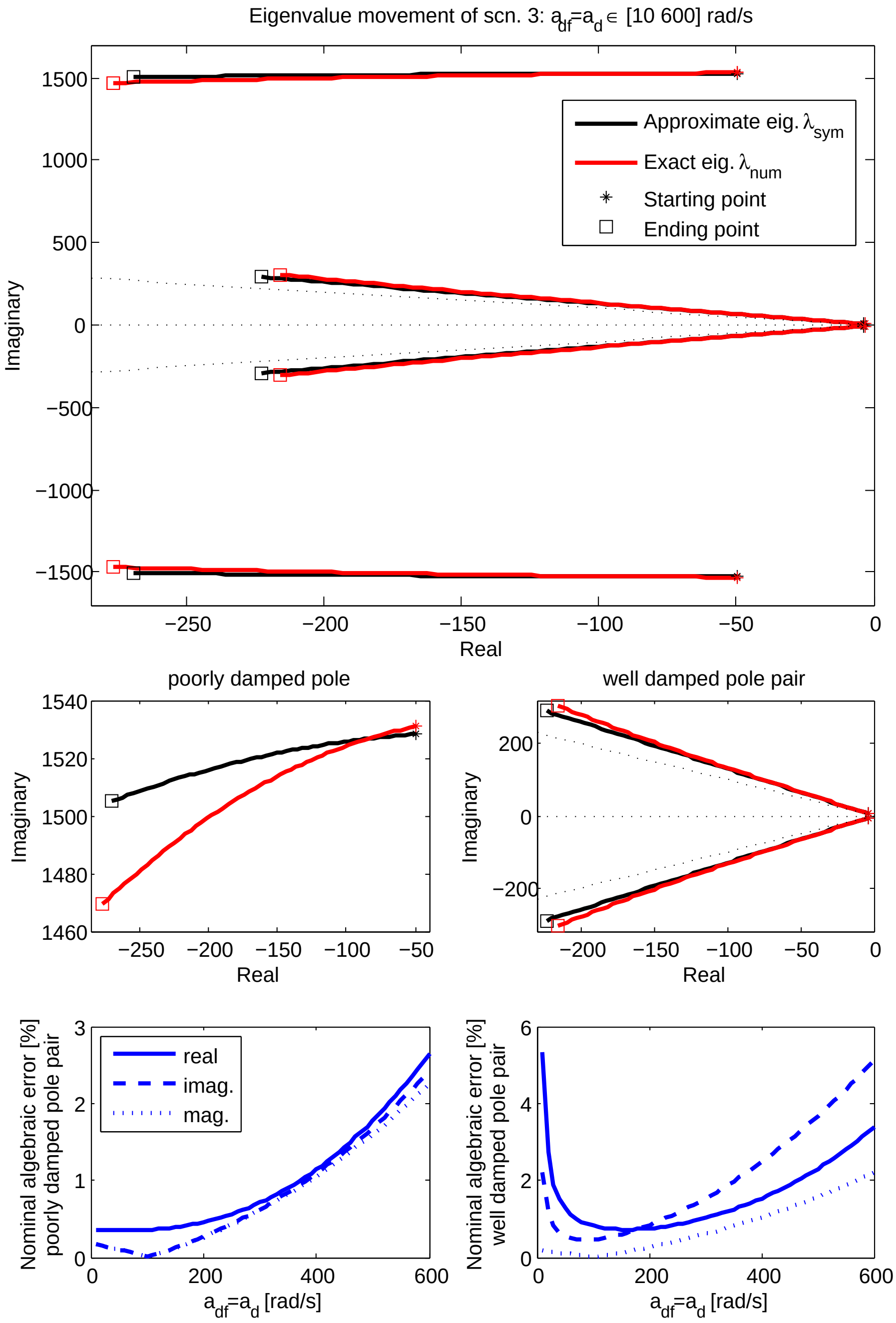

Figure 5.3: Eigenvalue movement and approximation error studies on scn. 3, where $a_{df} = a_d$ and varies within [10 600] rad/s.

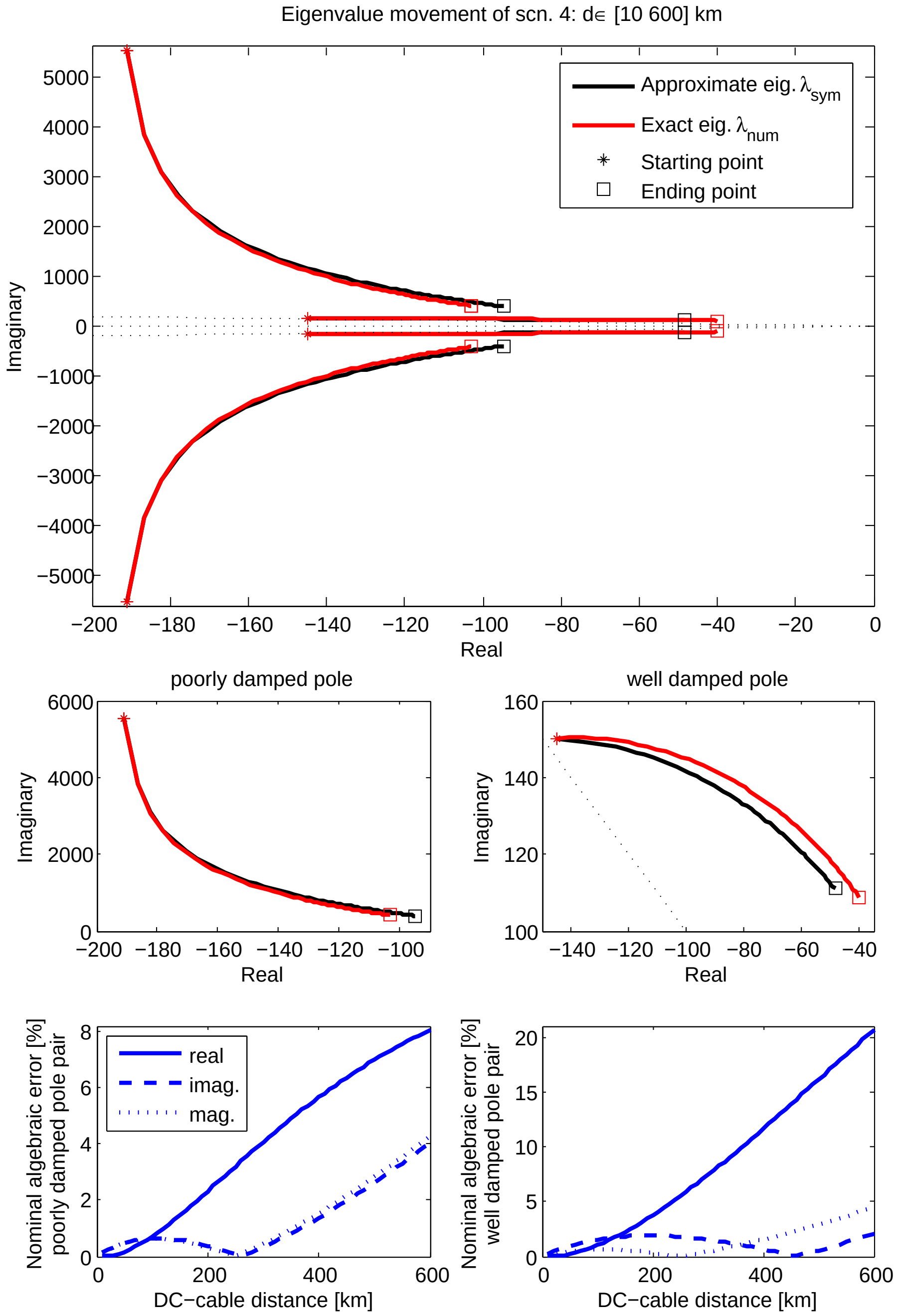

Figure 5.4: Eigenvalue movement and approximation error studies on scn. 4, where the DC-cable distance d is varied within [10 600] km.

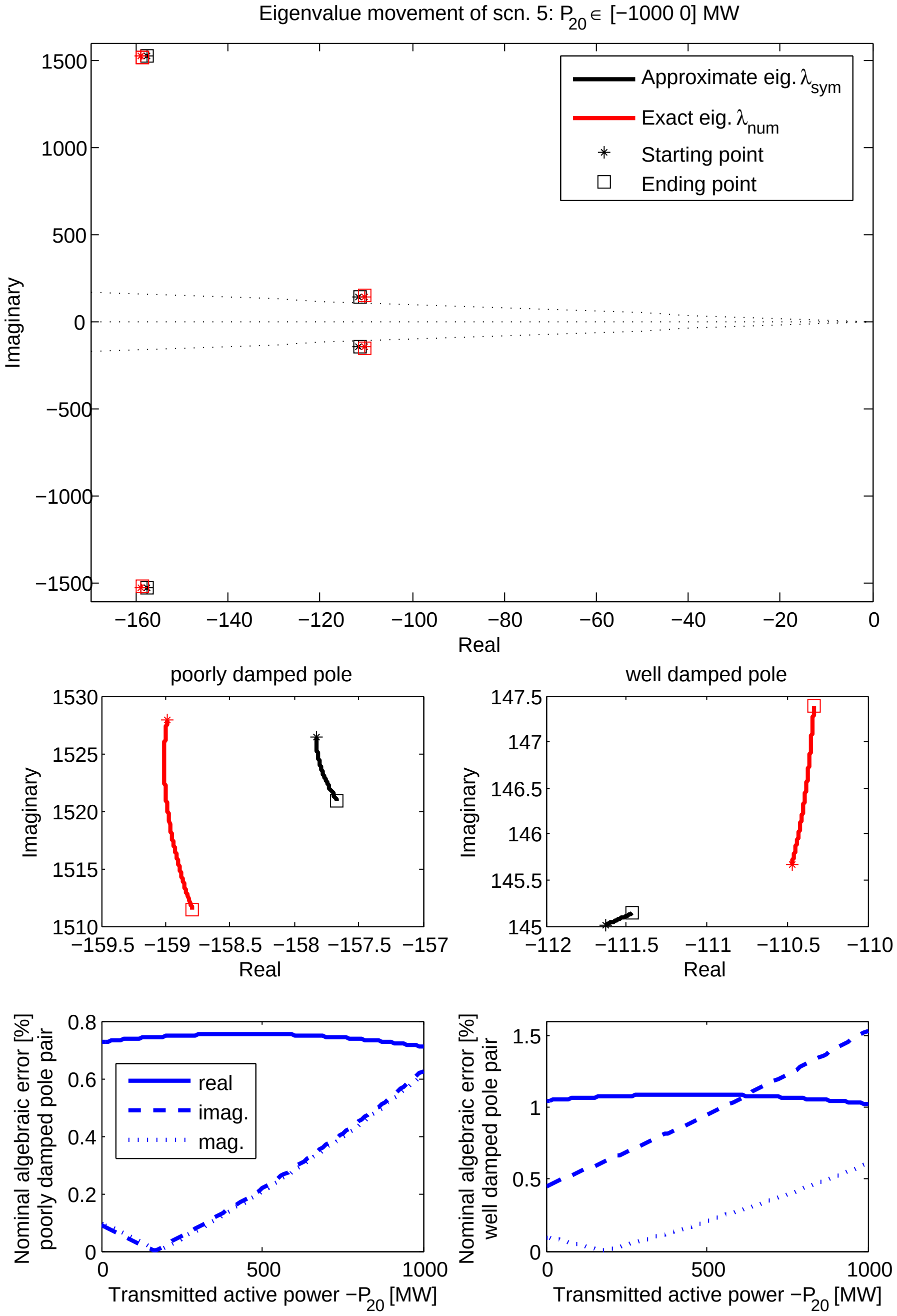

Figure 5.5: Eigenvalue movement and approximation error studies on scn. 5, where the stead state of the transmitted active power at VSC2 P_{20} is varied within [-1000 0] MW (AC→DC is the positive direction).

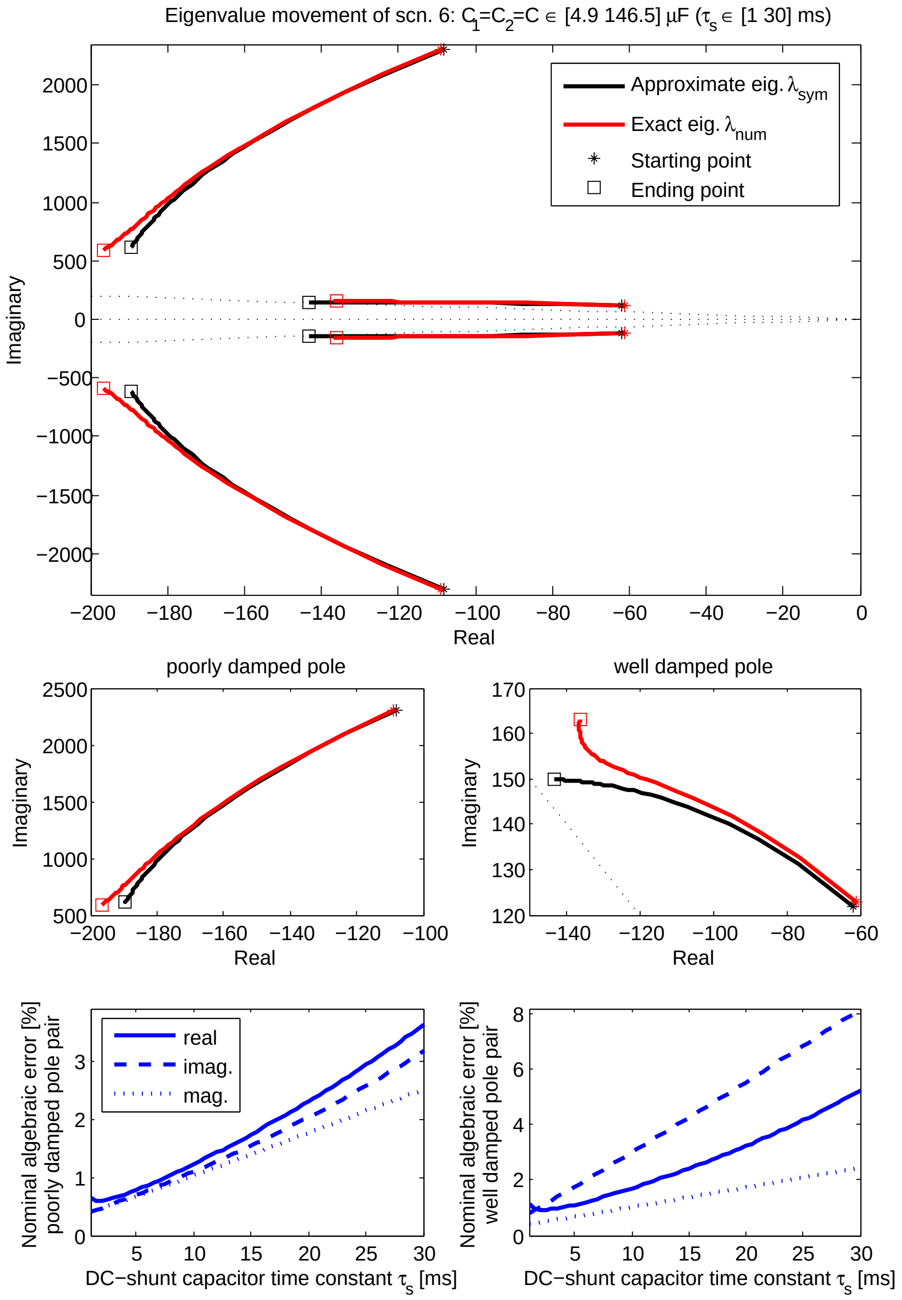

Figure 5.6: Eigenvalue movement and approximation error studies on scn. 6, where the DC-shunt capacitor is varied within [4.9 146.5] μF (equivalent capacitor charging time constant τ_s is varied within [1 30] ms).

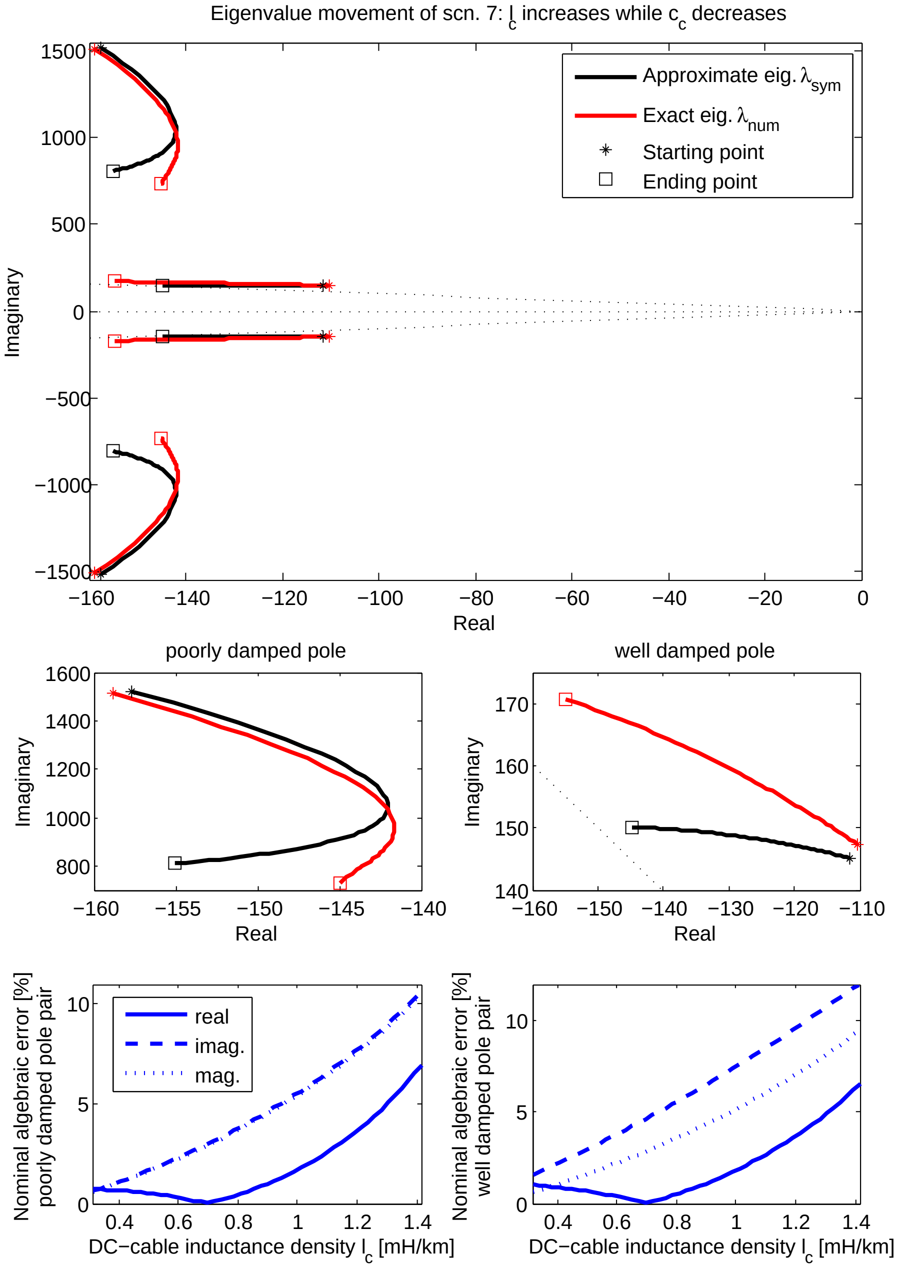

Figure 5.7: Eigenvalue movement and approximation error studies on scn. 7, where the DC-cable inductance density l_c increases from 0.316 to 1.415 mH/km while the capacitance density c_c decrease from 0.138 to 0.0139 μF/km..

5.2 System properties

After achieving approximate symbolic expressions for the system poles, the impact of physical and of control parameters are evaluated in this section.

5.2.1 Trends of the real parts of the eigenvalues

From eq.(5.5) and eq.(5.11), it is known that if the roots are complex then the real part of the system eigenvalues are given as follows, where the approximation is based on the fact that the difference between terminal voltages are so small that they can be neglected compared with the other terms.

$$\begin{aligned}\lambda_1+\lambda_2 &= 2*\mathrm{Re}\{\lambda_{1,2}\} = -0.5(a+d-e+2R_{dc}/L_{dc})\\ &= -\frac{1}{2}[\frac{C}{C_{tot}}(a_d+a_{df})+\frac{i_{dc0}}{C_{tot}}(\frac{1}{v_{dc10}}-\frac{1}{v_{dc20}})]-\frac{R_{dc}}{L_{dc}}\\ &\approx -\frac{C}{2C_{tot}}(a_d+a_{df})-\frac{R_{dc}}{L_{dc}} \qquad (5.15)\\ \lambda_3+\lambda_4 &= 2*\mathrm{Re}\{\lambda_{3,4}\}\\ &= -0.5(a+d-e) = -\frac{1}{2}[\frac{C}{C_{tot}}(a_d+a_{df})-\frac{P_{20}}{C_{tot}}(\frac{1}{v_{dc10}^2}-\frac{1}{v_{dc20}^2})]\\ &\approx -\frac{C}{2C_{tot}}(a_d+a_{df}) \qquad (5.16)\end{aligned}$$

It shows that:

1 By increasing a_d or a_{df}, all system eigenvalues will move to the left, away from the imaginary axis with the corresponding rate of change $C/C_{tot}/4$. This is verified by Fig. 5.1 - Fig. 5.3, i.e. when either a_d or a_{df} increases, both well and poorly damped pole pairs move away from imaginary axis at the same rate.

2 By increasing the cable length or decreasing the magnitude of DC-shunt capacitor C, the ratio of C/C_{tot} will decrease and thus the real part of all the system eigenvalues will decrease i.e. system eigenvalues move towards the imaginary axis as shown in Fig. 5.4 and Fig. 5.6.

3 By increasing the ratio between the cable resistance density and the inductance density, the real part of the poorly-damped system eigenvalues will move (to the left) away from the imaginary axis. However, the real part of the well-damped system eigenvalues pair will not change very much.

4 Since the difference between the terminal steady state voltages is too small, the operating point of transmitted active power P_{20} will not play an important role with respect to the real part of the system eigenvalues. It is shown in Fig. 5.5, where the real part of both well

and poorly damped pole pair will not change dramatically even if P_{20} increases from -1000 to 0 MW.

5.2.2 Trends of the natural frequencies of the eigenvalues

From eq.(5.5) and eq.(5.11), it is known that if the roots are complex, the natural frequencies of the system eigenvalues are the given as follows, where the approximation is based on the fact that the transmission losses (R_{dc}) is much lower than the load (v_{dc20}/i_{dc0}):

$$\lambda_1 \cdot \lambda_2 = |\lambda_{1,2}|^2 = \omega_{n1}^2 = \frac{2}{L_{dc}C_{tot}}(1 - \frac{R_{dc}i_{dc0}}{v_{dc20}}) \approx \frac{2}{L_{dc}C_{tot}} \tag{5.17}$$

$$\lambda_3 \cdot \lambda_4 = |\lambda_{3,4}|^2 = \omega_{n2}^2 = \frac{1}{2}\frac{C}{C_{tot}}a_d a_{df} \tag{5.18}$$

It shows that:

1 The natural frequency of the poorly damped pole pair (ω_{n1}) is dominated by the shunt capacitor and cable inductance. ω_{n1} is decreased by increasing the total shunt capacitor C_{tot} or increasing the cable inductance. It is verified by Fig. 5.4 and Fig. 5.6, where the magnitude of the poorly damped pole pair decreases dramatically if either the DC-shunt capacitor increases (and thus C_{tot} increases) or the DC-cable distance increases (and thus L_{dc} increases).

2 For the well damped pole pair, the natural frequency ω_{n2} mainly depends on the choice of control system bandwidths a_d and a_{df}, which is shown in Fig. 5.1 - Fig. 5.3.

3 Since the coefficients of both approximated pole polynomials (eq.5.5 and eq.5.11) are positive for all physical and control parameters, the VSC-HVDC system under study is always stable. Due to the fact that large relative errors appear at scn. 4 ($d \in [10, 600]$ km), it may have unstable poles when the DC-transmission line is extremely long but also suffer from large DC-voltage drops. Consequently, for reasonable DC transmission distances, the two-terminal VSC-HVDC system under study is always stable with all physical and control parameters.

5.2.3 Trends of the damping ratios and characteristic frequencies

For a second order polynomial $\lambda^2 + k_1 \cdot \lambda + k_2 = 0$ with two complex roots, the characteristic frequency is $\omega_0 = \sqrt{k_2 - k_1^2/4}$ and the damping ratio is $\zeta = k_1/\sqrt{4k_2}$. It implies that by increasing k_1 and decreasing k_2, the system characteristic frequency decreases and the damping ratio increases and thus the system has better dynamic performance.

For the poorly damped pole pair $\lambda_{1,2}$, we have:

$$k_1 \approx \frac{C}{2C_{tot}}(a_d + a_{df}) + \frac{R_{dc}}{L_{dc}}; \quad k_2 \approx \frac{2}{L_{dc}C_{tot}}$$

$$\zeta_1 \approx [\frac{C_c}{2C_{tot}}(a_d + a_{df}) + \frac{R_{dc}}{L_{dc}}]\sqrt{\frac{L_{dc}C_{tot}}{8}} \tag{5.19}$$

$$\omega_0^2 \approx \frac{2}{L_{dc}C_{tot}} - \frac{1}{4}[\frac{C}{2C_{tot}}(a_d + a_{df}) + \frac{R_{dc}}{L_{dc}}]^2 \tag{5.20}$$

1 We can increase the poorly damped system damping ratio by increasing the VSC shunt capacitor C (which is shown in Fig. 5.6) or the system bandwidths a_d, a_{df} (which is shown in Fig. 5.1 - Fig. 5.3). For fixed cable resistance R_{dc}, ζ_1 decreases when L_{dc} increases (which is shown in Fig. 5.7).

2 Since $k_2 \gg k_1^2/4$, the characteristic frequency of poorly damped system decreases when either the DC-cable inductance l_c increases or the converter shunt capacitor C increases.

For the well damped pole pair $\lambda_{3,4}$, we have:

$$k_1 \approx \frac{C}{2C_{tot}}(a_d + a_{df}); \quad k_2 = \frac{1}{2}\frac{C}{C_{tot}}a_d a_{df}$$

$$\zeta_2 \approx \sqrt{\frac{C}{C_{tot}}}\frac{a_d + a_{df}}{\sqrt{8a_d a_{df}}} = \frac{1}{2}\sqrt{\frac{C}{C_{tot}}}\sqrt{1 + \frac{1}{2}(\frac{a_d}{a_{df}} + \frac{a_{df}}{a_d})} \tag{5.21}$$

$$\omega_0^2 \approx \frac{1}{2}\frac{C}{C_{tot}}a_d a_{df} - \frac{1}{16}[\frac{C}{C_{tot}}(a_d + a_{df})]^2 \tag{5.22}$$

1 It is known that $a_d/a_{df} + a_{df}/a_d \geq 2$ where the equality holds when $a_d = a_{df}$. Therefore, $\zeta_2 \geq \sqrt{C/2/C_{tot}}$, and with a larger difference between a_d and a_{df}, the damping ratio of the well damped pole pair will increase. This is well illustrated in Fig. 5.1 - Fig. 5.3. When $a_d = a_{df}$ (Fig. 5.3), the eigenvalue movements with different a_d and a_f is in a line where they have similar damping ratios. However, when only one of a_d and a_{df} changes and the other one is kept constant, the damping ratio of the well damped system will decrease first until $a_d = a_{df} = 300$ rad/s and then decrease as the difference between a_d and a_{df} increases.

2 The characteristic frequency of well damped system increases when a_d and a_{df} increase.

5.3 Symbolic eigenvalues of a MTDC system

In this subsection, the proposed method will be applied to an MTDC system. Assuming that, within an MTDC system, there is only one converter controlling the DC-voltage and the other converters control their transmitted active power between the AC- and DC-grid nodes.

The MTDC system can be described as: one DC-voltage controlled VSC with its shunt capacitor (2nd order system $G_{vsc}(s)$); one $RLCR_0$ DC-grid ($G_{dc}(s)$), where R_0 describes the active power controlled VSC and, at the converters' steady states, $R_{j0} = v_{dcj0}^2/P_{j0}$ of the jth VSC. The block diagram of an autonomous MTDC system is depicted in Fig.3.

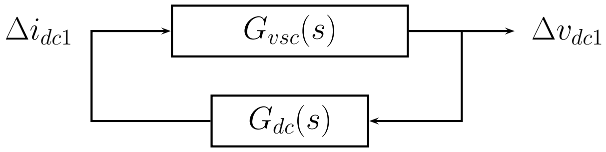

Figure 5.8: Block diagram of the MTDC system with zero input signals

In addition, the parameters of the DC-grid are assumed to be fully known and the parameters at the DC-controlled VSC have free values. The purpose is then to understand the influence of the design bandwidths (a_d, a_{df}), and the chosen shunt capacitor (C_1) on the dynamics of Δv_{dc1} within an MTDC system.

5.3.1 Symbolic-Isolation method

If only the DC-voltage controlled VSC contains symbolic design parameters, we can treat it as a port and reduce the DC-grid by a standard model-reduction approach such as based on the Arnoldi Algorithm [38]. Since this model order reduction algorithm in the state space do not change the input/output port structure and only one port is needed, the isolated symbolic method [36] is simple and straight forward to apply here.

For the linear DC-grid dynamic system, the input signal is the voltage of the DC-voltage controlled VSC (Δv_{dc1}) and the output is the DC-current flow into the DC-grid (Δi_{dc1}). The DC-grid model can be described as follows, where $u_{dcm} = \Delta v_{dc1}$, $y_{dcm} = \Delta i_{dc1}$ and assume $x_{dcm} \in \mathbb{R}^q$. B_{dcm}, C_{dcm} and G_{dcm} are constant matrices of appropriate dimensions.

$$C_{dcm}\frac{\mathrm{d}x_{dcm}}{\mathrm{d}t} + G_{dcm}x_{dcm} = B_{dcm}u_{dcm} \tag{5.23}$$

$$y_{dcm} = F_{dcm}x_{dcm} \tag{5.24}$$

In order to apply the symbolic solution, obtained in the subsection 5.1, the DC-grid system has to be model reduced into a second order system, where the new dynamic states z_{dcm} are calculated based on $x_{dcm} = V_{dcm} z_{dcm}$. The transformation matrix $V_{dcm} \in \mathbb{R}^{q\times 2}$ is then calculated based on the block Arnoldi algorithm [39]:

Arnoldi Algorithm

i Solve $\bar{v}_1$ from: $G_{dcm}\bar{v}_1 = B_{dcm}$.

ii Compute $h_{11} = ||\bar{v}_1||$ and $v_1 = \bar{v}_1/h_{11}$.

iii Solve $\bar{v}_2$ from: $G_{dcm}\bar{v}_2 = C_{dcm}v_1$.

iv Compute $h_{12} = v_1^T\bar{v}_2$, $w_2 = \bar{v}_2 - v_1 h_{12}$, $h_{22} = ||w_2||$ and $v_2 = w_2/h_{22}$.

v Finally $V_{dcm} = [v_1\ v_2]$

The new second order state space model of the DC-grid is then given as follows, where $\bar{C}_{dcm} = V_{dcm}^T C_{dcm} V_{dcm}$, $\bar{G}_{dcm} = V_{dcm}^T G_{dcm} V_{dcm}$, $\bar{B}_{dcm} = V_{dcm}^T B_{dcm}$ and $\bar{F}_{dcm} = F_{dcm} V_{dcm}$:

$$\begin{aligned}\frac{\mathrm{d}z_{dcm}}{\mathrm{d}t} &= -\bar{C}_{dcm}^{-1}\bar{G}_{dcm}z_{dcm} + \bar{C}_{dcm}^{-1}\bar{B}_{dcm}\Delta v_{dc1} \qquad (5.25)\\ &= \begin{bmatrix} a_{z11} & a_{z12} \\ a_{z21} & a_{z22}\end{bmatrix} z_{dcm} + \begin{bmatrix} b_{z1} \\ b_{z2}\end{bmatrix}\Delta v_{dc1}\\ \Delta i_{dc1} &= \bar{F}_{dcm}z_{dcm} = \begin{bmatrix} c_{z1} & c_{z2}\end{bmatrix} z_{dcm} \qquad (5.26)\end{aligned}$$

In order to make the 4th order state matrix of the reduced order MTDC system to have the same structure as A_s, a similarity transformation is required for the above 2nd order system. The similarity matrix is T, where $\bar{z}_{dcm} = T z_{dcm}$:

$$\begin{aligned} T &= \begin{bmatrix} c_{z1} & c_{z2} \\ k\cdot b_{z2} & -k\cdot b_{z1}\end{bmatrix}\\ k &= -\frac{a_{z12}c_{z1}^2 - a_{21}c_{z2}^2 + c_{z1}c_{z2}(a_{z22} - a_{z11})}{(b_{z1}c_{z1} + b_{z2}c_{z2})^2} \qquad (5.27)\end{aligned}$$

5.3.2 Study case: three-terminal VSC-HVDC system

The study system is depicted in Fig. 4, where station 1 controls the DC-voltage and the remaining converters control the transmitted active power. Each of the DC-lines is modeled as a single Π-section with parameters given in Tab. 5.1.

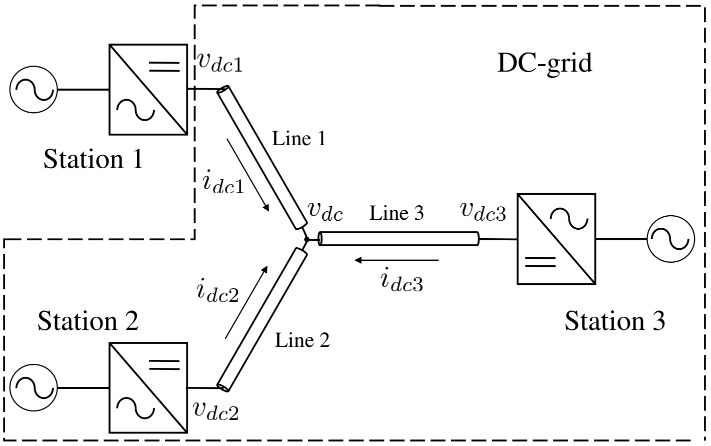

Figure 5.9: Study case 1: 'Y'-shape three-terminal VSC-HVDC system

Table 5.3: DC-grids dynamic parameters

Property	***Value***
Rated DC-voltage of station 1,2,3	640 [kV]
Operating point of active power of station 2	-600 [MW]
Operating point of active power of station 3	-400 [MW]
Shunt capacitor of station 2,3	20 [μF]
Distance of Line 1,2	100 [km]
Distance of Line 3	200 [km]

For fixed set points of v_{dc10}, P_{j0}, $j = 2, 3$ and cable length (which are shown in Tab. 3), the equivalent resistances R_{j0} are countable, i.e. $R_{20} = -667$ [Ω] and $R_{30} = -1003$ [Ω].

In the study case, the state space model matrices are given below, where L_{dcj}, R_{dcj}, C_{dcj} are the inductance, resistance, capacitance (one in each side of the cable) of the j-th line and C_j is the shunt capacitor of the j-th VSC.

$$x_{dcm}^T = \begin{bmatrix} i_{dc1} & v_{dc} & i_{dc2} & v_{dc2} & i_{dc3} & v_{dc3} \end{bmatrix};$$

$$C_{dcm} = \text{diag}\{L_{dc1},\ C_{dc1} + C_{dc2} + C_{dc3},\ L_{dc2},\ C_{dc2} + C_2, L_{dc3},\ C_{dc3} + C_3\}$$

$$G_{dcm} = \begin{bmatrix} R_{dc1} & 1 & 0 & 0 & 0 & 0 \\ -1 & 0 & -1 & 0 & -1 & 0 \\ 0 & 1 & R_{dc2} & -1 & 0 & 0 \\ 0 & 0 & 1 & \frac{1}{R_{20}} & 0 & 0 \\ 0 & 1 & 0 & 0 & R_{dc3} & -1 \\ 0 & 0 & 0 & 0 & 1 & \frac{1}{R_{30}} \end{bmatrix} \quad B_{dcm} = \begin{bmatrix} 1 \\ 0 \\ 0 \\ 0 \\ 0 \\ 0 \end{bmatrix}$$

$$F_{dcm} = \begin{bmatrix} 1 & 0 & 0 & 0 & 0 & 0 \end{bmatrix}$$

The poles of the above DC-grid system are located strictly in the left half plane. Therefore, the system in this study case is stable but not passive. (Note that the DC-grid involves active elements in contrast to the transmission line only.)

The transformation matrix V_{dcm} is applied here to reduce the DC-grid dynamic system into a 2nd order system. After similarity transformation, using the matrix T eq.(35), the numerical second order state space model is:

$$\begin{aligned} \frac{\mathrm{d}}{\mathrm{d}t} z_{dcm} &= \begin{bmatrix} -94.8 & -22.8 \\ 11315 & 28.3 \end{bmatrix} z_{dcm} + \begin{bmatrix} 22.8 \\ 0 \end{bmatrix} \Delta v_{dc1} \\ \Delta i_{dc1} &= \begin{bmatrix} 1 & 0 \end{bmatrix} z_{dcm} \end{aligned} \tag{5.28}$$

The bode plot comparison is given in Fig. 5. It shows that the reduced 2nd order model characterizes the original system well for $\omega < 700$ [rad/s].

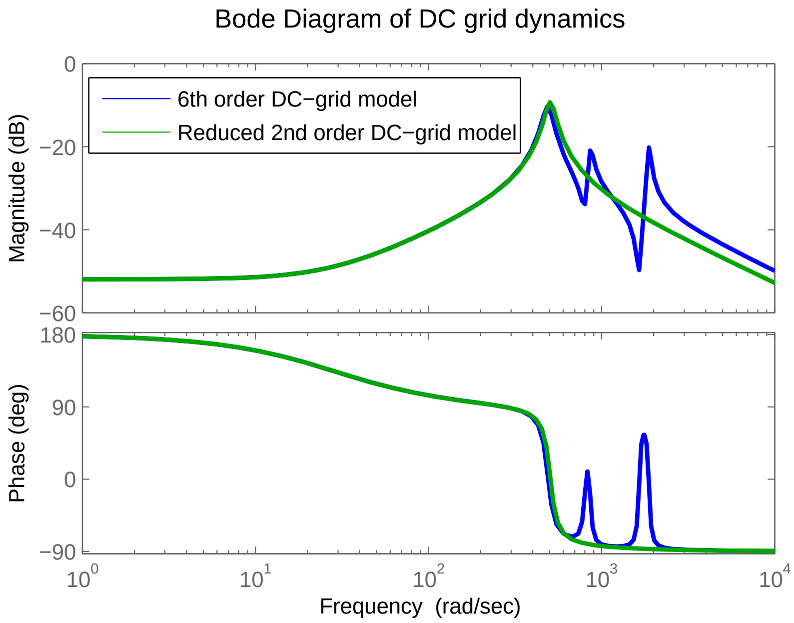

Figure 5.10: Study case 1: Bode plot comparison

5.3.3 Extended method for multi-terminal VSC-HVDC system

After the model order reduction of DC-grid dynamics, the state space model of the MTDC system is:

$$
\begin{aligned}
\frac{\mathrm{d}}{\mathrm{d}t}\hat{x} &= \hat{A}_s \cdot \hat{x} + \hat{B}_s \cdot \Delta v_{dc1}^{ref} && (5.29) \\
\hat{y} &= \hat{C}_s \cdot \hat{x} = \begin{bmatrix} 0 & 1 & 0 & 0 \end{bmatrix} \cdot \hat{x} = \Delta v_{dc1} && (5.30) \\
\hat{x}^T &= \begin{bmatrix} \Delta i_{load}^f & \Delta v_{dc1} & \Delta \hat{i}_{dc} & \Delta \hat{v}_{dc} \end{bmatrix} \\
\hat{A}_s &= \begin{bmatrix} -a_{df}\frac{C_1}{C_{tot}} & a_{df}\frac{C_1 i_{dc10} - a_d C_{dc} C_1 v_{dc10}}{C_{tot} v_{dc10}} & a_{df}\frac{C_1}{C_{tot}} & 0 \\ \frac{1}{C_{tot}} & -\frac{a_d C_1 v_{dc10} + i_{dc10}}{C_{tot} v_{dc10}} & -\frac{1}{C_{tot}} & 0 \\ 0 & 22.8 & -94.8 & -22.8 \\ 0 & 0 & 11315 & 28.32 \end{bmatrix} \\
\hat{B}_s^T &= \begin{bmatrix} a_{df} a_d \frac{C_{dc} C_1}{C_{tot}} & a_d \frac{C_1}{C_{tot}} & 0 & 0 \end{bmatrix}
\end{aligned}
$$

With the proposed method, the characteristic polynomial of $\hat{A}_s$ can be approximated as follows, where $a,\ b,\ e$ are defined in eq.(5.3), c_1 is the shut capacitor at station 1 i.e. $c_1 = C_{tot}$ and in this study case, $c_2 = 88.4 \cdot 10^{-6}$, $R_{dc}/L_{dc} = 94.8$, $f = 28.32$:

$$
\begin{aligned}
&\det(\lambda I - \hat{A}_s) = \hat{p}_1(\lambda)\hat{p}_2(\lambda) \\
&\hat{p}_1(\lambda) = \lambda^2 + \left(\frac{c_2(a+e) - c_1 f}{c_1 + c_2} + \frac{R_{dc}}{L_{dc}}\right)\lambda + \frac{c_1 + c_2}{c_1}\left(\frac{1}{L_{dc} c_2} - f\frac{R_{dc}}{L_{dc}}\right) \\
&\hat{p}_2(\lambda) = \lambda^2 + \frac{c_1(a+e) - c_2 f}{c_1 + c_2}\lambda + \frac{(aec_1 - b)}{c_1 + c_2}
\end{aligned}
$$

Compared with the two-terminal VSC-HVDC system with parameters given in Tab. 5.1, both the shunt capacitor at station 2 and the ratio of L_{dc}/R_{dc} increase, implying that the damping ratio of the poorly damped pole pair will increase. In addition, the poorly damped poles move further away from the imaginary axis and the well damped poles move towards the imaginary axis. The numerical result for the system poles is given in Tab. 4, which as well supports our conclusion. Consequently, the MTDC has better damping performance compared with the two terminal VSC-HVDC system for the poorly damped pole pair but worse damping performance for the well damped pole pair.

Note that the system parameters of the two-terminal VSC-HVDC study case is listed in Tab. 5.1, where the DC-cable length is 100 km. Replacing the active power controlled converter in the two-terminal VSC-HVDC system by another two connected DC-cables and active power controlled converters at the terminal respectively, the MTDC system is constructed as shown

Table 5.4: Eigenvalues of MTDC system

Study case	Eigenvalues			
Two-terminal	-158+1511i	-158-1511i	-110+147i	-110-147i
MTDC	-66+781i	-66-781i	-77-1972i	-77+1972i
	-178+1061i	-178-1061i	-48+112i	-48-112i
4th order MTDC	-254+1037i	-254-1037i	-48+112i	-48-112i

in Fig. 4. The MTDC system has two dynamic states of the DC-voltage controlled converter and six states of the connected DC-grid, where those eight eigenvalues of the MTDC system are listed in Tab. 4. The 4th order MTDC system is calculated by reducing the sixth order DC-grid model to a second order system, which implies that the variations of the well damped pole pair (dominated by the control parameters a_d and a_{df}) after model reduction are ignorable.

Chapter 6

Summary of included papers

This chapter provides a brief summary of the papers that constitute the base for this thesis. Full versions of the papers are included in Part II. The papers have been reformatted to increase readability and to comply with the layout of the rest of the thesis.

Paper 1

> Y. Song and C. Breitholtz, Nyquist stability analysis of a VSC-HVDC system using a distributed parameter DC-cable model, *19th IFAC World Congress*, August 2014, Cape Town, South Africa.

In this paper a two terminal VSC-HVDC system embedded in a strong grid AC-environment is considered, emphasizing modeling, controller design and small-signal stability analysis.

Under assumption of strong grid AC-environment, the dynamics of the PLL and the q-axis of the converter measured input current are ignored. The VSC is modeled as a third order system for the DC-voltage controlled side and as a second order system for the active power controlled side. Traditionally, DC-cables are most often modeled by a single Π-section and the VSC-HVDC system is consequently modeled as a sixth order system, where the system stability can be investigated through eigenvalue calculation. However, when using Π-section cable model for higher frequencies or in case of transmission over long distances and higher cable impedance density such as submarine cables, approximation accuracy aspects ought to be considered. In this paper, a distributed parameter cable model, based on the damped wave equation, is used to overcome this potential limitation.

The VSC-HVDC system with a distributed parameter DC-cable model can be described by two cascaded blocks. The first block is a transfer function that will be different, due to which input and output variables that are considered, but is in all realistic cases stable. The second block is a feedback loop, where the forward path is a rational function and the return path is a dissipative infinite dimensional function, that remains the same in all cases. For a VSC-HVDC system with a single Π-section cable model, the return path of the feedback loop is a first order improper transfer function, which has similar characteristic frequency properties as the distributed parameter cable model in the low frequency band. The stability for both cable models is then analyzed, using the Nyquist criterion in a straight forward manner.

Two examples have been illustrated, showing that in both cases with either the rectifier or the inverter working as DC voltage controller, the VSC-HVDC system with distributed parameter cable model is stable for three different cable distances d=50km, 150km, 450km. Similarly, the VSC-HVDC system with a single Π-section cable model is also stable under the above study cases.

Paper 2

> Y. Song and C. Breitholtz, Nyquist Stability Analysis of an AC-grid connected VSC-HVDC System Using a Distributed Parameter DC-cable Model,*IEEE Trans. on Power Delivery*, vol. 31, no. 2, pp. 898 - 907, April 2016.

In this paper a two terminal VSC-HVDC system embedded in a weak grid AC-environment, represented by an inductance and a resistance in series, is considered. Modeling, controller design and small-signal stability analysis are emphasized.

Under assumption of weak grid AC-environment, the dynamics of the PLL and the AC-grid have to be considered. The d-axis and q-axis currents are coupled due to the AC-grid dynamics. For the active power controlled VSC, the feedback loop stability would not be influenced by the weak AC-grid. Similarly, the stability of the active power controlled VSC could be analyzed without considering the DC-side influence. Consequently, the stability analysis of two terminal VSC-HVDC systems embedded in a weak AC-grid can be separated into two parts: the active power controlled VSC and the VSC-HVDC system while the active power controlled VSC is under steady state.

The stability of the first part is analyzed by the small gain theorem, which shows that for SCR > 2.7, provided the parameter values are taken from Table 1, the active power controlled VSC embedded in a weak AC-environment will always be stable. The second part is analyzed by the

Nyquist criterion. Similar to the strong AC-grid case, the system can be described by two cascaded blocks. The first block is a transfer function that will be different, due to which input and output variables that are considered but is in all realistic cases stable. The second block is a feedback loop, where the forward path is a rational function and the return path is a dissipative infinite dimensional function, that remains the same in all cases. Note that all the blocks, however, will be somewhat more complicated than in the strong AC-grid case.

One typical case has been investigated. Examples with different operating points P_{20} and different SCRs of the connected AC-grids have been studied, showing that the VSC-HVDC system with a single Π-section cable model is sufficient to prove system stability, independently of the DC-cable length and impedance density.

Paper 3

> Y. Song and C. Breitholtz, On passivity based measures of robustness for a VSC-HVDC system connected to weak AC-grids, *to be submitted for possible journal publication*, 2016.

In this paper, a modified "mixed" small gain and passivity theorem is proposed, which is applied to analyze the stability robustness of a two terminal VSC-HVDC system embedded in a weak grid AC-environment. Modeling, controller design and small-signal stability analysis based on a modified "mixed" small gain and passivity theorem are emphasized.

For constant power control of electrical devices, such as in a VSC-HVDC system, the input power $P = E \cdot i$ to the converter is controlled to a constant value, the linearized relationship between input current Δi and the PCC voltage ΔE is given as follows, where ΔP is assumed zero due to the constant power control:

$$E = \frac{P}{i} \;\Rightarrow\; \Delta E = \frac{1}{P_0}\Delta P - \frac{P_0}{i_0^2}\Delta i = -\frac{P_0}{i_0^2}\Delta i$$

Therefore, for positive input power, the converter admittance system (from ΔE to Δi) is not passive in the low frequency band. However, the interconnected AC-grid is always passive and even dissipative for non-zero AC-grid resistance, which enable the passivity theorem as an attractive and powerful tool to analyze the system stability but not fully applicable due to passivity invalidation of the converter admittance. Another important result in the stability theorem of feedback interconnection of two input to output stable LTI systems is the small gain theorem. However, the upper boundary of the AC-grid impedance system is not bounded for series R_gL_g-circuit.

Consequently, the idea of merging those two theorems would be potentially extremely useful. The modified "mixed" small gain and passivity theorem shows that the negative feedback interconnection of two stable LTI systems is input to output stable if in a certain frequency band, both subsystems are passive and at least one of them is strictly passive; in the remaining frequency bands, the loop gain is strictly less than one.

The stability analysis of two terminal VSC-HVDC systems embedded in a weak AC-grid can be separated into two parts: the active power controlled VSC and the VSC-HVDC system while the active power controlled VSC is under steady state. It shows that, by designing the q-axis outer controller to compensate for the PLL dynamics, the active power controlled converter (the first part) can be designed to have passive converter admittance for all frequencies and thus the system is stable under all kinds of connected AC-grids. In addition, at the DC-voltage controlled converter side (the second part), the stability sufficient condition with respect to the AC-grid SCR is studied based on the mixed small gain and passivity theorem. It shows that the system robustness can be increased by designing $i^{ref} = P^{ref}/E_0$ instead of $i^{ref} = P^{ref}/E$.

Paper 4

> Y. Song, C. Breitholtz, G. Stamatiou, and M. Bongiorno, Analytical investigation of poorly damped conditions in VSC-HVDC systems, accepted for presentation at *the 55th IEEE Conference on Decision and Control*, Las Vegas, USA, Dec, 2016.

In this paper, strong AC-grid connected VSC-HVDC systems are studied, which implies that the dynamics of the PLL and the q-axis of the converter measured input current are ignored. In addition, by designing the DC-voltage controller as a P-controller and assuming the active power controlled converter to operate at steady state, the two-terminal VSC-HVDC system can be described as a fourth-order state space model (minimum order). Symbolic eigenvalue expression and the impact of physical and control parameters on the system stability are emphasized.

The characteristic polynomial of the 4×4 state matrix A_s can be seen as a product of two second order polynomials $p_1(\lambda)$ and $p_2(\lambda)$. It shows that $p_1(\lambda)$ has poorly damped roots, which are strongly dependent of the DC-cable length; $p_2(\lambda)$ has well damped roots (and may even be real), which are to a low extent dependent of the DC-cable length. Consequently, by letting the DC-cable length to approach zero, the system will reduce to a second order system where the characteristic polynomial of the new 2×2 state matrix can be assumed to approximate the well damped polynomial $p_2(\lambda)$. Therefore, the approximated poorly damped polynomial is calculated by $p_1(\lambda) \approx \det(\lambda I - A_s)/p_2(\lambda)$.

The approximated symbolic expressions of $p_1(\lambda)$ and $p_2(\lambda)$ are given as follows, which are used to analyze the impact of physical and control parameters on the pole movements.

$$
\begin{aligned}
p_1(\lambda) &\approx \lambda^2 + [\frac{C}{2C_{tot}}(a_d + a_{df}) + \frac{R_{dc}}{L_{dc}}]\lambda + \frac{2}{L_{dc}C_{tot}} \\
p_2(\lambda) &\approx \lambda^2 + \frac{C}{2C_{tot}}(a_d + a_{df})\lambda + \frac{1}{2}\frac{C}{C_{tot}}a_d a_{df}
\end{aligned}
$$

For an MTDC system, it is assumed that there is only one converter controlling the DC-voltage and the remaining converters control their transmitted active power between the AC- and DC-grids. In addition, the DC-voltage controlled VSC keeps symbolic physical and controller parameters, while the remaining converters and the DC-grid parameters are assumed numerically known. The symbolic-isolation method is applied to reduce the system order into four and thus enables the proposed method to derive the approximate eigenvalues of the system in symbolic expressions.

A three-terminal VSC-HVDC system is investigated as an example, which shows that, compared to the two-terminal VSC-HVDC case, the MTDC has better damping performance compared with the two terminal VSC-HVDC system for the poorly damped pole pair but worse damping performance for the well damped pole pair.

References

[1] N. Flourentzou, V. Agelidis, and G. Demetriades, “VSC-based HVDC power transmission systems: An overview,” *IEEE Trans. on Power Electronics*, vol. 24, no. 3, pp. 592–602, March, 2009.

[2] “VSC transmission,” Cigre Working Group, Tech. Rep. B4.37-269, 2005.

[3] P. Bresesti, W. L. Kling, R. L. Hendriks, and R. Vailati, “HVDC connection of offshore wind farms to the transmission system,” *IEEE Trans. Energy Conversion*, vol. 22, no. 1, pp. 37–43, March, 2007.

[4] S. Cole, J. Beerten, and R. Belmans, “Generalized Dynamic VSC MT-DC Model for Power System Stability Studies,” *IEEE Trans. Power System*, vol. 25, no. 3, pp. 1655–1662, August, 2010.

[5] L. Zhang, “Modeling and Control of VSC-HVDC Links Connected to Weak AC System,” Ph.D. dissertation, Royal Institute of Technology, Stockholm, Sweden, 2010.

[6] L. Harnefors, M. Bongiorno, and S. Lundberg, “Input-Admittance Calculation and Shanping for Controlled Voltage-Source Converters,” *IEEE Trans. Ind. Electron.*, vol. 54, no. 6, pp. 3323–3334, Dec., 2007.

[7] B. Wen, D. Dong, D. Boroyevich, R. Burgos, P. Mattavelli, and Z. Shen, “Impedance-based analysis of grid-synchronization stability for three-phase paralleled converters,” *IEEE Trans. on Power Electronics*, vol. 31, no. 1, pp. 26–38, Jan 2016.

[8] J. Sun, “Impedance-based stability criterion for grid-connected inverters,” *IEEE Trans. on Power Electronics*, vol. 26, no. 11, pp. 3075–3078, Nov 2011.

[9] H. K. Khalil, *Nonlinear Systems.* Prentice Hall, 2002.

[10] W. M. Griggs, B. D. O. Anderson, and A. Lanzon, “A ”mixed” small gain and passivity theorem in the frequency domain,” *Systems and Control Letters*, vol. 56, no. 9, pp. 596–602, Sep 2007.

[11] W. M. Griggs, S. S. K. Sajja, B. D. O. Anderson, and R. N. Shorten, “On interconnections of ”mixed” systems using classical stability theory,” *Systems and Control Letters*, vol. 61, no. 5, pp. 676–682, 2012.

[12] B. D. O. Anderson, R. R. Bitmead, C. R. Johnson, R. L. K. I. M. V. M. L. P. Jr., P. Y. Kokotovic, and B. D. Riedle, *Stability of Adaptive Systems: Passivity and Averaging Analysis.* Cambridge, MA: The MIT Press, 2008.

[13] M. Bahrman, E. Larsen, R. Piwko, and H. Patel, “Experience with hvdc - turbine-generator torsional interaction at square butte,” *IEEE Trans. Power App. Syst.*, vol. 99, no. 3, pp. 966–975, May 1980.

[14] N. Prabhu and K. R. Padiyar, “Investigation of subsynchronous resonance with vsc-based hvdc transmission systems,” *IEEE Trans. Power Delivery*, vol. 24, no. 1, pp. 433–440, Jan 2009.

[15] G. Kalcon, G. Adam, O. Anaya-Lara, S. Lo, and K. Uhlen, “Small-signal stability analysis of multi-terminal vsc-based dc transmission systems,” *IEEE Trans. Power System*, vol. 27, no. 4, pp. 1818–1830, Nov 2012.

[16] G. C. Hsieh and J. C. Hung, “Phase locked loop techniques - A survey,” *IEEE Trans. Ind. Electron*, vol. 43, no. 6, pp. 609–615, Dec. 1996.

[17] B. T. Ooi and X. Wang, “Voltage angle lock loop control of the boost type PWM converter for HVDC application,” *IEEE Trans. Power Electronics*, vol. 5, no. 2, pp. 229–235, April, 1990.

[18] “IEEE guide for planning DC links terminating at AC locations having low short circuit capacities,” Tech. Rep. IEEE Std 1204-1997, 1997.

[19] N. Mohan, *Advanced electric drives: analysis, control and modeling using Simulink.* MNPERE, 2001.

[20] A. Jain, K. Joshi, A. Behal, and N. Mohan, “Voltage regulation with STATCOMs: Modeling, control and results,” *IEEE Trans. Power Delivery*, vol. 21, no. 2, pp. 726–735, April, 2006.

[21] B. K. Bose, *Power Electronics and Variable Frequency Drives.* New York, USA: IEEE Press, 1997.

[22] R. Ottersten, "On control of back-to-back converters and sensorless induction machine drives," Ph.D. dissertation, Chalmer University of Technology, Göteborg, Sweden, 2003.

[23] L. F. Drbal, P. G. Boston, and K. L. Westra, *Power Plant Engineering.* Springer, 1996.

[24] M. Durrant, H. Werner, and K. Abbott, "Model of a VSC HVDC terminal attached to a weak ac system," in *IEEE Conference on Control Applications*, Istanbul, 2003.

[25] K. J. Astrom and R. M. Murray, *Feedback System - An Introduction for Scientists and Engineers.* Princeton university press, 2008.

[26] C. A. Desoer and M. Vidyasagar, *Feedback Systems: Input Output Properties.* New York: Academic Press, 1975.

[27] H. J. Marquez, *Nonlinear Control Systems: Analysis and Design.* NJ: John Wiley and Sons, Hoboken, 2003.

[28] M. Green and D. J. N. Limebeer, *Linear Robust Control.* Englewood Cliffs, NJ: Prentice Hall, 1995.

[29] K. Zhou, J. C. Doyle, and K. Glover, *Robust and Optimal Control.* Upper Saddle River, NJ: Prentice Hall, 1996.

[30] A. R. Teel, T. T. Georgiou, L. Praly, and E. Sontag, *Input output stability, in: W.S. Levine (Ed.), The Control Handbook.* Boca Raton, FL: CRC Press, 1996.

[31] S. Skogestad and I. Postlethwaite, *Multivariable Feedback Control: Analysis and Design.* Chichester: John Wiley and Sons, 1996.

[32] J. Bao, P. L. Lee, F. Wang, and W. Zhou, "New robust stability criterion and robust control synthesis," *International Journal of Robust and Nonlinear Control*, vol. 8, no. 1, pp. 49–59, 1998.

[33] M. T. P. Lancaster, *The Theory of Matrices with Applications.* San Diego, London: Academic Press, 1985.

[34] B. Noble and J. Daniel, *Applied Linear Algebra.* Englewood Cliffs, NJ: Prentice Hall, 1998.

[35] Y. Song and C. Breitholtz, "Nyquist Stability Analysis of an AC-Grid Connected VSC-HVDC System Using a Distributed Parameter DC Cable Model," *IEEE Trans. Power Delivery*, vol. 31, no. 2, pp. 898–907, April 2016.

[36] G. Shi, B. Hu, and C. J. R. Shi, “On symbolic model order reduction,” *IEEE Trans. computer-aided design of intergrated circuits and systems*, vol. 25, no. 7, pp. 1257 – 1272, July 2006.

[37] G. Stamatiou, “Converter interactions in VSC-based HVDC systems,” 2015.

[38] I. M. Jaimoukha, “A general minimal residual Krylov subspace method for large-scale model reduction,” *IEEE Trans. Automatic Control*, vol. 42, no. 10, pp. 1422–1427, Oct. 1997.

[39] E. Grimme, “Krylov projection methods for model reduction,” Ph.D. dissertation, Electr. Comput. Eng. Dept., Univ. Illinois, Urbana-Champaign, 1997.